MINERALOGICAL AND PETROPHYSICAL CHANGES IN CARBON DIOXIDE SEQUESTRATION

by

Hyukmin Kweon

A dissertation submitted to the faculty of
The University of Utah
in partial fulfillment of the requirements for the degree of

Doctor of Philosophy

Department of Chemical Engineering

The University of Utah

August 2015

The University of Utah Graduate School

STATEMENT OF DISSERTATION APPROVAL

The dissertation of **Hyukmin Kweon**

has been approved by the following supervisory committee members:

Milind Deo	, Chair	**June 5, 2015** Date Approved
Jan D. Miller	, Member	**June 5, 2015** Date Approved
John McLennan	, Member	**June 5, 2015** Date Approved
Jules Magda	, Member	**June 5, 2015** Date Approved
Joseph Moore	, Member	**June 5, 2015** Date Approved

and by **Milind Deo** , Chair/Dean of

the Department/College/School of **Chemical Engineering**

and by David B. Kieda, Dean of The Graduate School.

ABSTRACT

Carbon dioxide (CO_2) sequestration is a technology being implemented with the potential to mitigate anthropogenic CO_2 emissions. CO_2 injection into underground brine-saturated formations requires a good understanding of the ensuing mineralogical changes. Core floods and batch reactor studies involving three different rock types such as sandstone, limestone, and dolomite were conducted at realistic sequestration conditions in this study. Inductively Coupled Plasma Mass Spectrometer (ICP-MS) was used to obtain effluent brine concentrations as brine and CO_2 were injected/reacted with the different rock types. Analysis of the cores by X-ray Diffraction (XRD), Quantitative Evaluation of Minerals by Scanning Electron Microscopy (QEMSCAN), and Micro-Computed Tomography (Micro-CT) complemented the aqueous-phase compositional measurements. Selected porosity and permeability measurement were also performed using a helium porosimeter. Core flooding revealed the importance of iron chemistry in CO_2 sequestration in sandstone formations. Significant dissolution of iron bearing minerals was observed with slight increase in porosity. This would have implications in the near well bore injection region. Dissolution with wormhole creation was seen in limestone and dolomite experiments. The changes in mineralogy were modeled using TOUGHREACT, a reactive transport geochemical simulator. The experimental changes observed due to changes in flow rates could not easily be reproduced in the model indicating a more

complex underlying processor, even at this scale.

The batch experiments confirmed the types of mineral dissolutions observed in the core studies. Additionally, these experiments helped quantity the effect of surface area (higher surface area leading to more dissolution) and revealed that the heterogeneity of limestone and dolomite permit reactions to occur in the interior. In contrast, sandstone reactions appeared limited to the surface. Surface area measurements showed that the new porosity generated was characterized by a smaller pore size distribution in comparison to the unreacted one.

To my family,

Hyunju and Richard,

with love

TABLE OF CONTENTS

LIST OF TABLES

Tables

LIST OF FIGURES

Figures

ABBREVIATIONS

As	Arsenic
BET	Brunauer-Emmett-Teller
Cd	Cadmium
CO_2	Carbon Dioxide
CCS	Carbon Capture and Storage
CH_4	Methane
CT	Computerized Tomography
DI H_2O	Deionized Water
EDX	Energy Dispersive X-ray Spectroscopy
EGI	Energy and Geosciences Institute
EOR	Enhanced Oil Recovery
GHG	Greenhouse Gas
H_2S	Hydrogen Sulfide
He	Helium
HF	Hydrofluoric Acid
HNO_3	Nitric Acid
ICP-MS	Inductively Coupled Plasma Mass Spectrometry
MRI	Magnetic Resonance Imaging

N_2	Nitrogen
N_2O	Nitrous Oxide
NaCl	Sodium Chloride
Pb	Lead
QEMSCAN	Quantitative Evaluation of Minerals by Scanning Electron Microscopy
SEM	Scanning Electron Microscope
XRD	X-ray Diffraction

ACKNOWLEDGEMENTS

Many thanks to my colleagues at the University of Utah for the countless hours they spent helping me pursue my study. First, I would like to sincerely thank my advisor, Professor Milind Deo, Ph. D., for giving me generous, expert advice through all stages of this research as well as the preparation of all the manuscripts for publication.

Several people have played a decisive role in saving me from leaving chemical engineering. These people are: Kevin Leecaster, Christian Payne, Bradley Dallin, Luanjing Guo, and other laboratory members who have helped throughout. Without your willingness, suggestions, favorable help, and collaboration in experiments and simulations during my study, this Ph.D dissertation would not have been written. I greatly appreciate Dana Overacker and Robert Cox in particular for kindly helping and teaching me the usage of all instruments in my study. Also, I would like to thank Dr. Diego Fernandez, Dr. Chen-Luh Lin, and Yan Wang for your analysis on ICP-MS and Micro-CT.

I would like to express my deep gratitude to my family, especially my parents, younger sister, and my wife’s family, who have always believed and supported me. Special thanks are sent to my wife, Hyunju Lee, and my son, Richard Minjun Kweon, for their love, care, and advice throughout.

And finally, never enough thanks to one who doesn't want to be named.

CHAPTER 1

INTRODUCTION

1.1 Climate Changes and Global Warming

The atmospheric concentrations of greenhouse gases (GHG), such as CO_2, methane (CH_4), and nitrous oxide (N_2O), have increased since the 20th century as a result of human activity. Land use (agriculture and deforestation) is the major factor in the increase in CH_4 and N_2O concentrations, and the use of fossil fuels for power generation, industrial processes, and transportation are the main causes of the increase of anthropogenic CO_2 concentration in the atmosphere. The greenhouse effect works as follows: energy arrives from the sun in the form of visible light and ultraviolet radiation. The Earth then emits some of this energy as infrared radiation. Greenhouse gases in the atmosphere capture some of this heat, then the heat is re-emitted in all directions – including back to the Earth's surface. Some studies indicate that the concentration of CO_2 in the atmosphere increased from 280 ppm to 380 ppm in 1994, and is expected to reach over 550 ppm by 2050.[1, 2] CO_2 is categorized as the major anthropogenic GHG and it is believed it will cause climate changes and global warming if industry does not concern itself with CO_2 emissions.[3] Climate changes and global warming due to industrial CO_2 emissions has been recognized as a serious social concern since 1950.[4, 5] Fossil fuels have many advantages, such as low cost, high energy, abundant supply, etc. Nevertheless,

fossil fuels emit high amounts of CO_2 into the atmosphere, resulting from combustion processes and transportation. Certain industrial processes such as cement making and land use changes also emit CO_2.[6-8] The current situation of the greenhouse effect is formidable; therefore, reducing the emission of CO_2 to reverse climate changes and the global warming trend becomes a prime concern.[9, 10] Under ongoing greenhouse gas emissions, available Earth System Models project that the Earth's surface temperature could exceed historical analogs as early as 2047, affecting most ecosystems on Earth and the livelihoods of over 3 billion people worldwide.[11]

1.2 Several Methods to Mitigate CO_2 Concentration

Recently, many countries have become aware of the significance of carbon emission reduction technologies. There are many technologies used to solve these problems; 1) Energy efficiency and conservation practices that reduce the consumption of carbon-based fuels, 2) Use of carbon-free and reduced-carbon energy sources, 3) Carbon capture and storage (CCS), and 4) Cap and trade and market-based controls, among which CCS has been considered as the most effective way to reduce carbon emission.[12]

Energy efficiency and energy conservation are often referred to as the “cheapest and cleanest sources of energy.” The benefits come in protection against rising energy costs and decreased demand for construction of new energy projects. The latter can translate into a cleaner environment and address climate change concerns. Energy efficiency and energy conservation also contribute to greater national security by reducing demand for other energy sources.

Using carbon-free and reduced-carbon energy sources is one way to reduce carbon emissions. Carbon-free sources such as solar power, wind power, geothermal energy, nuclear power, etc. generate energy without producing and emitting carbon dioxide into the atmosphere. Another solution is switching from high carbon fuel such as coal and oil to low carbon fuels such as natural gas and biomass energy. For instance, the use of cultivated biomass fuels in place of fossil fuels such as coal, oil, and natural gas can result in a reduction in the amount of CO_2 that accumulates in the atmosphere, but only if the carbon released by the combustion of biomass fuels is effectively recaptured.

There are two main ways to capture and sequester CO_2 to mitigate carbon levels in the atmosphere; terrestrial sequestration and geologic sequestration. Terrestrial sequestration involves the collection and storage of CO_2 by plants and the storage of CO_2 in soil. Geological sequestration involves collecting and placing CO_2 into suitable underground formations for storage.

In general, in a cap and trade system, an entity establishes an overall cap for CO_2 emissions within its region. Participants receive permits to emit CO_2 up to that limit. Participants can also purchase “carbon offset credits”. A carbon offset credit is a kind of certificate stipulating that a certain amount of GHG was eliminated or avoided.

1.3 Carbon Capture and Storage (CCS)

CCS is the process of capturing CO_2 from industry and transporting it to a storage site. CCS has been considered for combating the global rise in CO_2 concentration and is a key technology which could be utilized to stabilize CO_2 concentrations to about 450 ppm. There are many options of CCS. First is terrestrial carbon capture and sequestration

in which carbon is stored in forests or soils. Second is geosequestration in which CO_2 is stored in underground rock sites. CO_2 can be directly captured at the point of release, transported to a well site, and injected deep underground into the geologic formation. Chemical conversion can be used to convert CO_2 to another substance to use or sell again. The main purpose is to prevent the release of large quantities of CO_2 into the atmosphere.

Many geological sequestration methods for storing CO_2 have attracted interest and been developed in order to manage CO_2. Sequestration sites in geological formations (see Figure 1), such as in saline aquifers, depleted oil and gas fields, and unmineable coalbeds, are considered the best geological storage sites.[13, 14] CO_2 storage is believed to be particularly feasible in deep saline aquifers because of their large storage capacity and geological ubiquity. In addition, many studies show that most saline aquifers have low

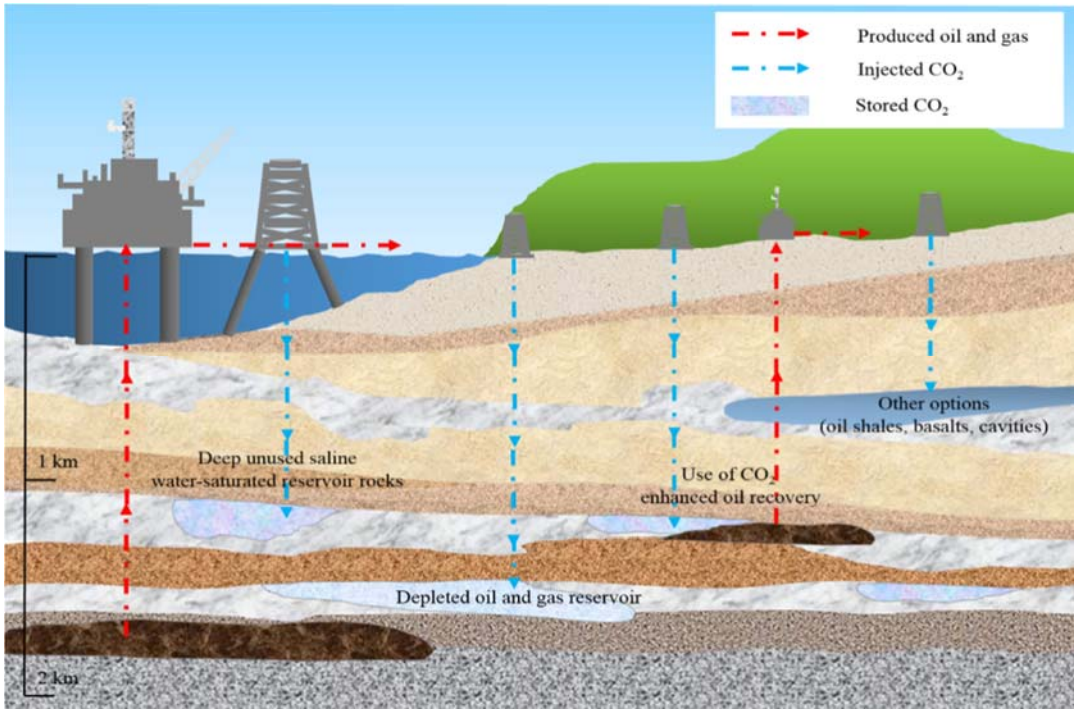

Figure 1. Options for storing CO_2 in deep underground geological formations

permeability.[15-17] The research on the CO_2 flow and storage in low permeability saline aquifers has important significance for mitigating the greenhouse effect and improving CO_2 storage efficiency.[18, 19] Undoubtedly, several such projects have been implemented, and there are no known engineering problems that would prevent large-scale implementation of this form of CO_2 storage.[20, 21] CCS can be implemented at a scale suitable for reducing the emissions of large point sources such as power plants, but high costs and concerns about the long-term containment of CO_2 in the storage reservoir have limited the global deployment of CCS.

1.3.1 CO_2 Geological Storage

The subsurface is the Earth's largest carbon reservoir, where the vast majority of the world's carbon is held in coal, oil, gas, organic-rich shale, and carbonate rocks. Geological storage of CO_2 has been a natural occurrence during the process of chemical weathering of surface terrains and the influence rates of erosion and element fluctuation in the environment for hundreds of millions of years.[22] Geological storage of anthropogenic CO_2 as a greenhouse gas mitigation option was first proposed in the 1970s, but little research was done until the early 1990s. In a little over a decade, geological storage of CO_2 has grown from a concept of limited interest to one that is quite widely regarded as a potentially important mitigation option. One of the major reasons is that geological storage could help to make deep cuts to atmospheric CO_2 emissions. However, for the potential to be realized, geological storage must be the technically safe, environmentally sustainable, and capable of being broadly applied.

For CO_2 geological storage, the CO_2 gas must first be compressed to be supercritical state depending on the rate that temperature (geothermal gradient) and density of CO_2 will increase with depth (over 1 km). Geological storage of CO_2 can be undertaken in a variety of geological settings in sedimentary basins. Within these basins, oil fields, depleted gas fields, deep coal seams, and saline formations are all possible storage formations. Various fluids such as unwanted chemicals, pollutants, and by-products of petroleum production have been injected on a massive scale into the deep subsurface for many years.[23] Natural gas has also been injected and stored in the subsurface on a large scale in many parts of the world for many years. Depleted oil and gas fields and deep saline formations are the most likely candidate sites for geologic storage. Both depleted oil and gas fields and deep saline formations use the several trapping mechanisms as described below.

There are four primary CO_2 trapping mechanisms in saline aquifer formations which are hydrostratigraphic trapping, residual gas trapping, solubility trapping, and mineral trapping. These trapping processes take place over many years at different rates from days to years to thousands of years, but in general, geologically stored CO_2 becomes more securely trapped with time. Demonstrations of various methods of geological storage of CO_2 are already being carried out in a range of projects of varying scale.

Hydrostratigraphic trapping is the most dominant of the trapping mechanisms. Once injected, the supercritical CO_2 can be more buoyant than other liquids that might be present in the pore space. The CO_2 will therefore percolate up through the porous rocks until it reaches the top of the formation where it meets an impermeable layer like a cap-rock. With an artificial CO_2 storage site, the wells that were drilled for injection through

the cap-rock would be sealed with solid physical plugs made of steel and cement, a method which is already used extensively by the natural gas storage industry.

Residual gas trapping happens very quickly as the porous rock acts like a tight, rigid sponge. As the supercritical CO_2 is injected into the formation, it displaces fluid as it moves through the porous rock. As the CO_2 continues to move, fluid again replaces it, but some of the CO_2 will be left behind as disconnected - or residual - droplets in the pore spaces which are immobile, similar to water in a sponge. This is often how the oil has been held for millions of years.

Solubility trapping involves CO_2 dissolusion in other fluids in its gaseous and supercritical state. This phase in the trapping process involves the CO_2 dissolving into the brine already present in the porous rock. The brine containing CO_2 is denser than the surrounding fluids and so will sink to the bottom of the rock formation over time, trapping the CO_2 even more securely.

Mineral trapping is the final phase of trapping resulting from the fact that when CO_2 dissolves in water it forms a weak carbonic acid. Over a long time, however, this weak acid can react with the minerals in the surrounding rock to form solid carbonate minerals. This process can be rapid or very slow depending on the chemistry of the rock and water in a specific storage site, but it effectively binds CO_2 to the rock.

Such geological formations have cap rocks on top of the porous sedimentary rocks that could contain CO_2. Above all, saline formations are very deep, widely dispersed, porous rocks containing unusable water already trapped in the rocks. These conditions meet all the necessary criteria to provide long-term storage. Therefore, deep

saline formations contain most of the global geologic storage capacity for CO_2 and are likely to become the most widely used type of geologic storage site.

1.3.2 CO_2 Injection Process

In a typical implementation of the process, CO_2 in supercritical form is injected into underground porous formations; either oil and gas reservoirs or saline aquifers. The capacity in oil and gas formations is not considered adequate to accommodate the anthropogenic emissions from stationary sources of CO_2 emissions. Thus, for any reasonable amount of CO_2 to be sequestered, saline aquifers must be considered for CO_2 injection and they are potentially important targets for carbon sequestration. Supercritical CO_2 injection occurs routinely in the petroleum industry through enhanced oil recovery (EOR).[24] CO_2 injection processes are a promising EOR technique and could significantly the improve performance of oil reservoirs. CO_2 injection technique is not only an efficient method to increase oil recovery, but also can be considered as a mitigation of the carbon concentration option through permanently storing CO_2 underground.[25, 26]

When the injected CO_2 is supercritical, the storage efficiency will be largely improved.[27] Under a supercritical CO_2 condition, the process of injection and storage of CO_2 in a saline aquifer is actually a two-phase flow problem involving supercritical CO_2 and saline water. The dynamics of CO_2 injection is one of the most important considerations in geological sequestration[28]. Injected CO_2 is trapped in aquifers by two main mechanisms: physical trapping and geochemical trapping. Physical trapping mechanisms confine the injected CO_2 in the subsurface on a short-term basis. Geochemical trapping, associated with chemical reactions between the injected CO_2,

ground water, and the host rock, is of growing interest for long-term storage security. During CO_2 injection, the CO_2 partial pressure and fugacity will increase. It also promotes CO_2 dissolution into reservoir fluids to form aqueous CO_2 and carbonic acid which reacts with different mineral constituents in the rock causing dissolution; in cases where adequate cations are available, precipitation of carbonate phases occurs. This drives down the pH, leading to disequilibrium between the formation water and minerals, resulting in chemical reactions. Other dissolved species also typically increase, due to the dissolution of highly soluble carbonate minerals. The solubility is dependent on the pressure and temperature conditions and ionic strength, with aqueous CO_2 solubility generally increasing with pressure, and decreasing with temperature and salinity.[29] Mineral dissolution/precipitation is more complicated, because it strongly depends on the type of host rock, pH, and brine chemistry. After an initial period of dissolution, carbonate re-precipitation is likely, depending on the mineralogy and mix of cations present in the system.[30] In addition, rates of fluid flow, such as in diffusion- and advection-controlled environments, also govern the rate of water-rock interaction. As the sequestration process continues, carbonic acid continually reacts with the minerals in place.

Mineral reactions result in either dissolution or precipitation. This leads to the creation or reduction of pore space. Pore space dynamics are relevant in defining the ultimate capacity for CO_2, and also affect pressure propagation/equilibration. Thus, the injectivity of CO_2 is also impacted. Superposition of the concentration gradients and heterogeneity in the aquifer makes prediction of these irreversible changes in the system challenging. Reactivity of cap-rock and wellbore integrity is particularly important, since

the reactive changes cause changes in porosities and permeabilities in the rock. These changes lead to changes in injectivity of CO_2. Mechanical properties of the formation are affected with implications on fault activation and induced seismicity. In order to understand the effect of mineral dissolution and precipitation on the properties of a reservoir, the cap-rock and wellbore integrity are some of the key questions.

1.4 Critical Issues for CO_2 Geological Storage

Until recently, the major options under consideration for mitigation of greenhouse gas emissions included switching to non-carbon-based fuels, increasing energy efficiency, and using terrestrial or biotic sequestration of CO_2. However, the idea of storing CO_2 in geologic reservoirs is becoming increasing popular and has been investigated with vigor in recent years. In fact, geological sequestration is likely to be the only option that will allow storing CO_2 in large enough quantities over a short time period to make a difference. The primary attraction of the geological sequestration option is due to the potential for direct and long-term storage of captured CO_2 emissions in close proximity to the CO_2 source. In the geosequestration process, both CO_2 capture and transport involve well known and generally accepted technologies. However, many aspects of CO_2 storage are not very well known; therefore, a new approach is required because the starting point is fundamentally different than those of CO_2 capture and transport.

The existing technology involving seasonal natural gas storage is well established, and for many years the gas has been stored in the subsurface on a large scale in many parts of the world.[31-33] Also, in most countries there are regulations governing

these activities. Beginning in the early 1990s, small-scale and some large-scale CO_2 injection projects have been carried out. Presently, many projects are being conducted. The results from these projects provide important examples of effective management of the injection of CO_2 and other hazardous gases such as H_2S. Although injection of CO_2 has been done at a relatively small scale, it has the potential to be used to significantly decrease emissions from existing stationary sources. The issue of long-term liability is an additional hurdle to widespread CCS deployment.[34]

1.5 Potential Negative Effect of CO_2 Leakage

Potential geologic storage sites will need to be carefully selected and managed so as to minimize any chance of CO_2 leakage.[35, 36] Given the complexity of most geologic reservoirs and the potentially huge volumes of CO_2 that may be injected, the possibility of some leakage over time may never be completely eliminated. Knowledge of the environmental consequences associated with CO_2 leakage from deep subsurface storage is continually evolving. Supercritical CO_2 will undergo exsolution as it migrates from deep to shallower depths (phase changes from liquid to gas). A portion of the CO_2 gas will dissolve into the groundwater, which will cause a low pH aquifer (around pH 1-3). Reactions that may occur due to CO_2 intrusion include mineral dissolution, as well as ion exchange. Changes in pH will likely promote the release of major and minor ions into the aqueous phase, such as iron, calcium, magnesium, aluminum, potassium, sodium, etc. The groundwater may therefore become oversaturated and precipitate to different types. In addition, the release of potentially toxic elements such as lead (Pb), arsenic (As), and cadmium (Cd) that are naturally present in aquifer rocks and sediments may occur also.

As a result, aqueous concentration of potential contaminants my reach levels close to or over maximum contaminant levels.

Lake Nyos is a crater lake in northwest Cameroon. Formed by subterranean volcanic activity, crater lakes commonly are naturally saturated with CO_2. Under normal circumstances, these gases dissipate as the lake water turns over. On Aug. 21, 1986, however, something in the lake went wrong. It is unknown what the trigger was; it may have been a landslide, small volcanic eruption, or even something as small as cold rain falling on the edge of the lake. Whatever the cause, the result was catastrophic. Hundreds of thousands of tons of carbon dioxide burst forth at 60 miles an hour, suffocating people up to 15 miles away. Of the 800 residents of nearby Nyos, only six survived. In all, 1,746 people died and more than 3,500 livestock perished in a matter of minutes. Accidents like this are extremely rare and can only happen if higher concentration leaks exsist. If it is happen, that might come from man-made wells and are likely to diffuse quickly. It also possibly can cause an earthquake. During the 1950s, it was discovered that injection of fluids at high pressures could cause small-to-medium-sized earthquakes. Subsequent scientific studies identified “hydrofracturing”, slippage along pre-existing fractures, and fault activation as the causes for these earthquakes.

1.6 Verification Programs to Detect Potential Reservoir Leakage

Before a CO_2 storage site is chosen, a detailed survey takes place to identify any potential leakage pathways and to assess the storage integrity of the site. Only sites with a high level of integrity are selected for CO_2 storage. In the United States, Europe, and other parts of the world, underground gas storage (natural gas and hydrogen) has an

excellent safety record, with sophisticated monitoring techniques that are easily adaptable to CCS. Additionally, measuring, monitoring, and verification programs will be used to plot the migration of injected CO_2 over time to detect potential reservoir leakage.

CO_2 storage operations are designed to withstand earthquakes. A detailed survey takes place to identify any potential leakage pathways (including seismic faults) before a CO_2 storage site is selected; if these are discovered, then the site will not be selected for CO_2 injection. During injection, scientists and engineers can ensure that the pressure of the CO_2 does not exceed the strength of the rock by limiting injection rates and volumes, thereby avoiding over-pressurization of the reservoir. Additionally, CO_2 storage sites have demonstrated the ability to retain injected carbon dioxide even if a natural earthquake occurs nearby.

To date, no known contamination of groundwater has occurred from the capture and geologic storage of CO_2. Given proper site selection and operation, the risks to usable water supplies would be extremely small. In the unlikely event that CO_2 would migrate upward toward shallower groundwater, seismic monitoring, groundwater analysis, and chemical tracers can detect any CO_2 that migrates upward into groundwater. Surface air and soil sampling can be used to detect potential CO_2 leakage, while underground changes can be monitored by detecting sound, electromagnetic, gravity, or density changes. In addition, the oil and gas industry already has 50 years of experience in monitoring wells and keeping them secure. Based on the understanding of local and regional stresses in the earth's crust, guidelines have been developed to prevent injection-induced microseismicity. Now, regulatory agencies limit injection rates and pressures to avoid unintentional hydrofracturing.

1.7 Implications of Chemical Interactions

Dissolution of CO_2 into formation water during geological storage can acidify the water as some of the CO_2 dissociates, the reactions are summarized below: [37, 38]

$$CO_2 + H_2O \leftrightarrow H_2CO_3 \leftrightarrow H^+ + HCO_3 \leftrightarrow 2H^+ + CO_3^{2-}$$

The implications are reviewed by Gaus (2010)[39] in the context of brine aquifers. During dissolution of CO_2 in water, the weak acid H_2CO_3 forms and dissociates in the water. This results in a decrease in pH, which in turn induces dissolution of minerals of the host rock and possibly results in desorption of ions from mineral surfaces.[40] Interactions involving reactive minerals, for example carbonates, will result in buffering of the pH and a reduction in acidity:

$$FeCO_3 \text{ (Siderite)} + H^+ \leftrightarrow Fe^{2+} + HCO_3^-$$

These CO_2-water-rock interactions have considerable implications in the near-well environment, in terms of increasing porosity and permeability, as a result of dissolution,[41,42] whereas physical mobilisation of non-reactive minerals and precipitation of minerals can substantially reduce porosity and permeability.[43]

During CO_2 injection, dissolution and precipitation could be either beneficial or detrimental, depending on the location in a reservoir system. Although an increase in permeability due to dissolution of minerals in sealing units would be undesirable, an increase in permeability in the near wellbore environment could potentially allow an

increase in CO_2 flow rate, and lead to a lower pressure-gradient.[41] In addition, precipitation of secondary minerals may reduce permeability in a reservoir unit. For instance, precipitation of silicate or carbonate minerals may lead to the sealing of fractures, or reductions in porosity and permeability in overlying cap-rocks.[44, 45]

However, near injection wellbore, strong dissolution of minerals takes place as fresh acidic fluids are continuously injected within a relatively short time frame. These reactions have important effects on various processes: dissolution in the pore structure caused by the acidic solution injection leads to greater connectivity and injectivity,[46] the geomechanical implications of these changes on the stability of the reservoir are of crucial importance in the evaluation of potential injection reservoirs and risk assessment,[47] and the highly dissolved iron observed[48] could be a source of long-term mineral trapping as iron carbonates.

CHAPTER 2

LITERATURE REVIEW

2.1 Induced Seismicity

CO_2 dissolves in water to form carbonic acid which reacts with different host rocks causing dissolution and precipitation. This reactive environment causes changes in porosities and permeabilities in the rocks. These changes are related with injectivity of CO_2. Petrophysical properties of the formation are affected with implications on induced seismicity. Induced seismicity still remains a major issue for public acceptance of geological CO_2 sequestration. Studying induced seismicity due to deep well injection, McGarr (1976) found how the sum of the seismic moments during three years of injection can be related to the amount of fluid injected.[49] Shapiro et al. (2007) introduced a “seismogenic index” which is linked to the expected level of seismic activity at a given fluid injection site, independent of injection parameters.[50]

2.2 CO_2 Leakage Studies

In order for CCS to be a successful mitigation process, well injectivity must remain sufficiently high in order to maintain high injection rates of CO_2 throughout the life of the CCS project. CO_2 injection wells are used to inject CO_2 in supercritical state at high pressure and temperature (over 73.8 bar and 31 °C). In the CO_2 injection process,

one important challenge is the Joule-Thomson cooling effect which is after flowing the injection valves, CO_2 is going to expand and generate low temperature at the wellhead. The outcome is a loss of wellhead integrity and malfunction. CO_2 also attacks the cement and host rocks of the well causing severe corrosion effects. Therefore, the compressive strength decreases and the permeability and porosity of the cement and host rock increase. Locally, reaction between the fluid and cement occurs via the mechanisms proposed by Kutchko et al. (2007, 2008)[51, 52] and modified by Mason et al. (2013).[53] Generally, simplified CO_2 reactions with calcium hydroxide ($Ca(OH)_2$) and Portland cement (C-S-H) commonly used are the following:[54, 55]

$$CO_2 + H_2O \leftrightarrow H_2CO_3$$

$$H_2CO_3 + Ca(OH)_2 \rightarrow CaCO_3 + 2H_2O$$

$$\text{C-S-H} + H_2CO_3 \rightarrow CaCO_3 + \text{amorphous silica}$$

In the initial reaction, carbonic acid in the fluid initially lowers pH at the cement-water interface and later diffusion also lowers pH in the cement's pore water. The cement phases become soluble and release calcium and hydroxide ions that buffer the water's acidity. As the fluid pH rises, calcium carbonate minerals become insoluble, which begin to precipitate. Further exposure to infiltrating acidic fluid leads to dissolution of calcium carbonate minerals. Field-scale studies of wellbore cement exposed to CO_2-rich fluids for years show significant reaction. There are some available studies show evidences for sustained CO_2 leakage.[56-58]

Despite the importance of understanding leaking wells on the host rock side, much remains poorly understood. A few experimental studies about dissolution on the host rocks side have been made.[59-62] As well as, modeling studies have predicted dissolution/precipitation will occur when supercritical CO_2 is injected into a brine-saturated core or saline aquifer.[63-65] These can have adverse effects on well injectivity due to the significant changes of the formation permeability adjacent near the injection well.[66] Oh et al. (2013) conducted core-flooding experiments to investigate the impact of fractures on CO_2 transport, capillary pressure, and storage capacity. Within their experiment, CO_2 saturation reached steady-state conditions throughout the core. However, the CO_2 saturation at the core inlet showed a progressive decrease after 8 injected pore volumes. Many researchers used SEM images to discover dissolution/precipitation occurred at the core inlet or outlet after CO_2 flooding experiment. The observed dissolution/precipitation during experiments highlights the potential for pressure changes. Darcy's Law can describes the condition when pressure change, and the larger the contact area between the fluid and solid, the larger the viscous loss.[67] For most cases, Darcy's Law is valid.

Giorgis et al. (2007) arrived at similar conclusions that the precipitation and the related reduction in formation permeability caused the blockage of the injection well and halted CO_2 injection. Interestingly, Kim et al. (2012) revealed two different precipitation configurations defining the uniform and localized, which were selectively developed dependent on the conditions of both injection rate and the permeability of storage formation. These conditions can be met during pilot-scale CCS projects where the

injection rates can be relatively low and the storage formation tends to have high permeability.

In fact, the buildup of pressure in the annular space between casing strings is surprisingly general. The pressure buildup rate can even be used to estimate the conductivity a leaky well.[68] A well can fail for numerous reasons during all parts of the life of a well. Failure can also occur in various locations in the well construction. For example, failure can occur along the casing-cement-rock interface, within a cemented annulus as tensile fractures, or by debonding of cement from the cement-casing interface.[69] Typically, leaks that remain or develop post completion are difficult to detect and are associated with failure somewhere within the wellbore system or along casing-cement-rock interfaces. This study will look at the case of a single leak path on the host rocks that typically occurs due to mineral dissolution. This leak path can be considered to be a natural closed fracture. This type of fracture has a flow field that is significantly affected by locally varying aperture size[70, 71] which has a direct control on solute residence time[72] and chemical reactions.[73, 74]

2.3 Monitoring Technology for Fluid and Rock Interaction

Previously, CO_2 geological safety issues and verification programs are examined. In order to scale up and more activate short- and long-term CO_2 storage technology, it is necessary to gain a deeper understanding of the chemical reactions under different conditions such as different mineralogy, temperature, pressure, salinity, and heterogeneity. Less information and understanding of the physical, chemical, and geological context make CO_2 storage deep in the subsurface more difficult.[75]

Before studying the long-term fluid and rock interaction affected by different salinity on porosity and permeability changes, the short-term fluid and rock interaction processes occurring in geological reservoirs should be understood. A number of studies have been designed and conducted based on the CO_2-brine-rock interaction in a high-pressure and temperature batch system by Fu et al. (2009)[76], and Carroll et al. (2013).[77] The precipitation of secondary clay minerals from the sample rocks may cause visible porosity and permeability decreases in the sample rocks after exposure to CO_2-saturated brine at reservoir conditions. Significant porosity and permeability changes are also observed in Soong et al. (2014).[78]

Monitoring is also one of the methods to evaluate water–rock reactions using water and gas chemistry and isotope compositions from fluids produced before and after the injection of CO_2.[79] In natural CO_2 fields, analogous to CO_2 storage reservoirs, long-term geochemical processes over thousands of years can be observed and monitoring methodologies can be developed and tested. For instance, the Montmiral CO_2 field in south-eastern France is one of the European sites investigated in the framework of the EU research project ‘‘Natural Analogues for the Storage of CO_2 in the Geological Environment’’ (NASCENT). Effluent samples from the CO_2-rich reservoir are available, which offers an opportunity to test fluid monitoring as a potential tool for CO_2-water-rock interaction assessment.

Knowledge of fluid chemical and isotope compositions are essential to assess CO_2–water–rock interaction in a reservoir. Hence, the detailed assessment of the present chemical and isotope composition is required. The methodology is based on repeated to determine the gas-water ratio and detailed chemical and isotopic analysis of both the

water and gas phases. After determined, these results also can be used for the assessment of long-term CO_2-water-rock interactions and the relevance of geochemical monitoring of reservoir fluids at industrial CO_2 storage sites.

2.4 Mineralogical Changes

The CO_2 injection into geological reservoirs, the short- and long-term fluid and rock interaction processes occurring should be understood. The purposes of fluid and rock interaction study are 1) determining CO_2 trapping mechanism in saline aquifer formation, 2) understanding geochemical reactions, and 3) assessing impact of CO_2 storage on low salinity environments. Many studies have been designed and conducted based on the CO_2-brine-rock interaction in a high-pressure and temperature not only core flooding system by Lebedev et al. (2013)[80, 81], but also simulations by Berg et al. (2013).[82] Generally, the laboratory-scale experiment results show short-term interactions between CO_2, rock, and brine under single flow rate conditions (saturation condition) at reservoir scale.[83]

2.4.1 Determining CO_2 Trapping Mechanism

There are four primary CO_2 trapping mechanisms in saline aquifer formation which are hydrostratigraphic trapping, residual gas trapping, solubility trapping, and mineral trapping. These trapping processes are well described in section 1.3.1.

2.4.2 Understanding Geochemical Reactions

Generally, after CO_2 is injected into deep saline formations, pH of reservoir water can decrease down to 3.0 and chemical components such as calcium, magnesium, aluminum, silicon, carbonate, etc. increase significantly; it is dependent on host rocks. And CO_2 would be sequestrated mainly by secondary carbonate minerals. The sequestration (precipitation) of secondary clay minerals from the sample rocks may cause visible porosity and permeability decreases in the sample rocks after exposure to CO_2-saturated brine at reservoir conditions. Significant porosity and permeability changes are also observed.[84, 85] Minerals in the formation water show different evolution tendency due to specific rock compositions and water chemistry. Xu et al. (2003) described CO_2 was trapped by calcite, dolomite, chlorite, and dawsonite which will occur in the presence of supercritical CO_2. The implication of fluid and rock interactions is summarized simply below:

$$CO_2 + H_2O \leftrightarrow H_2CO_3\ (aq)$$

$$H_2CO_3\ (aq) \leftrightarrow H^+ + HCO_3^-$$

$$\text{Calcite} + H^+ \leftrightarrow Ca^{2+} + HCO_3^-$$

$$\text{Dolomite} + 2H^+ \leftrightarrow Ca^{2+} + Mg^{2+} + 2HCO_3^-$$

$$\text{Chlorite} + 16H^+ \leftrightarrow 5Mg^{2+} + 2Al^{3+} + 3SiO_2(aq) + 12H_2O$$

$$\text{Dawsonite} + 4H^+ \leftrightarrow Na+ + Al^{3+} + CO_2(aq) + 3H_2O$$

Once injected, CO_2 could accelerate fluid and rock interaction, cause pH to decrease, induce the mobilization of metals, inorganic, and organic constituents which

could lead to ground water quality deterioration. When CO_2 mitigates from a deep saline formation, it will change the geochemical conditions in the aquifer and will cause secondary effects. Concentration of major cations in the aquifer note the relatively constant concentration of sodium and potassium, but the general increases in the concentrations of divalent cations with water alkalinities possibly indicate dissolution of carbonate minerals.

2.4.3 Assessing Impact of CO_2 Storage on Low Salinity Environments

Most experiment and simulation studies of the interaction between CO_2, water, and rock in saline aquifer are conducted high salinity environments (5-18 wt. % of NaCl).[86-91] However, in order to improve the necessary potential storage capacity, further investigation of CO_2, water, and rock interaction in fresh water or low salinity formation conditions is needed. Previous work on fluid and rock interactions in fresh water formations has been limited. The limited studies involving fresh ground water compositions have largely focused on the potential risk of CO_2 leakage.[92-94] Additionally, previous experimental work simulating fluid and rock interactions has predominantly been conducted with single or pure mineral samples. Similarly, many studies use elevated temperature conditions to accelerate reactions with a view to predicting the long-term effects of CO_2 injection.[95] However, this may actually lead to thermodynamically inaccessible reactions occurring. Short-term core flooding experiments using variable samples such as sandstone, limestone, and dolomite are conducted in low salinity (1-3 wt. % of NaCl) environments. One purpose of this study is to determine the mineralogical changes in the fluid and rock after being held at near wellbore conditions, and how these

interactions affect mineralogical changes as well as porosity and permeability in different rocks. In order to understand the effects of CO_2 injectivity, the experiments are carried out in the core flooding system with different CO_2 flow rates.

2.5 Petrophysical Changes

Changes in pore structure caused by acidizing have been studied in detail. Acidizing process improves production by creating channels in the reservoir rocks. Numerous experimental studies on the generation of wormholes have been reported by Daccord (1987)[96], Hoefner and Fogler (1988)[97], Wang et al. (1993)[98], Bazin et al. (1996)[99], Fredd et al. (1997)[100], and Buijse and Glasbergen (2005).[101] Traditionally, acidizing is conducted to deliberately increase reservoir permeability to promote transport of fluids. The positive feedback between enhanced brine acidified by CO_2 and dissolution changes in pore structure and volume leads to enhanced connectivity to increase permeability and porosity.[102-104]

While several studies have been conducted on numerical simulation and modeling in underground formations, relatively fewer papers have focused on experimental investigations under flow conditions. In one recent study, Balashov et al. (2013)[105] looked at long-term diffusive transport and trapping mechanisms in deep saline sandstone aquifers upon CO_2 injection. This was a comprehensive modeling study examining detailed mineral changes over about 25,000 years. They observed that, in the diffusion context, tortuosity is an important consideration, even more so than rock permeability. Fundamental changes in rock chemistry under different prevailing reservoir chemistry conditions have also been conducted. For example, Fu et al. (2009) studied alkalifeldspar

dissolution and secondary mineral precipitation in rock-brine systems. There have also been studies of changes in rock chemistry and pore morphology with CO_2 injection in the reservoir and batch experiments are often employed.

Studies on changes in permeability in cement and the associated rock have also been performed. Cao et al. (2013)[106] reported experiments with cement-sandstone composites. The fracture and void aperture in the cement zone increased significantly, whereas the host sandstone remained unaltered. The change in aqueous chemistry due to cement dissolution may have resulted in overall lower reactivity of sandstone. Newell and Carey (2012)[107], on the other hand, observed potential for self-limiting flow along a wellbore defect. Permeabilities in their samples decreased in contrast to the data of Cao et al. (2013). Brunet et al. (2013)[108] observed dissolution and increased permeabilities at the cement-brine interface, but precipitation and loss of permeability in the calcite zone.

The importance of changes in injectivity of CO_2 with regard to permeability and relative permeability were noted by Burton et al. (2009).[109] They found four fold changes in injectivity when different relative permeability curves were used. They did not consider significant changes in pore morphology due to dissolution or precipitation. Fu et al. (2009) studied alkalifeldspar dissolution and secondary mineral precipitation in rock-brine systems that did not contain CO_2. Carroll et al. (2012) identified the importance of reactive iron clay minerals under CO_2 storage conditions in sandstone formations. Experiments were conducted in batch mode with rock fragments. Carroll et al. (2012) did not measure concomitant porosity changes. In this study, the role of iron minerals in sandstone is considered in cores under reactive flow conditions with associated changes in porosity. Core flooding experiments of brine-CO_2 mixtures with carbonates were

reported by Izgec et al. (2005, 2007, and 2008).[110-112] Izgec et al. (2005) reported porosity changes with concomitant permeability variations for CO_2-brine injections in carbonates and observed that porosity and permeabilities increased and then decreased. Alemu et al. (2011) performed CO_2 flooding experiments in the presence of brine and identified changes in petrophysical parameters as the flood progressed. Their goal was to quantify saturation changes of CO_2 and brine under multiphase conditions. They did not look specifically at changes in the core due to reactions. Shi et al. (2009) performed history matching of core flooding CT scan saturation profiles with porosity dependent capillary pressure. The aim of this study was to look at saturation distributions and match those using simulations. Rock reactivity with CO_2 and brine was not considered. Vogt et al. (2014) provided magnetic resonance imaging (MRI) of flow path enhancement in CO_2-brine environment for sandstone and carbonate cores. They observed measurable porosity changes for carbonates, while sandstones did not display any significant changes. Wellman et al. (2003)[113] provide an evaluation of CO_2-brine-reservoir rock interaction with laboratory flow tests and reactive transport modeling. The authors provide porosity and permeability changes from earlier experiments and use a reactive transport model to match the data. They observed the formation of wormhole type structures after a few days of flooding. Experimental data on effluent concentrations and porosity changes along the length of the sample were not provided.

Most of the permeability reduction level with CO_2 injection is usually considered in reservoir conditions. However, petrophysical changes in different rock types such as sandstone, limestone, and dolomite due to CO_2 injection under core flooding conditions are not fully studied. Therefore, the purpose of this study was to examine changes in of

porosity, permeability, and pore morphology in different rocks on CO_2 injection under core flooding conditions, since they have profound impact on CO_2 injectivity and the ultimate fate of CO_2 in the low saline aquifer formation.

2.6 Reactive Transport Modeling

In order to evaluate the short- and long-term impacts of CO_2 during geologic storage, an application of predictive reactive transport numerical models is required.[114, 115] Mineral phase dissolution and precipitation mechanisms are a main key to develop. There are a number of mechanisms proposed that describe mineral dissolution.[116-118] The change in mineral dissolution rate at equilibrium is described to be the result of a change in the primary mechanism of dissolution. Rapidly dissolving of mineral layers is dominated by dissolution at point defects and crystal edges and corners.[119] Most geochemical modeling codes use a general equation based on the transition state theory to incorporate rate-controlling mechanisms into an overall rate law.[120, 121] The rate law shows a dependence on the reactive surface area, catalyzing or inhibiting aqueous species and the Gibbs free energy of reaction.

A reactive transport model relies on a mathematical formulation to describe geochemical processes involving fluid-rock interactions. The general governing equation can be written as, equation (1):

$$\frac{\partial}{\partial \mathrm{t}}(\phi C_i) = \frac{\partial}{\partial \mathrm{x}}\left(\phi D \frac{\partial C_i}{\partial x}\right) - \phi v \frac{\partial C_i}{\partial x} + \phi \sum_k \left(\frac{\partial C_i}{\partial x}\right)_k \qquad (1)$$

where C_i is the concentration of a specific species in the pore fluid, D is the combined diffusion and dispersion coefficient term, v is the linear fluid flow rate, and ϕ is the porosity. The first two terms on the right-hand side describe the transport process (diffusion, dispersion, and advection) while the last term describes the effect of geochemical reactions.

Due to complex boundary conditions and complicated coupling between the transport and reaction terms, it is impossible to provide analytical solutions to equation (1) for even the simplest geochemical systems. Therefore, numerical solutions have to be used. Fortunately, due to the exponential increase in computational power, realistic reactive transport models are beginning to provide new insights to CO_2 injection and storage at both injection and geological time scales. The simulations in this study were carried out using the non-isothermal reactive geochemical transport code TOUGHREACT. The simulator can model geochemical reactions including aqueous complication, mineral dissolution and precipitation, gas dissolution and exsolution, and ion exchange. Special modeling considerations include CO_2 solubility dependence on pressure, temperature, salinity, changes in porosity, and permeability due to mineral dissolution and precipitation. Some studies applied reactive transport modeling to investigate CO_2 injections in sandstone reservoirs.[122, 123]

2.7 Studies of Mineral Dissolution/Precipitation Reaction Rate

CO_2 dissolution into the aqueous phase results in the forming of carbonic acid and a corresponding decrease in the pH where CO_2 is stored. The dissolution of minerals mechanism is pH dependent and is promoted when the fluid is undersaturated. However,

these mechanisms are very dependent on the reservoir conditions such as salinity, mineralogy of rock, and physical properties. Some information on the relevant processes is available from experiments (e.g., Liu et al., 2003; Ueda et al., 2005; Kaieda et al., 2009; Wakahama et al., 2009; Aste et al., 2012),[124-128] numerical simulations (Ukwattage et al., 2014),[129] and studies on natural CO_2-bearing geothermal systems.[130, 131] Liu et al. (2003) conducted lab experiments at different temperatures from 100 °C to 350 °C in the presence or absence of excess CO_2. The results suggested that the addition of excess CO_2 facilitates the dissolution of granite and sandstone and the deposition of secondary minerals, particularly above 250 °C. A similar conclusion was also drawn by Ueda et al. (2005).

Peng et al. (2012) and Qi et al. (2009)[132] conducted experiments on alkali feldspars/Amelia albite-CO_2-brine interactions to assess the alkali–feldspar dissolution in initially acidic fluid. Their analysis of reaction products showed dissolution features on feldspars and precipitation of secondary minerals. Munz et al. (2012)[133] combined an approach of flooding and batch experiments to investigate the mechanisms and rates of plagioclase carbonation reactions. Re et al. (2014)[134] conducted hydrothermal experiments to evaluate the geochemical reactions of fractured granite with thermal water-supercritical CO_2. Yuko et al. (2012) performed granite alteration with CO_2-saturated fluid over 100 °C, which showed the dissolution of granite and the deposition of a secondary sodium, calcium-alumino silicate. Their results revealed the precipitation of illite and smectite, whereas calcite formed during cooling and degassing in the granite experiment with CO_2.

Field experiments were also conducted in Japan, in which water with dissolved CO_2 was injected at high-temperatures to study CO_2 sequestration in solid minerals. During the experiments, mineral changes were observed and reactive transport modeling to study the impact of fluid-rock interactions in CO_2-geothermal systems. These studies were not specific to a particular site; geological and geothermal conditions and parameters were taken from various research sites. The aqueous presence in CO_2-based geothermal systems causes a combination of mineral dissolution and precipitation effects that could impact reservoir growth and longevity. However, the impacts of geochemical on the reservoir have been rarely studied.

Also, some studies focused to determine the reaction kinetic and rate using various lab-scale experiments and simulation models. Salvage and Yeh (1998) mathematically developed a numerical model for kinetic and equilibrium microbiological and geochemical reactions.[135] Wang (2014) provides a systematical review, to the extent possible, of recent advances in nanogeochemical research as well as recent progress in nanoscience that may bear significant implications to geochemical studies.[136] Atchley et al. (2014) investigate three-dimensional plume evolution within the non-equilibrium stages of reactive transport.[137] Heterogeneity is also considered.

2.8 Research Objectives and Goals

A range of assessments are required to develop a detailed understanding of diverse subsurface conditions and to evaluate the suitability for CO_2 storage,[138] in order to create safe short-term CO_2 storage at different subsurface reservoir conditions and to gain a better understanding of fluid and rock interaction. The aim of this study is

summarized as follows:

- Measure how different CO_2 injection rates affect mineralogical and petrophysical changes
  - Determine the short-term significant changes
  - Study the significance of iron chemistry in sandstone
  - Examine the generation of physical structures such as wormholes in limestone and dolomite
- Investigate how different reservoir conditions affect mineralogical and petrophysical changes
  - Study mineralogical and petrophysical changes in different rock types and different reactive surface areas
  - Study mineralogical dissolution at different brine concentrations
- Evaluate experimental results using reactive transport models

CHAPTER 3

EXPERIMENTAL APPARATUS AND METHODOLOGY

3.1 Core Samples

Before conducting the core flooding experiments, it was necessary to understand the composition of the core samples. The core samples were ground using a wire-saw to make powder samples. To determine these properties, X-ray diffraction (XRD) and inductively coupled plasma mass spectrometry (ICP-MS) were utilized. XRD was used to detect all relevant constituents found in the unreacted samples. For XRD analysis, the samples were mixed with deionized water (DI H_2O) and further ground in a micronizing mill until fine enough to pass through a 325 mesh screen. The solution was then applied to a glass slide using a pipette. Once the sample had dried, an XRD pattern was obtained.

Prior to ICP-MS analysis, unreacted core samples were digested using hydrofluoric acids for ICP-MS. Typically, 100 mg of solid are treated with 5 ml concentration of HNO_3 and 5 ml concentration of HF. The samples are dried, and the process repeats 2-3 times. As expected, the sandstone is primarily quartz, but contains iron, calcium, magnesium, and potassium. Limestone is dominated by the presence of calcium. Magnesium is the next most prominent cation present. Last, calcium and magnesium are distributed in dolomite as a similar component ratio. General core properties of unreacted sandstone, limestone, and dolomite cores are shown in Table 1.

Table 1. Mineralogical compositions of unreacted sandstone, limestone, and dolomite core used in the experiments

		Sandstone	Limestone	Dolomite
Composition (Based on XRD)	Kaolinite	2.51 %	-	-
	Oligoclase	1.52 %	-	-
	Clinochlore	1.08 %	-	-
	Illite	4.58 %	-	-
	Sanidine	4.20 %	-	-
	Calcite	-	99.34 %	-
	Quartz	86 %	0.49 %	0.32 %
	Dolomite	-	0.17 %	99.68 %
Elements (Based on ICP-MS)	Mg (mg/kg)	1034	3959	178764
	K (mg/kg)	1047	871	629
	Ca (mg/kg)	1703	497661	283987
	Fe (mg/kg)	4655	205	216

In the core flooding experiments with sandstone, limestone, and dolomite, each of the cores were approximately 7 inch in length and 1.5 inch in diameter. Originally, each of the sandstone, limestone, and dolomite cores were 8 inch in length. A 1 inch end section of each core was removed. These 1 inch core sections were analyzed using the helium porosimeter (Core Lab, Ultra-Pore 300) to provide the unreacted porosity. Before placing the cores in the core holder, they were wrapped with a heat shrinking material (FEP tubing) in order to isolate core pressure from the confining pressure. The core was then placed inside of the core holder and the core holder was secured inside of an oven.

For the batch reactor experiments, core plugs were taken from 1 inch cores consisting of sandstone, limestone, and dolomite. First, a 1 inch section of the 8 inch in length core was cut using a blade saw. After that, the 1 inch section was divided to two 1/2 inch sections. Multiple core plugs were taken from the one of 1/2 inch sections of the core using a drill press (3/8 inch drill bit). Two additional experiments were carried out because the surface reactions on each core plug were expected to be quite slow and not very active in the batch reactors. To increase activity, one of the simplest methods is to increase the surface area. Adding fractured and powder samples enhanced reactivity and maximized reaction rates. The core plugs were crushed and ground to provide various forms with different surface areas. The additional experiment results allowed for comparisons according to the changes in shape and also surface area.

3.2 Core Flooding System

The core flooding apparatus used in these experiments is shown in Figure 2. The main components of the experimental apparatus were a dual syringe pump system (Teledyne Technologies International Corp, ISCO D-500 series) for continuous flow, a supercritical CO_2 pump (Supercritical Fluid Technologies, INC, SFT-10), a syringe pump (Teledyne Technologies International Corp, ISCO D-500 series) for confining fluid, a core holder (Harbert Engineering, Hassler Core Cell), a high temperature oven, a pressure transducer, a back-pressure regulator (EQUILIBAR, EB1HP1), and a gas regulator.

The confining pressure was set to 3000 psi for sandstone and limestone and 3500 psi for dolomite, and the temperature of the oven was set to 60 °C. A 2% NaCl brine solution was pumped from the dual syringe pump system through a 500 ml stainless steel

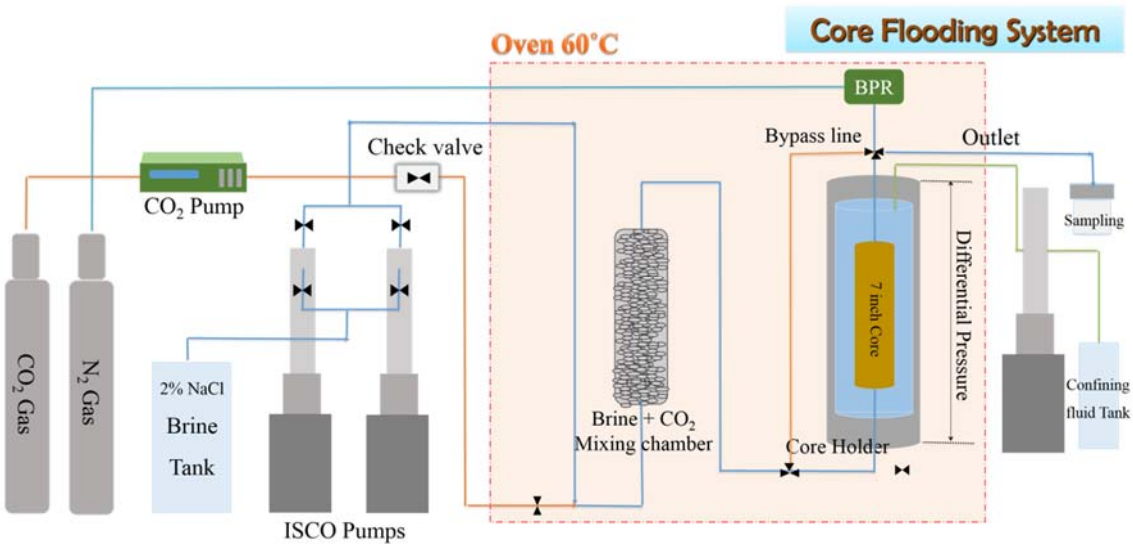

Figure 2. Schematic diagram of the core flooding system.

mixing chamber within the oven and then into the core holder. A CO_2 cylinder was attached to a supercritical CO_2 pump capable of pressurizing the CO_2 to supercritical conditions and pumping it through the system at a constant flow rate.

The 500 ml stainless steel chamber was put in place in order to facilitate in the mixing and heating of the CO_2-brine mixture before entering the core holder. The back-pressure regulator was set to 2000 psi for sandstone and limestone, and 1500 psi for dolomite using an N_2 tank. The outlet from the back-pressure regulator was directed to a product-collecting container outside the oven.

The flow rate of brine remained constant for each of the sandstone, limestone, and dolomite experiments, being 0 ml/min (blank CO_2 run), 0.5 ml/min, and 1 ml/min. The CO_2 flow rates were different. For sandstone core flooding experiments, three different CO_2 flow rates were tested – 2.82 ml/min, 1.41 ml/min, and 0 ml/min (blank brine run). For limestone and dolomite, the three different flow rates of CO_2 were – 1.41 ml/min,

0.71 ml/min, and 0 ml/min (blank brine run). The flow rates of 0 ml/min in among sandstone, limestone, and dolomite were chosen to represent a blank test to compare with other experimental results. The different flow rates were chosen to verify the hypothesis that brine with a higher CO_2 saturation would be more reactive.

3.3 Batch Reactor System

The batch reactor experiment was organized with four similarly constructed batch reactors. Each of these reactors had a pressure gauge with a maximum reading of 3000 psi, stainless steel fittings and tubing, and a valve with a maximum pressure of 3500 psi at 50 ˚C. The lower portion of the batch reactors consisted of tubing that was 1/2 inch in diameter and had a cap on the bottom end (Figure 3). This is where the sample of each rock type would presumably reside during the experiment. The valve was used as both an inlet and an outlet valve. The cap was removed from the bottom end of the 1/2 inch tubing and different rock types and forms were inserted into the bottom of the reactor, and then using a micropipette, 5 ml of brine was injected into the reactor submerging the rock samples in brine. The bottom cap was then secured and tightened. The valve cap was then removed to inject CO_2 into the reactor. The CO_2 pump outlet was attached to the reactor inlet where the valve cap was removed. The valve was opened and the reactor pressure reached the CO_2 tank pressure, which was 720-740 psi. A supercritical CO_2 pump was utilized. Prior to CO_2 injection, the pump had initially cooled for 20 minutes. After the pump was cooled, the CO_2 injection rate was increased to pressurize the reactor to around 830 psi for reactors with rock sample and to around 840 psi for the blank test.

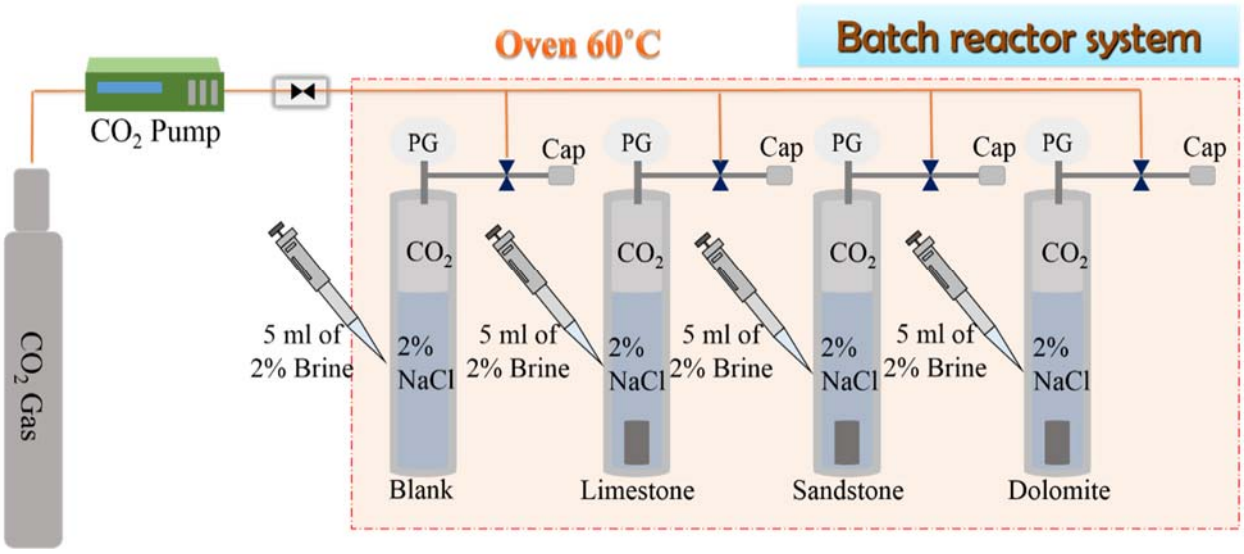

Figure 3. Schematic diagram of the batch reactor system

Once the reactors were pressurized, they were placed in an oven at 60 ˚C. The reactor pressure increased inside the oven due to the increased temperature. The pressure increase was gradual until reaching around 2400 psi. At this temperature and pressure, CO_2 entered a supercritical phase.

Within the oven, a small fan was inserted in order to keep the circulation of air constant. A thermometer was inserted into the top portion of the oven in order to easily read the internal temperature. A small rack was built in order to hold the reactors within the oven and preventing them from resting on the bottom of the oven where the main source of heat was generated.

After the two-week period was completed, the reactors were removed from the oven and cooled to room temperature. After being cooled, a small vial was placed over the opening of the valve and it was then opened, releasing the CO_2 gas and capturing the brine mixed inside of the vial. For the experiments with core plugs and fractured core

samples, the effluent was separated simply by pouring it into a vial from the reactor. The rock samples were then set aside to dry. When performing the reaction with the powder samples, a filtration system was implanted in order to separate the samples from the liquid. This was done by rinsing the reactor free of the powder with an additional 60 ml of DI H_2O. The dilution rate was measured and used to convert the ICP-MS data accordingly.

3.4 Sample Characterization

3.4.1 X-ray Diffraction (XRD)

X-ray diffraction (XRD) analyses were done at the University of Utah Energy and Geosciences Institute (EGI). EGI performed on each sample using a Bruker D8 Advance X-ray diffactometer. Phase quantification using the Rietveld method was performed using TOPAS software, developed by Bruker AXS. The Rietveld method fits the peak intensities calculated from a model of the crystalline structure to the observed X-ray powder pattern by a least squares refinement. This is done by varying the parameters of the crystal structures to minimize the difference between the observed and calculated powder patterns. Because the whole powder pattern is taken into consideration, problems of peak overlap are minimized and accurate quantitative analyses can be obtained.

The following operating parameters were used when analyzing the bulk samples: Cu-K-α radiation at 40 kV and 40 mA, 0.02˚ 2θ step size, and 0.6 seconds per step, for bulk samples. Bulk samples were examined from 4 to 65˚ 2θ. The instrument is equipped with a lynx eye detector which collects data over 2.6 mm, rather than at a point, greatly increasing X-ray counts collected and decreasing acquisition time; and a rotating sample

stage, which increases the mineral grain orientations encountered by the incident electron beam.

3.4.2 Quantitative Evaluation of Minerals by Scanning Electron Microscopy (QEMSCAN)

In order to compensate for the limits of XRD, Quantitative evaluation of minerals by scanning electron microscopy (QEMSCAN) analysis was conducted for the pre- and post- experiment core. The analysis was completed on a QEMSCAN 4300, which is built on a Zeiss Evo 50 SEM platform with four light elements BrukerX flash energy dispersive X-ray detectors. Energy dispersive X-ray spectral analysis (EDX) involves the interpretation of secondary X-ray spectra to determine elemental composition, and ultimately mineralogy. This instrument is currently iMeasure v.5.3 software for the data acquisition, and iDiscover v.5.3 for the spectral interpretation and data processing. The measurements were collected in field-scan mode, and X-ray data were collected every four on the polished thin sections. Prior to each analysis, standard instrument tuning was performed, including beam focusing, beam alignment, and calibration of the X-ray detectors and backscatter. A measurement procedure is entered and the analyses are automated. The QEMSCAN was operated using a accelerating voltage 20 kV and a specimen current of approximately 5 nA.

3.4.3 Inductively Coupled Plasma Mass Spectrometer (ICP-MS)

The determination of iron, calcium, magnesium, and potassium was performed using a quadrupole inductively coupled plasma mass spectrometer (Agilent, 7500ce) with

a double-pass spray chamber; PTFE 100 µl/min nebulizer, platinum cones, and sapphire injector within a quartz shielded torch.[139] The sample handling and chemistry was performed in laminar flow benches. An external calibration curve containing iron, calcium, magnesium, and potassium was freshly prepared from 1000 mg/l single elemental standard solutions in HNO_3 (Inorganic Ventures). Both the samples and the calibration solutions were prepared in 2.4 % HNO_3 (BDH Aristair Plus). Indium at a concentration of 20 ppb was added to calibration curve, samples, and blanks as internal standard. Samples were diluted 1:200 and run in the ICP-MS using 4 ml He/min in the collision cell. Silicon was determined on a separate run, with the samples diluted 1:2. Chloride was determined using an ion chromatograph (Metrhom 881).

3.4.4 Helium (He) Porosimeter

Samples for the helium porosimeter were prepared by cutting a 1 inch core section from the end of an 8 inch in length core with a 1.5 inch in diameter. This was done for twelve different 8 inch in length cores, four each for sandstone, limestone, and dolomite. The top and bottom of these 1 inch core sections were then leveled using a grinder. The average diameter and thickness of each core section was measured and a "caliper bulk volume" measurement was calculated. This measurement is based on the assumption that the core section is a cylinder. The core sections were exposed to an air stream in order to clear off excess dust and particles that resulted from using the grinder. A matrix cup connected to the helium porosimeter was then used to calculate the grain volume (GV) and calculate the pore volume (PV) and porosity (ϕ) of sandstone, limestone, and dolomite core sections. After measuring the grain volume of a core

section, the porosimeter program then calculated the pore volume using the following equation:

$$Pore\ Volume = Bulk\ Volume - Grain\ Volume \quad (2)$$

The computer program then calculated the porosity of the core section using:

$$\phi = \frac{Bulk\ Volume - Grain\ Volume}{Bulk\ Volume} = \frac{Pore\ Volume}{Bulk\ Volume} \quad (3)$$

Before each use, the helium porosimeter was calibrated using five calibration disks with different volumes. A ten-point calibration was performed before analyzing each set of core sections. Each core section was measured for porosity five different times and the average porosity of each core section was then calculated.

3.4.5 Micro-Computed Tomography (Micro-CT)

Application of the computed tomography at the microscale level (microtomograp hy) allows for the quantitative examination of porosity changes.[140-142] A Micro-CT (The XCT-400) was used for 7 inch limestone core samples. XCT-400 method is based on a 3D reconstruction from one-thousand 2D radiographs of the X-ray attenuation properties of various materials forming an object.[143] The optical system used in the experiment provides an optical resolution of 42 microns. Each data set is 1014×1024×1012 voxels. To measure porosity change in core plug samples, a Micro-CT (XCT-400) was also used. The optical system used in the experiment provides an optical resolution of 1.85 microns.

The reconstruction provides 3D images of the X-ray absorption by the different materials in the sample. Each data set is 986×1005×968 voxels. Different magnification levels were utilized in analyzing the samples: 4X for core plugs. For 4X, 80 kV of voltage and 9 seconds of exposure time were used.

3.4.6 Surface Area Analysis (BET)

The BET surface area and porous structure of the various types and forms of core samples were determined by the single point BET/Nitrogen (N_2) method based on the quantity of gas that adsorbs as a single layer of molecules on the rock surface at a temperature of -196 ˚C using a Micrometric Tristar II. Approximately, 0.6 g of each sample was loaded into a glass sample tube. Immediately preceding surface area analysis, the samples were degassed at a minimum temperature of 100 ˚C for at least 4 hours on the degassing station. A mixture of 30 % N_2 / 70 % Helium (He) was used as a gas supply and analyses were carried out at atmospheric pressure and at liquid N_2 temperature.

CHAPTER 4

MINERALOGICAL CHANGES IN CORE FLOODING SYSTEM

4.1 Core Analysis: X-ray Diffraction

X-ray diffraction (XRD) was used to detect mineralogy found in the unreacted and reacted sandstone core samples with different CO_2 injection rate in core flooding system. XRD spectra present a different intensity of mineralogy before and after the experiment, especially in quartz. However, the trends do not change significantly because there are no changes of crystallization and structure in the quartz.

In order to compare quantitative differences, one method is measure the unreacted dominate mineral intensity before and after the reaction. For the mineralogical composition of sandstone core samples (see Table 1), quartz is the dominant mineral. The quartz intensity in each sandstone core was determined before and after the reaction under different CO_2 flow rate conditions. The unreacted core includes around 86 % of quartz. The quartz does not react with supercritical CO_2 and brine solution. In XRD analysis, the mineralogical percentages are based on the relative amount of each mineral in the sandstone sample. This means when the quartz intensity is increasing relatively, the concentration of other minerals such as kaolite, illite, smectite are decreasing relatively; dissolving in the effluent. However, the intensities of the other minerals are not significant because the XRD analysis is more of a bulk measurement, and does not

accurately detect the small changes.

Based on the XRD spectra of quartz (Figure 4), the quartz intensity is affected by the CO_2 injection rate. The unreacted sandstone and the brine without CO_2 intensities are similar around 25000. The brine with CO_2 at a low flow rate (1.41 ml/min) shows a higher intensity around 35000, and the brine with CO_2 at a high flow rate (2.82 ml/min) has the highest intensity around 40000. Concluding that at higher CO_2 flow rates the quartz intensity is increased further showing that reactive lower concentration minerals were dissolved.

XRD spectra (Figure 5 and Figure 6) of unreacted and reacted limestone and dolomite core samples were also taken. Due to the high quantities of calcite minerals in

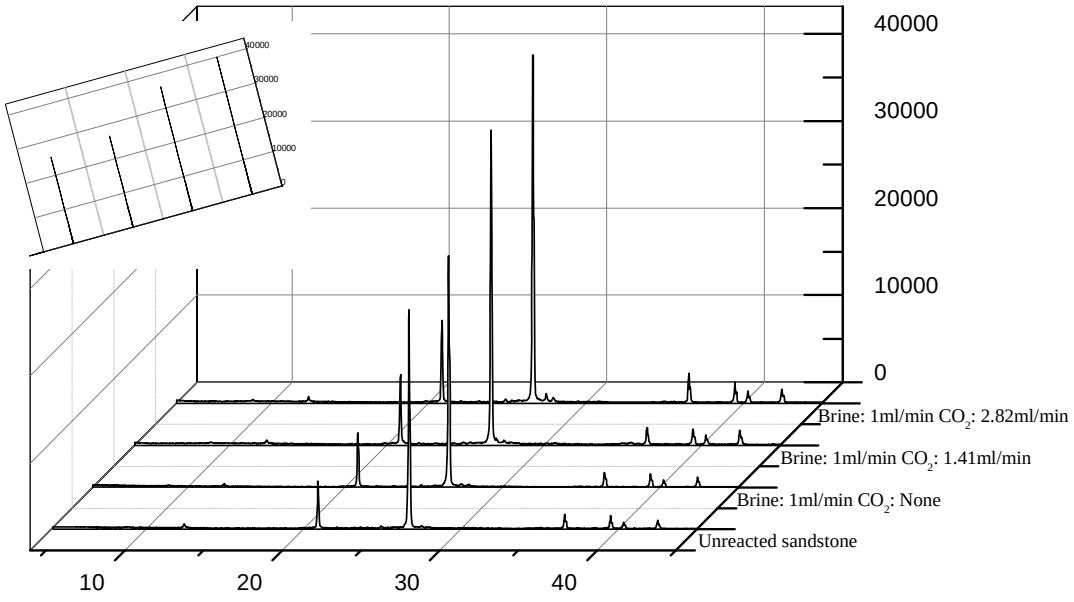

Figure 4. XRD Spectra lines of unreacted and reacted sandstone core samples under various CO_2 injection rate conditions

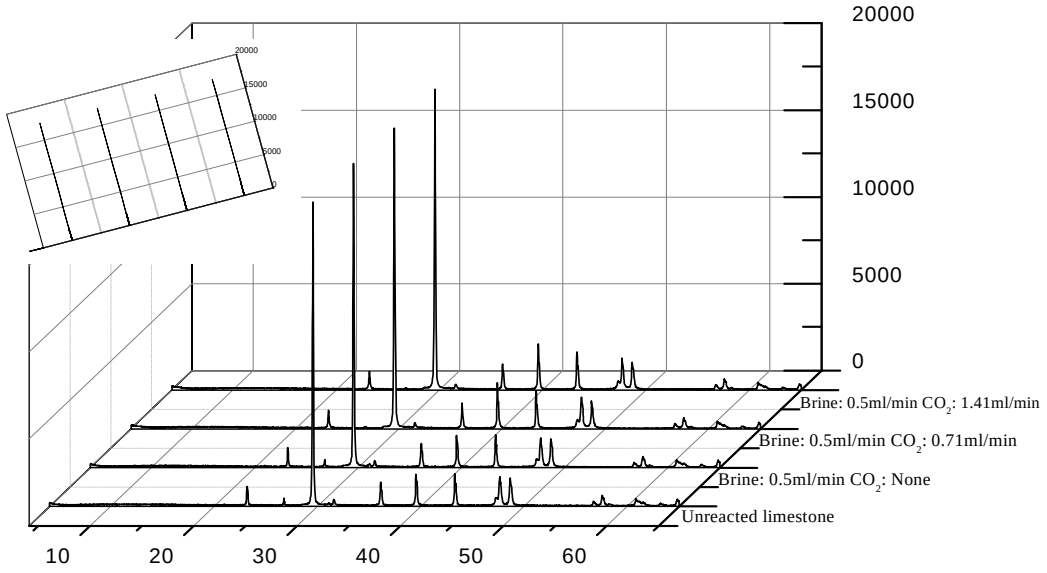

Figure 5. XRD Spectra lines of unreacted and reacted limestone core samples under various CO_2 injection rate conditions

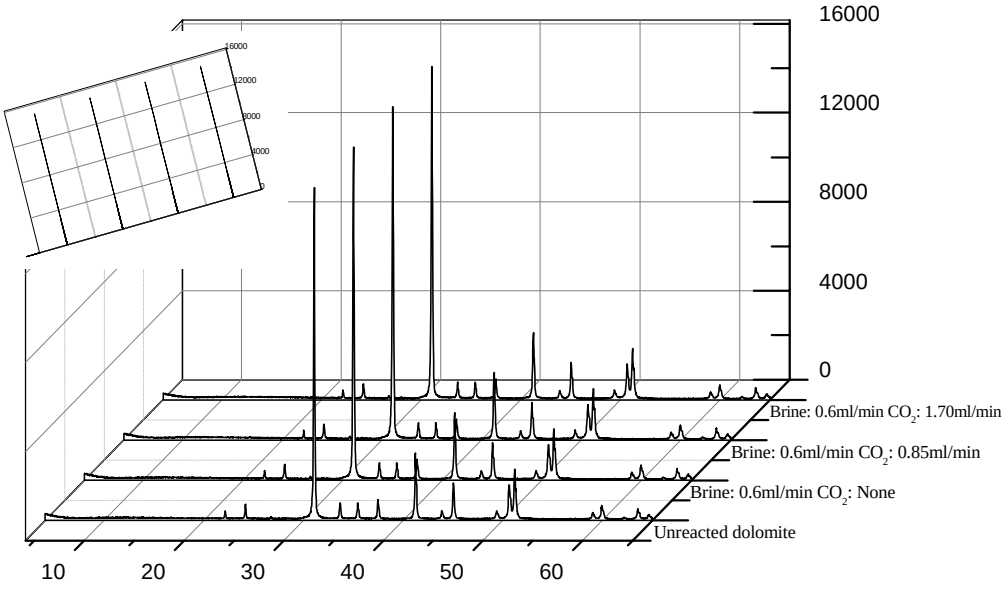

Figure 6. XRD Spectra lines of unreacted and reacted dolomite core samples under various CO_2 injection rate conditions

limestone and dolomite minerals in dolomite, the XRD spectra data showed the intensity of calcite remained relatively constant 99.34 % in limestone core samples and the intensity of dolomite remained relatively constant 99.28 % in dolomite core samples. Because of the limitations of XRD data as a bulk measurement the small changes in the calcite and dolomite intensities are not enough to make a conclusion for limestone and dolomite.

4.2 Core Analysis: QEMSCAN Imaging

In order to compensate for the limits of XRD, QEMSCAN analysis was conducted. For QEMSCAN analysis, each reacted core was divided into 21 sections making 63 sections in total or 63 total data points. Figure 7 contains an image of each core divided into 21 sections each. Sections 1-21 make up the blank core, sections 22-42 make up the low CO_2 flow rate core, and sections 43-63 make up the high CO_2 flow rate core.

Figures 8-13 show mineral concentrations based on QEMSCAN results. The QEMSCAN analysis confirmed that quartz is the dominate mineral in sandstone with minor amounts of illite, kaolinite, smectite, chlorite, siderite, and ankerite. Overall, the mineralogical distributions in the rock are evenly distributed throughout.

A QEMSCAN of the unreacted sandstone core showed that the cores were comprised of approximately 6% by area illite, 3% by area kaolinite, 0.9 % and 0.8 % by area chlorite and smectite, and less than 0.2 % by area siderite and ankerite. The compositions of the unreacted core are represented by a solid line in each figure. After the reaction with brine and no CO_2 (Figure 8), QEMSCAN showed that illite concentrations

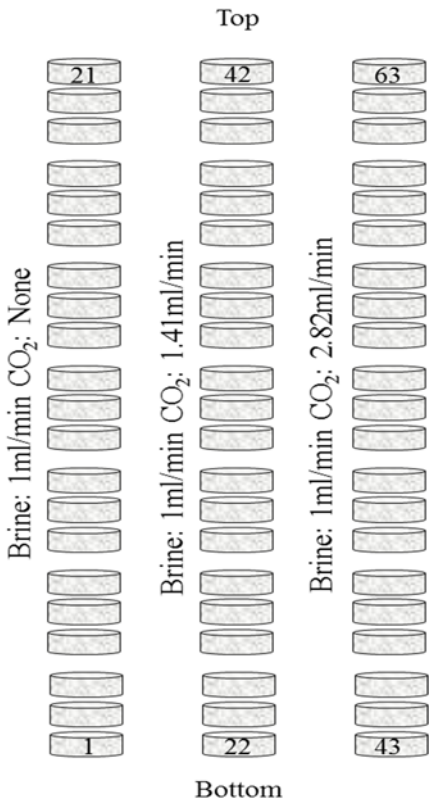

Figure 7. Sandstone post-experimental cores divided into 21 sections for QEMSCAN analysis. Sections 1-21 make up the blank core, sections 22-42 make up the low CO_2 flow rate core, and sections 43-63 make up the high CO_2 flow rate core

at the bottom of the core decreased but not so much as it progressed up the core, meaning brine reacted initially with illite but less reaction took place further up the core. After the reaction, around 5% by area illite remained in the core. Kaolinite concentration remains relatively constant after the brine only experiment. The other minerals believed to be the iron source in sandstone are presented in Figure 9. There are no significant concentration changes in these minerals after the brine only experiment.

When brine and CO_2 are injected at 1 ml/min and 1.41 ml/min, respectively, the illite concentration decreased to around 4% throughout the entire core. Kaolinite concentration remains unaffected and the concentration stays around 3 % (Figure 10).

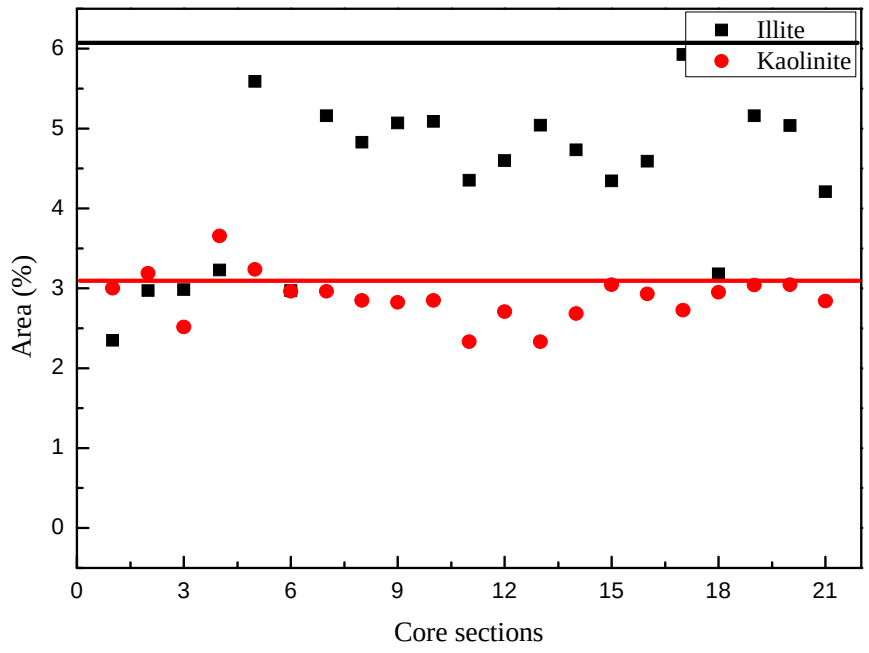

Figure 8. Illite and kaolinite concentrations (Area %) of each reacted core section under brine only condition; acquired through QEMSCAN analysis

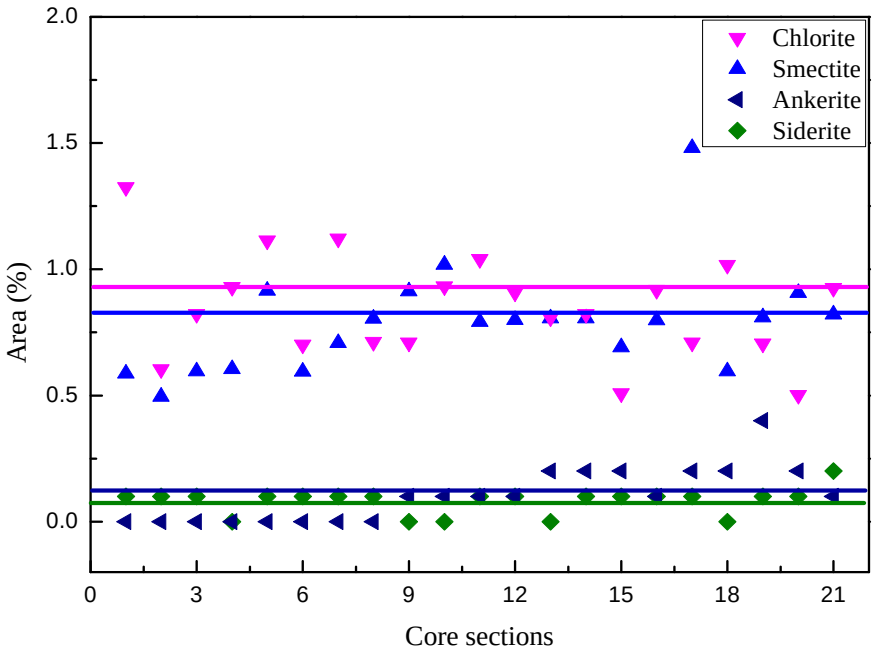

Figure 9. Smectite, chlorite, siderite, and ankerite concentrations (Area %) of each reacted core section under brine only condition; acquired through QEMSCAN analysis

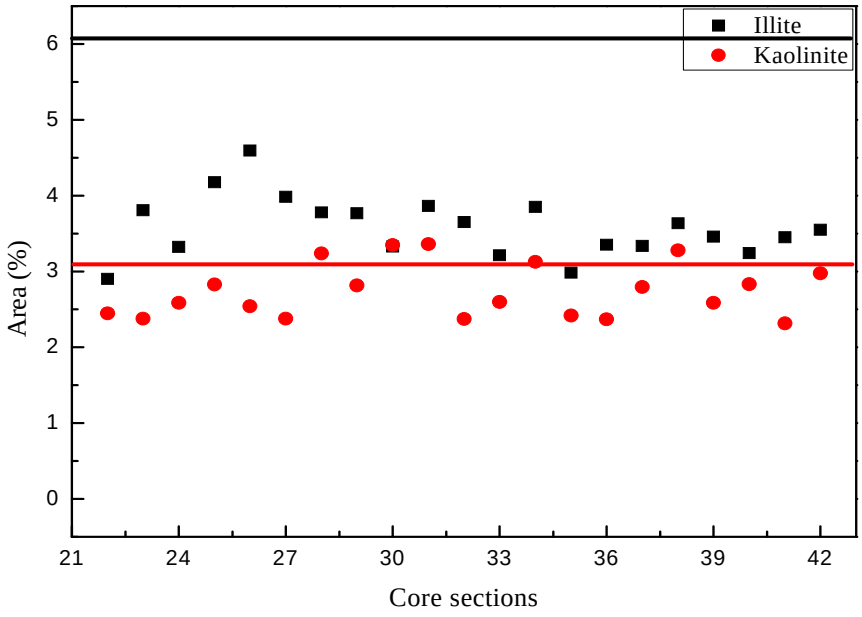

Figure 10. Illite and kaolinite concentrations (Area %) of each reacted core section under 1 ml/min brine and 1.41 ml/min CO_2 injection conditions; acquired through QEMSCAN analysis

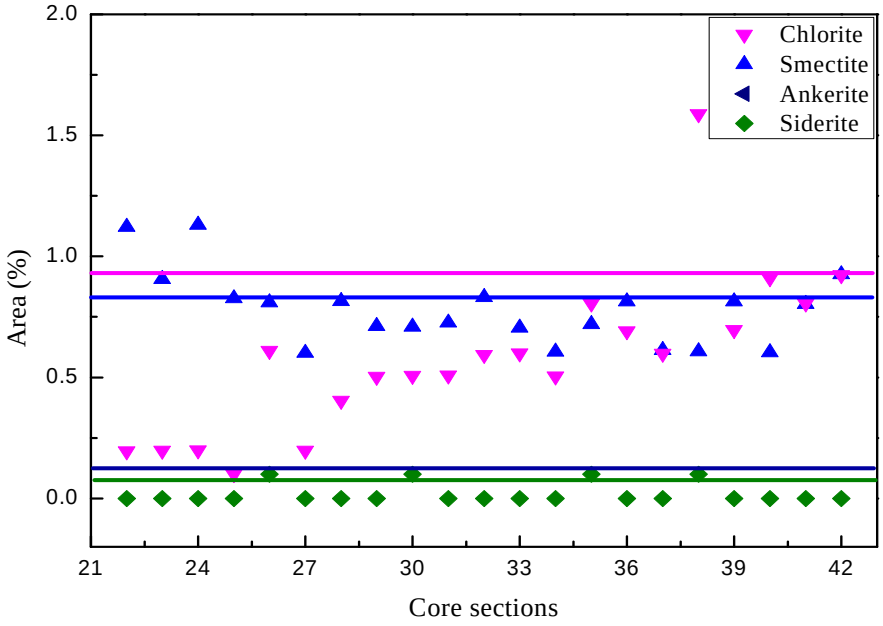

Figure 11. Smectite, chlorite, siderite, and ankerite concentrations (Area %) of each reacted core section under 1 ml/min brine and 1.41 ml/min CO_2 injection conditions; acquired through QEMSCAN analysis

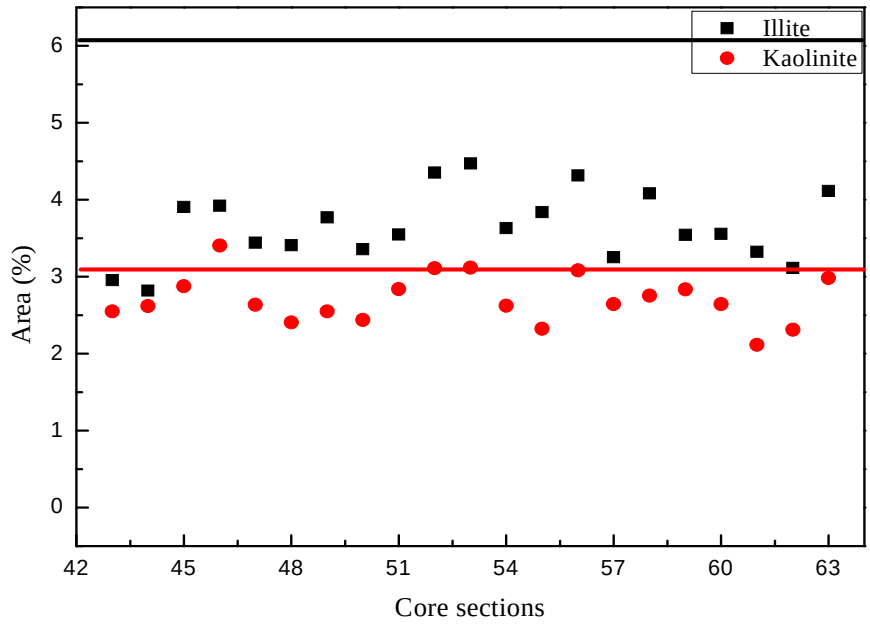

Figure 12. Illite and kaolinite concentrations (Area %) of each reacted core section under 1 ml/min brine and 1.41 ml/min CO_2 injection conditions; acquired through QEMSCAN analysis

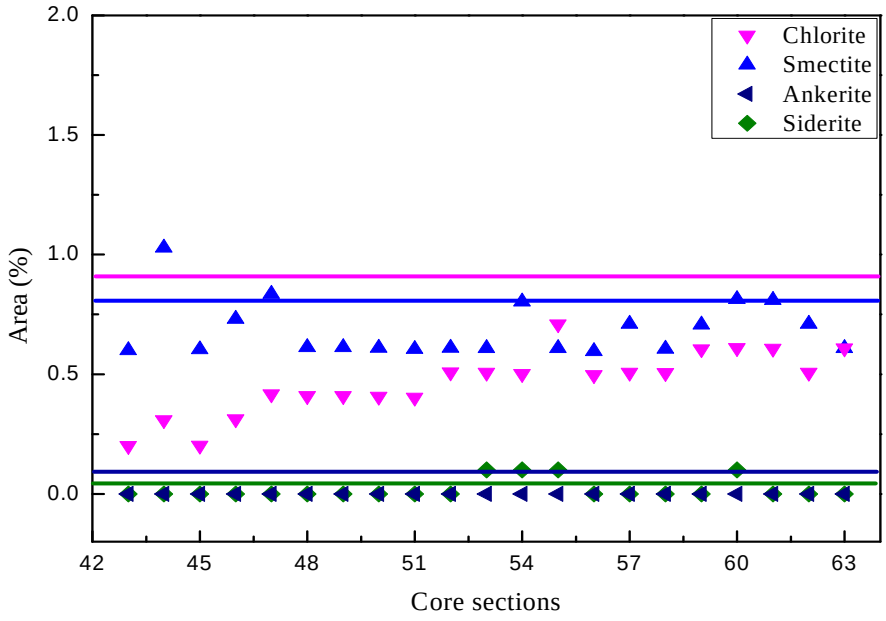

Figure 13. Smectite, chlorite, siderite, and ankerite concentrations (Area %) of each reacted core section under 1 ml/min brine and 2.82 ml/min CO_2 injection conditions; acquired through QEMSCAN analysis

Figure 11 shows the iron containing minerals. Smectite concentration remains constant around 0.7 % and chlorite concentration is decreased more in the inlet section around 0.2 % and around 0.8 % at the outlet section. Ankerite and siderite are completely dissolved after the injection of brine and CO_2.

After the CO_2 injection flow rate was increased to 2.82 ml/min and brine injection rate remained at 1 ml/min, illite dissolution was increased. Illite concentration had decreased to around 3.7 %. Kaolinite concentration remained unchanged around 3 %, (Figure 12). Figure 13 shows that smectite was slightly dissolved in this experiment. Smectite concentration decreased to around 0.6 %. Chlorite concentration decreased throughout the entire core. The trend is similar to the previous injection rate (CO_2 1.41 ml/min and brine 1 ml/min), but the overall concentration is slightly lower, 0.2 % at the inlet section and 0.5 % at the outlet section. At this flow rate, condition siderite and ankerite were completely dissolved as in the case of CO_2 injection of 1.41 ml/min and brine injection of 1 ml/min.

4.3 Effluent Analysis: ICP-MS

To begin the core flooding experiment, the brine was pumped through the system to the pressure set by the back-pressure regulator; the outlet line would remain dry. Once the pressure of the system reached target pressure about 1500 to 2000 psi, the first drops of effluent would pass through the outlet line and into the product collecting container. Post-experiment fluid samples were taken and analyzed to ensure that brine chemistry, component analysis, and concentration measurements between rock and brine were achieved.

In preliminary tests on a sandstone core, the product collecting container was changed once every day and a sample of this outlet fluid was then analyzed using ICP-MS. This preliminary data suggested that for most minerals, the content was high in the beginning of the experiment and decreased as time elapsed. To more fully understand how these mineral concentrations changed over injected pore volume, it was necessary to divide the samples into smaller increments and view the concentrations in a more continuous manner. It was hypothesized that most of the concentration changes would occur within a short span of time and after this time had elapsed the change in concentration would be slow. To ascertain this more continuous view of mineral concentration, the outlet container was changed as follows: every 1 hour for 24 hours, every 2 hours for 12 hours, every 4 hours for 12 hours, every 8 hours for 24 hours, and then every 24 hours for the remainder of the experiment. These results allow us to make conclusions about the mineralogical concentrations as experimental time proceeds.

pH values for all of the effluent samples were within the 5.2 to 5.6 range. Each of the collected fluids was analyzed using ICP-MS. The mineralogical concentrations of iron, calcium, magnesium, and potassium have been plotted over time for sandstone in Figures 14-17 for limestone in Figures 18-21 and for dolomite in Figures 22-25, respectively. In each of the mineral concentrations plotted, the blank test tends to have relatively low values for the elements throughout the time period with the exception of a few large spikes at the beginning of the experiments.

The results of the iron concentration in the sandstone experiments with low and high CO_2 flow rates are of particular interest (Figure 14). It is seen from Table 1 that the iron concentration in sandstone was about 4655 ppm. The source of iron is a combination

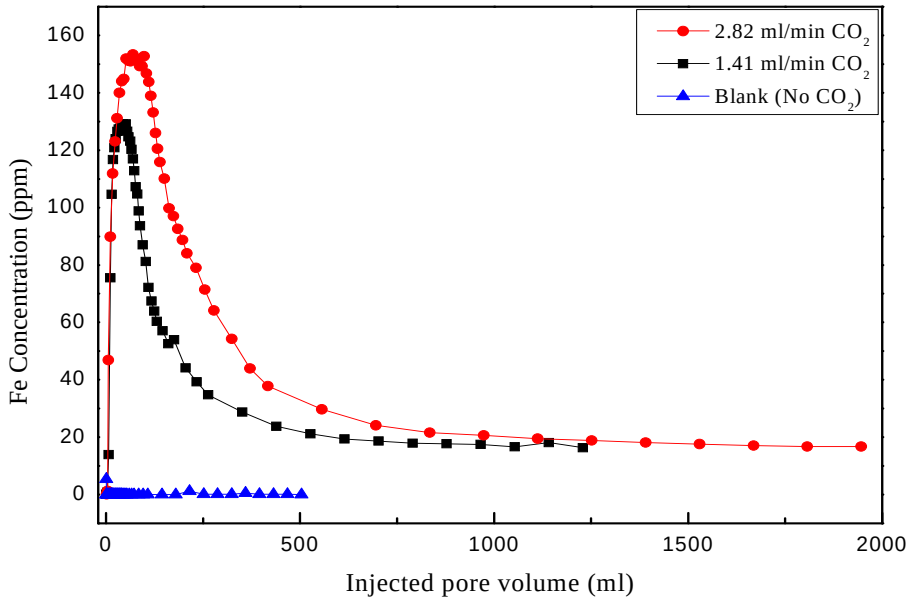

Figure 14. Concentration of iron ions as measured by ICP-MS in the effluent for sandstone flooding experiments

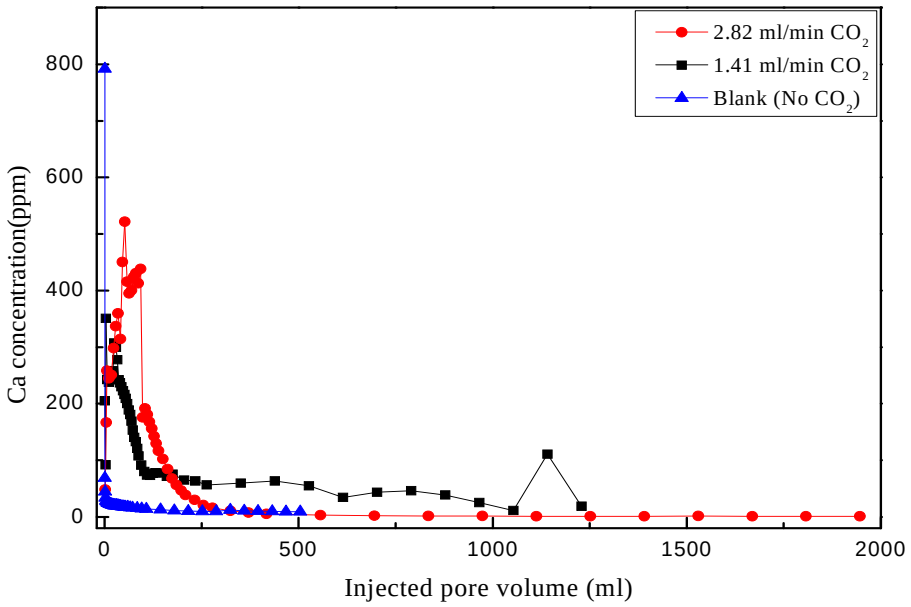

Figure 15. Concentration of calcium ions as measured by ICP-MS in the effluent for sandstone flooding experiments

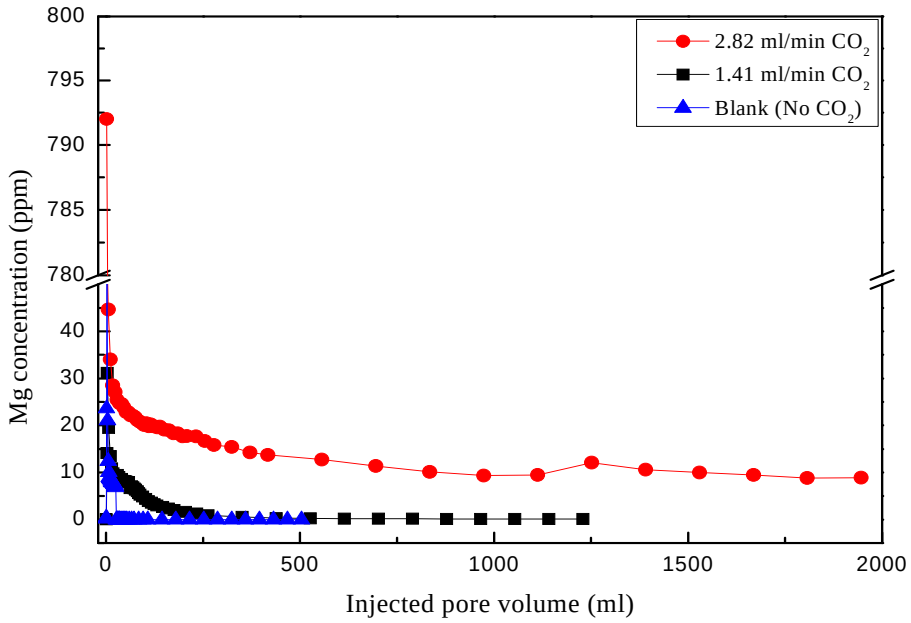

Figure 16. Concentration of magnesium ions as measured by ICP-MS in the effluent for sandstone flooding experiments

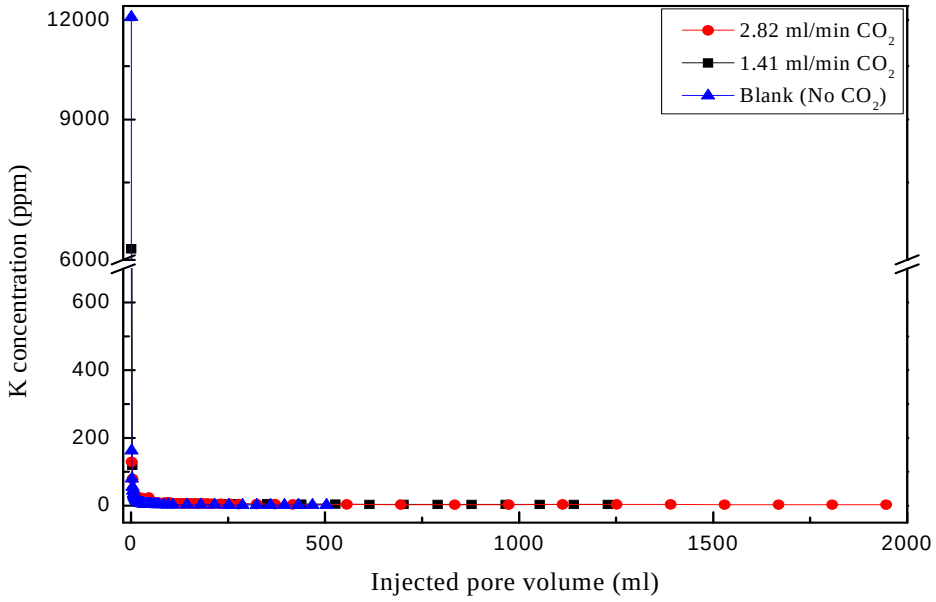

Figure 17. Concentration of potassium ions as measured by ICP-MS in the effluent for sandstone flooding experiments

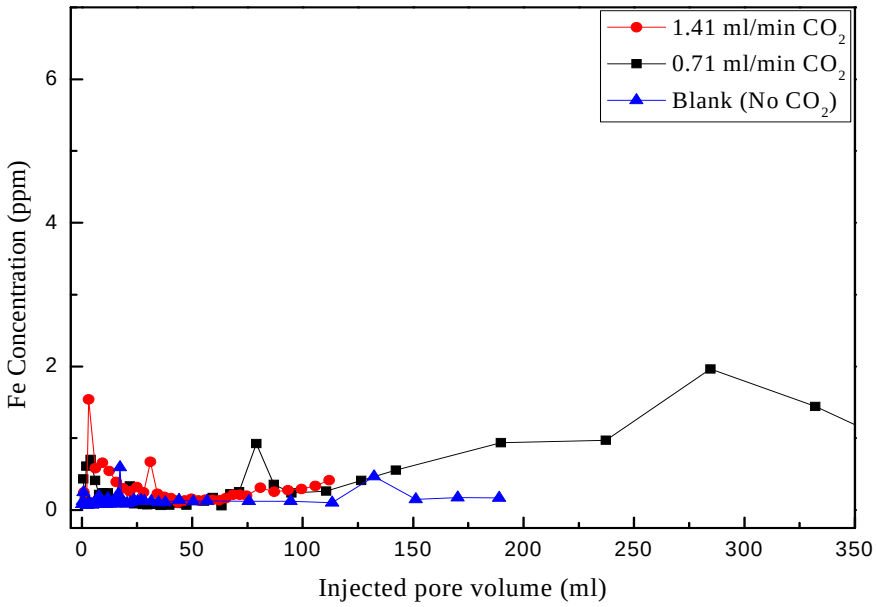

Figure 18. Concentration of iron ions as measured by ICP-MS in the effluent for limestone flooding experiments

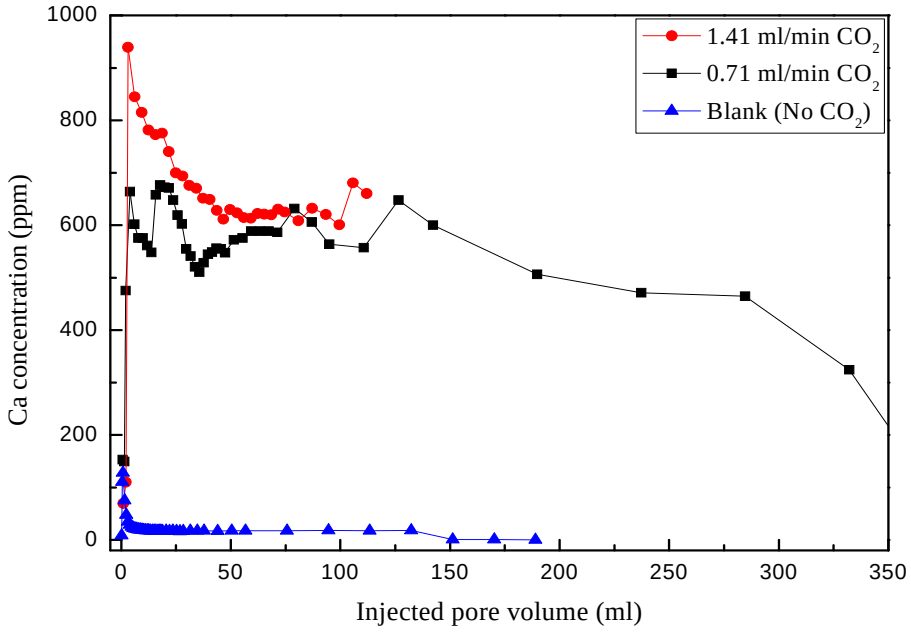

Figure 19. Concentration of calcium ions as measured by ICP-MS in the effluent for limestone flooding experiments

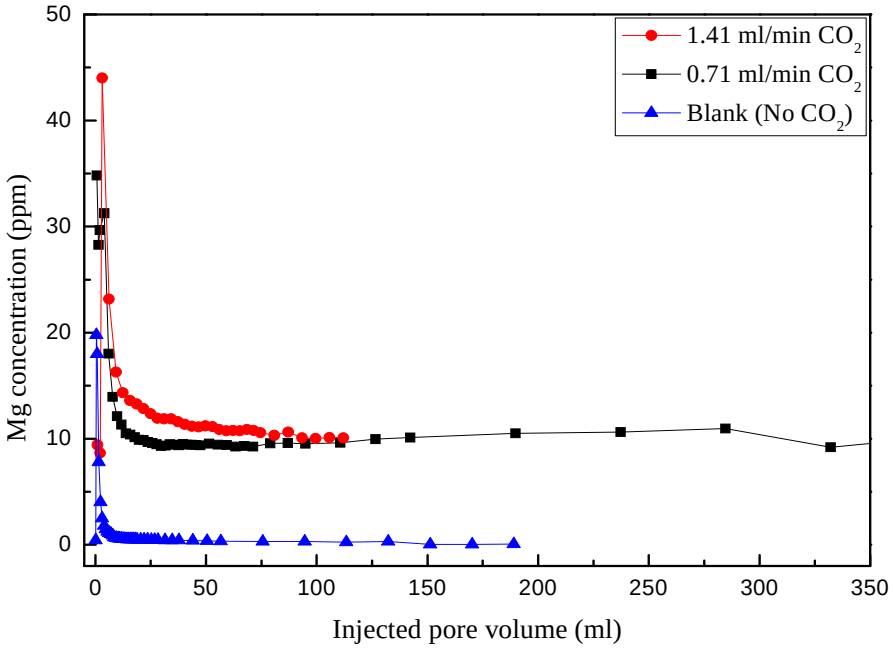

Figure 20. Concentration of magnesium ions as measured by ICP-MS in the effluent for limestone flooding experiments

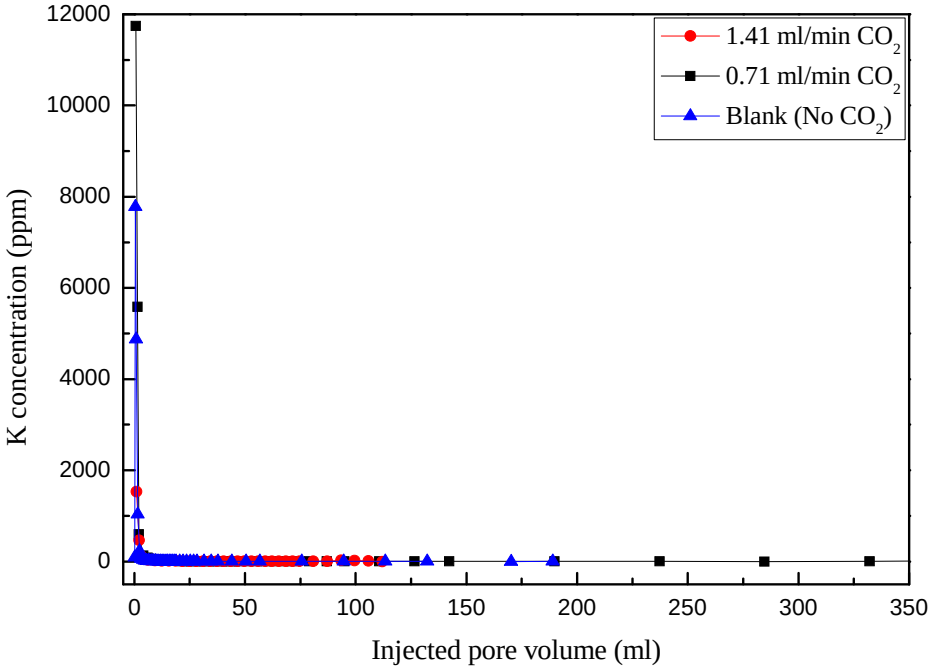

Figure 21. Concentration of potassium ions as measured by ICP-MS in the effluent for limestone flooding experiments

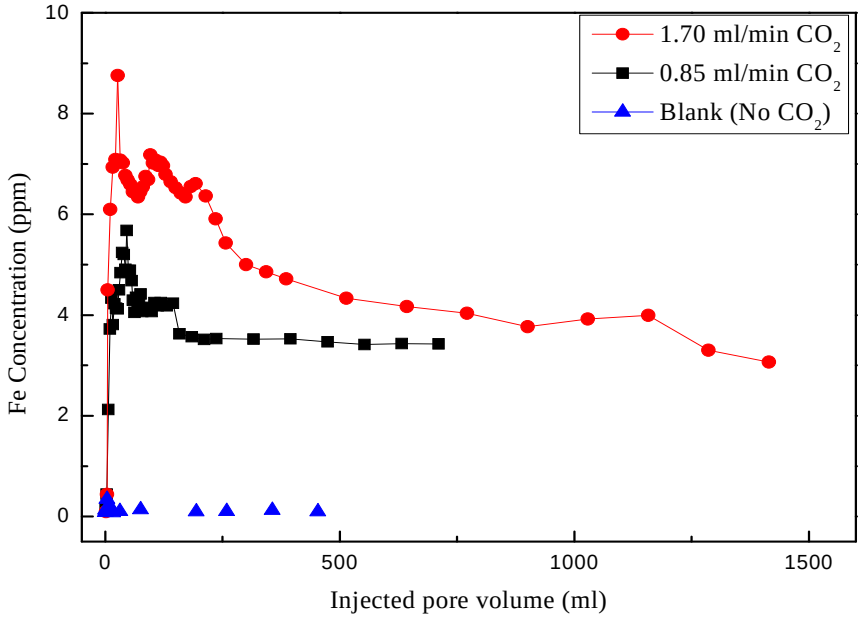

Figure 22. Concentration of iron ions as measured by ICP-MS in the effluent for dolomite flooding experiments

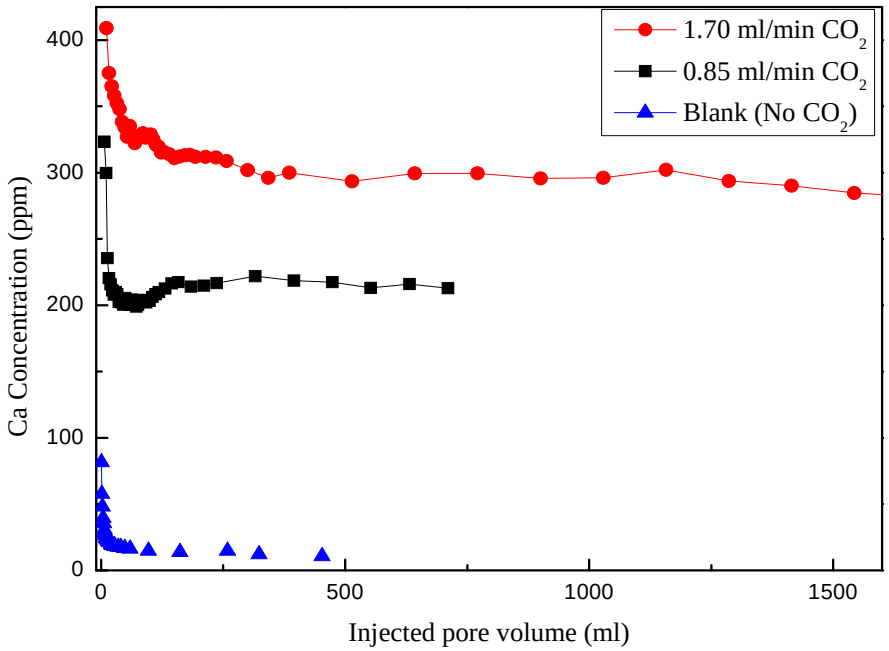

Figure 23. Concentration of calcium ions as measured by ICP-MS in the effluent for dolomite flooding experiments

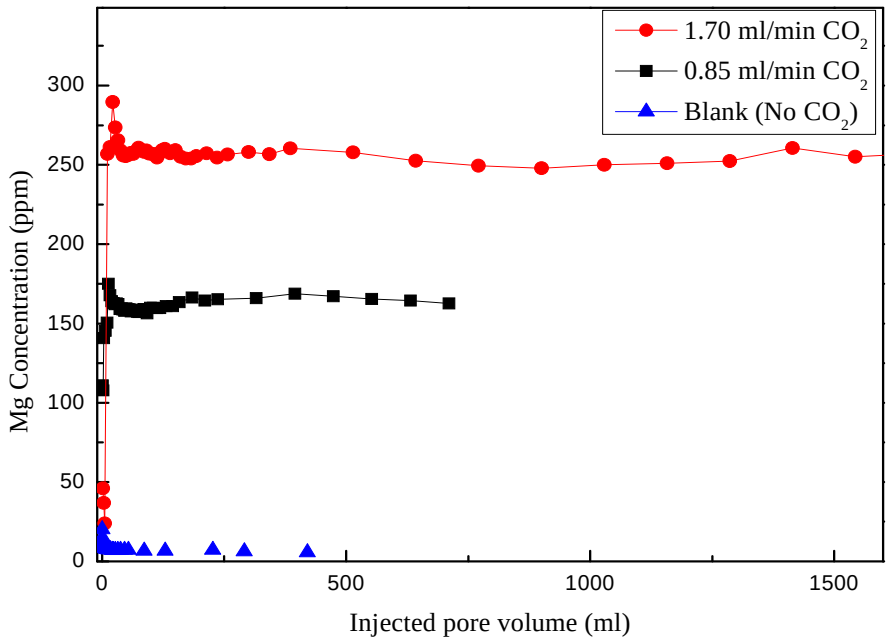

Figure 24. Concentration of magnesium ions as measured by ICP-MS in the effluent for dolomite flooding experiments

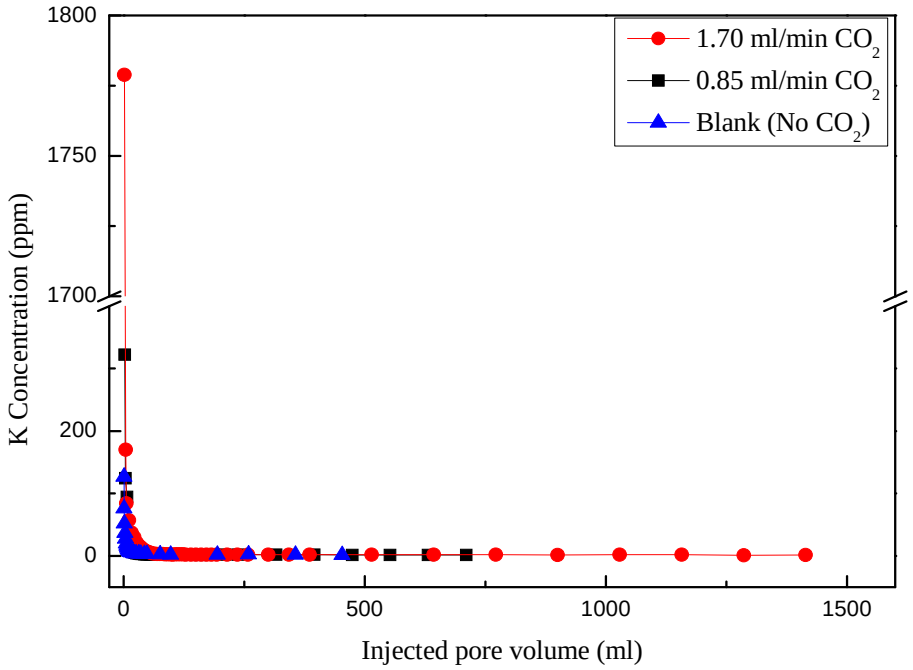

Figure 25. Concentration of potassium ions as measured by ICP-MS in the effluent for dolomite flooding experiments

of minerals such as ankerite, siderite, smectite, and illite. Both of the flow rates exhibit the same trends in their iron concentrations, although the concentrations of iron in the higher CO_2 flow rate are higher at each point. The concentrations begin near zero and then increase rapidly until reaching a smooth peak. After reaching the smooth peak, the iron concentration begins to decrease but at a more gradual rate. Eventually, the rate of change in the iron concentration begins to taper off and the concentration begins to become steadier towards the end of the experimental time. Interestingly, the final iron concentration of each flow rate is approximately the same. From these results, it can be determined that the higher flow rate of CO_2 results in greater iron reactivity from the minerals within the sandstone core. This suggests that the decrease in pH that results from an increase in CO_2 concentration contributes to the greater dissolution of iron in sandstone.

Sandstone does contain some calcite, which is the source of the calcium cations. Figure 15 show the trend is an increase in calcium concentration at the beginning of the experiment and then a continual decrease until it reaches a steady concentration towards the end of the experiment. The result for the higher flow rate of 2.82 ml/min is especially interesting because the final concentration that it reaches is near zero, whereas the steady concentration for the lower flow rate of 1.41 ml/min is quite a bit higher at around 50 ppm. The changes in effluent concentrations for the different flow rates are a result of the competing reaction (dissolution) and transport phenomena. The magnesium concentrations in the sandstone effluent samples initially decrease rapidly in concentration until approaching a much lower rate of change (Figure 16). When both magnesium concentrations level off, the concentration of magnesium from the higher

CO_2 flow rate remains higher than the magnesium concentration from the lower flow rate. This indicates a lower rate of dissolution of magnesium containing minerals. The potassium concentrations in the sandstone effluent samples peak quickly and decrease to low ppm values, again indicating dissolution process (Figure 17).

Effluent concentrations of iron, calcium, magnesium, and potassium, for limestone are shown in Figure 18-21, respectively. The iron concentration in the limestone effluent samples is much lower when compared to the sandstone effluent samples (Figure 18). Concentration differences of iron at the two different CO_2 flow rates are not significant. The limestone core is mainly calcite, based on the XRD analysis, and does not include a high percentage of iron based minerals.

Predictably, the calcium concentrations in the limestone effluent samples are much higher (Figure 19). The concentration of calcium increases rapidly with both the high CO_2 and low CO_2 flow rates. The experiment with high CO_2 flow rate was stopped after around 48 hours. This was due to excessive dissolution on one edge of the core at the core holder inlet. Due to the dissolved section of the core, the confining fluid began to generate a small pinhole within the heat shrinking tube at this location. Once the confining pressure had penetrated the heat shrinking tube, the confining pressure and core pressure began to equalize. When this occurred the experiment could not properly proceed under the desired conditions. When comparing the first 36 hours of the low CO_2 and high CO_2 flow rates, it is apparent that the higher CO_2 flow rate results in a large concentrations of calcium in the limestone effluent samples.

This effect is similar to the iron concentrations in that it suggests that the pH of the working fluid affects the reactivity of the minerals. The concentration of calcium in

the effluent does appear to be stable at around 600 ppm, even for higher CO_2 flow rate. This would be in contrast to the results of the sandstone calcium concentrations that display lower concentrations of calcium in the high CO_2 flow rate effluent samples towards the end of the experiment. This is attributed to the much higher concentration of calcium in limestone and a relatively low calcium concentration in sandstone.

In the limestone samples, the magnesium concentrations for both the low and high CO_2 flow rates remain quite similar throughout the first 36 hours (Figure 20). As time progresses, the concentrations begin to approach a steady concentration with the concentration with the high CO_2 flow rate being only slightly above the magnesium concentration with the low CO_2 flow rate. The concentration of magnesium in the unreacted limestone sample was higher than that of the magnesium concentration in the unreacted sandstone sample. Figure 21 shows concentrations of potassium peak early in limestone floods as well, and decrease to low ppm values within 24 hours. The steady concentrations are attained more rapidly than in the sandstone floods.

Dolomite contains a significant amount of calcium and magnesium as a similar component ratio. Concentrations of iron, calcium, magnesium and potassium for dolomite are shown in Figures 22-25. The iron concentration in the dolomite effluent samples is similar when compared to the limestone effluent samples (Figure 22). Concentration differences of iron at the two different CO_2 flow rates look like significant, but actual value is a couple of ppm difference. It is because the dolomite core is mainly dolomite mineral ($CaMg(CO_3)_2$) based on the XRD analysis, and does not include a high percentage of iron based minerals.

Predictably, the calcium concentrations in the dolomite effluent samples are much

higher (Figure 23). The concentration of calcium increases rapidly with both the high CO_2 and low CO_2 flow rates. The experiment with high CO_2 flow rate was stopped after around 240 hours. This was due to excessive dissolution on bottom of the core at the core holder inlet similar to the limestone core flooding experiment. A pinhole was generated in the heat shrinking tubing similar to the pinhole generated in limestone, but unlike limestone, there was no wormhole created in the dolomite cores. The pinhole was possibly created due to the size of the pores on the exterior of the dolomite cores increasing the chances of a pinhole developing in the tubing. When comparing between low and high CO_2 flow rates, it is apparent that the higher CO_2 flow rate results in a large concentrations of calcium in the dolomite effluent samples. The higher CO_2 injection rate means that more fluid passes through the core facilitating greater reaction opportunity within the core. The concentration of calcium in the effluent is initially around 400 ppm but decreases to 300 ppm where it appears to be stable at higher CO_2 flow rate. At lower CO_2 flow rate, calcium concentrations begin slightly above 300 ppm then decreasing to just above 200 ppm where the concentration stabilizes. This result is similar to that of limestone, where the calcium concentration began high then decreased to a stabilized value. Also the concentrations of calcium in limestone and dolomite from the ICP-MS data are consistent with the XRD data such that limestone is almost completely comprised of calcium and the composition of dolomite is almost even values of calcium and magnesium. Therefore, the concentration of calcium in limestone is nearly double the concentration of calcium in the dolomite effluent samples.

The magnesium concentrations and calcium concentrations follow a similar trend (Figure 24). The trend is that the concentration begins high and stabilizes to a lower

value. The difference being the magnesium concentration is lower than the calcium concentration. This is because of the ratio of calcium and magnesium in dolomite. This result is consistent to the calcium and magnesium ratio from the XRD data. Concentrations of potassium peak early in dolomite effluent as well, and decrease to low ppm values within 24 hours (Figure 25). The potassium concentrations are essentially the same in each of the effluent samples.

The overall higher flow rates used in the sandstone, limestone, and dolomite experiments likely have an effect on the amount of mineral dissolution. Relative abundance of each of the minerals, reaction rates with individual minerals, and reactive flow aspects, all contribute to the relative differences in ionic concentrations observed at the outlet.

4.4 Summary

Core flooding experiments were performed with different injection rates of a CO_2 and brine mixture through sandstone, limestone, and dolomite host rocks. Higher CO_2 injection rates led to higher levels of mineral dissolutions. The cores were analyzed using XRD to measure the intensity of dominate minerals. In sandstone, quartz intensity showed a difference. However, in limestone and dolomite cores, there was not a noticeable intensity change. Dissolution of minerals was a significant result in the experiments based on the QEMSCAN data. Ankerite and siderite were the main iron bearing reactive minerals in sandstone and they dissolved almost completely in the two-week experiment. ICP-MS data showed effluent peaks of the key cations such as iron, calcium, and magnesium. The level of iron dissolution in sandstone – even over short

durations was higher than expected – may have major implications in practical sequestration scenarios. As expected, calcite was mainly dissolved in limestone core and calcium and magnesium were dissolved from dolomite mineral in dolomite core. The dolomite mineral composition ratio was $(Ca_{0.6}Mg_{0.4})CO_3)_2$ based on the ICP-MS results.

CHAPTER 5

PETROPHYSICAL CHANGES IN CORE FLOODING SYSTEM

5.1 Core Analysis: Porosity Measurements

Originally, each of the sandstone, limestone, and dolomite cores measured 8 inch in length. However, the end of a 1 inch section of these cores was removed and both the top and bottom of this 1 inch section were made flat using a grinder. These 1 inch core sections were then analyzed using the helium porosimeter. The average porosity of the four sandstone, limestone, and dolomite core sections make up the “average porosity of unreacted sandstone, limestone, and dolomite,” respectively.

The porosity measurements were made using the helium porosimeter described earlier. In general, each core section was measured for porosity five different times and the average porosity of each core section was then calculated. The average porosity values are stated as the porosities for pre reaction core samples. After the core flooding experiments were completed, each of the four sandstone and five limestone, and three dolomite cores were then cut into seven equal sections each measuring under 1 inch. The top and bottom of each of the core sections were made flat using a grinder, with the exception of the inlet and outlet sides of the core. The porosity of each core section was then determined using the helium porosimeter. Before analysis in the helium porosimeter, the core sections were exposed to an air stream and lightly brushed (not including the

inlet/outlet sides) in order to clear off excess dust and particles that resulted from using the grinder and saw.

Helium porosimeter data show the porosity change of the sandstone, limestone, and dolomite cores after core flooding experiments (Figures 26-28), respectively. Four core flooding experimental conditions were set up brine without CO_2, CO_2 only after saturating the core with brine, and brine and CO_2 flowing together. A higher porosity implies greater pore volume and thus a greater amount of mineral dissolution. After helium porosimeter analysis, brine without CO_2 and CO_2 only after saturating the core with brine showed no significant porosity changes. The experiments with brine and CO_2 flowing together showed much higher porosity changes. To compare the porosity change, the porosities of the seven 1 inch core sections was averaged and compared with the unreacted core porosity. In the core flooding experiments, there appears to be a porosity reduction in some sections of the cores followed by mild dissolution. This is believed to be due to two possibilities. One of the believed possibilities after the minerals partially dissolved and precipitated in sections. Izgec et al. also observed dissolution followed by precipitation in carbonates. The other possibility is rock heterogeneity.

Mineral dissolution appears during core flooding experiment with all different core samples (see Chapter 4). Also, in all cases, the porosity at the inlet is greater than the porosity at the outlet. This results shows that the reactivity is greater at the inlet due to the fresh brine and CO_2 solution continuously reacting with the core after that the mixing fluid has some reacted minerals proceeding up the core decreasing reactivity. Especially, dissolution does not significantly appear in sandstone under the brine without CO_2 and CO_2 only after saturating the core with brine conditions, 0.18 % and 0.12 %, respectively

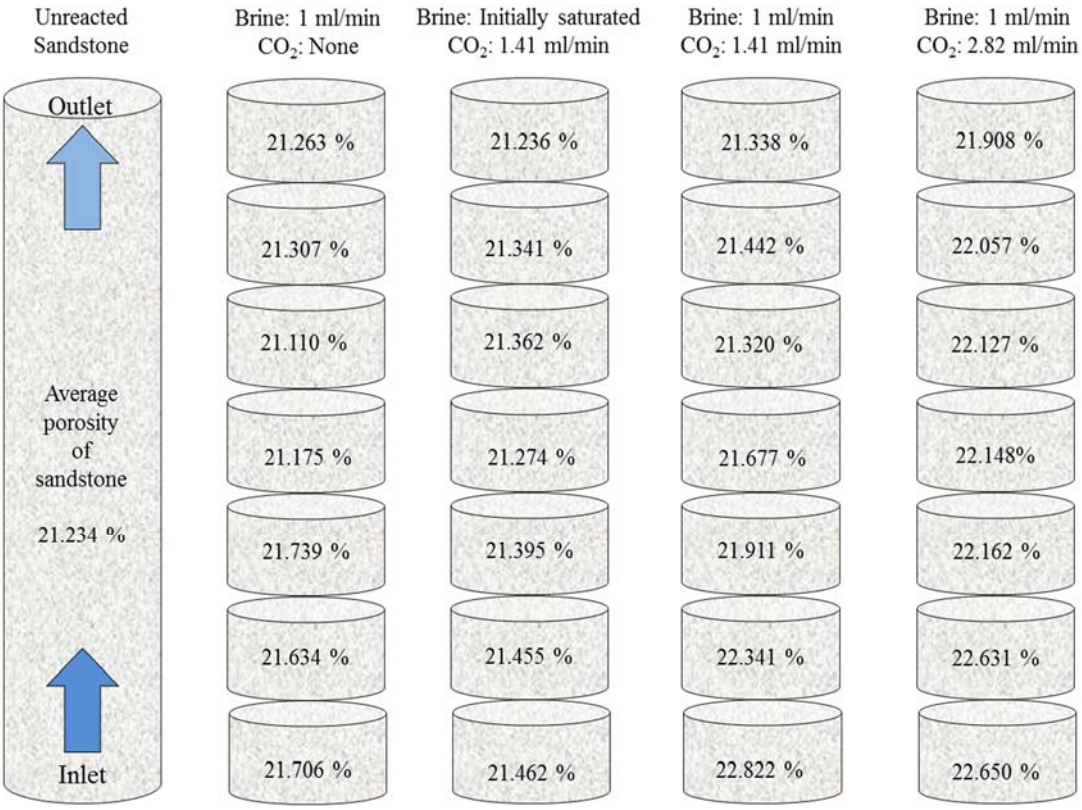

Figure 26. Porosity changes of different sections in sandstone using He porosimeter

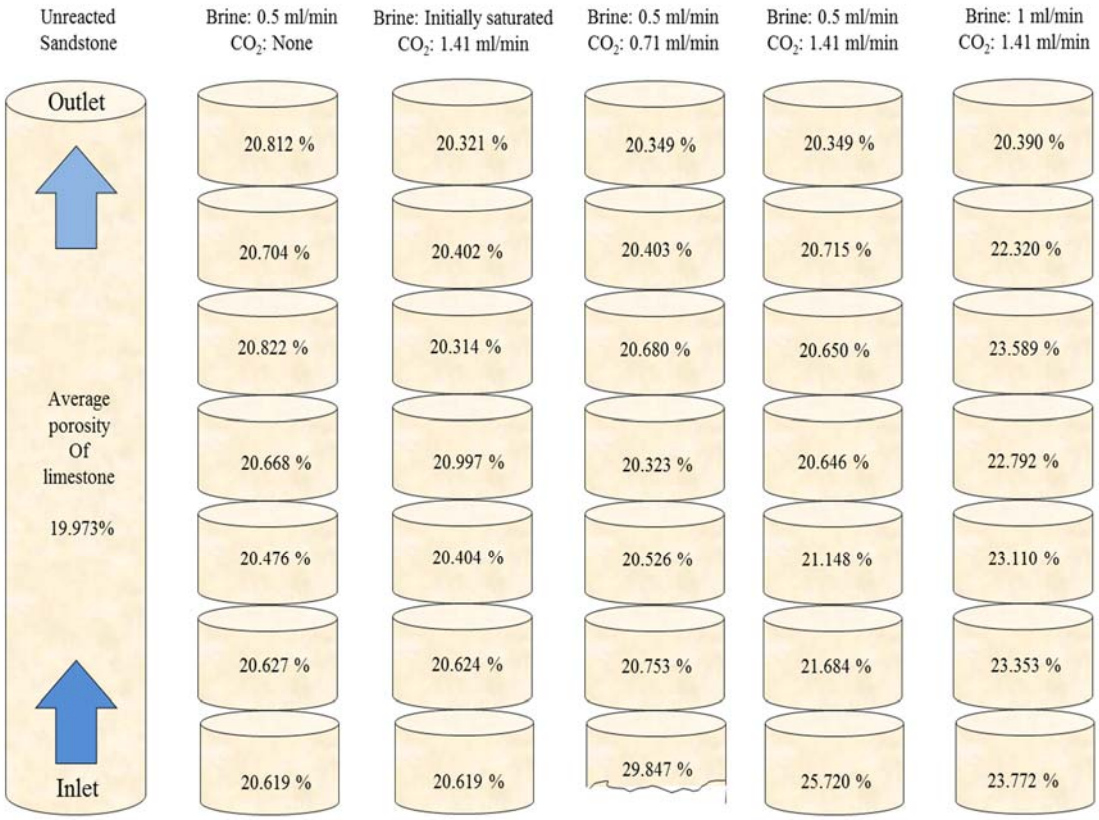

Figure 27. Porosity changes of different sections in limestone using He porosimeter

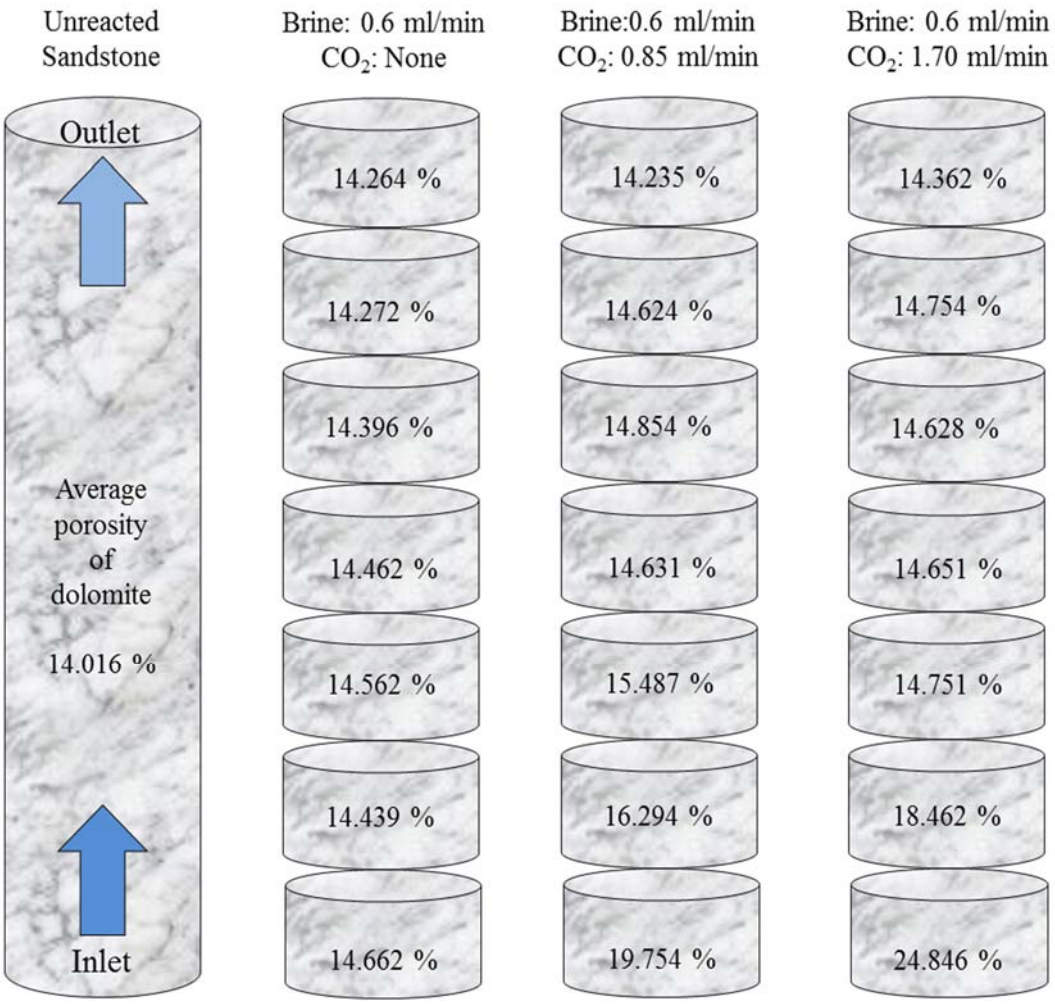

Figure 28. Porosity changes of different sections in dolomite using He porosimeter

(Figure 25). When brine and CO_2 were injected together, the porosity change is greater than the previous conditions but only slightly: 0.60 % for 1.41 ml/min CO_2 flow rate and 1.01 % for 2.82 ml/min CO_2 flow rate. The greater porosity change under the higher CO_2 flow rate condition is consistent with the ICP-MS data results, showing more reactivity at higher CO_2 flow rates.

In limestone, the porosity increase is consistent in all the experiments indicating the expected dissolution (Figure 27). Also, in all cases, the porosity at the inlet is greater than the porosity at the outlet as in the sandstone core samples. Little dissolution appears in limestone under the brine without CO_2 and CO_2 only after saturating the core with brine conditions, 0.70 % and 0.55 %, respectively. When different ratio of brine and CO_2 were injected together, the porosity change is much greater. When the injection rate of brine is 0.5 ml/min and CO_2 is 0.71 ml/min, the porosity change is 5.46 %. The high increase is due to the high dissolution in the bottom section of the core. As in the sandstone, the reactivity is much greater at the inlet and this section in the limestone was almost completely dissolved at this flow ratio. The residence time is increased at this flow ratio, therefore the fluid can react with the inlet section longer. When average core porosity is calculated without the bottom section, the porosity change is around 1.12 %. When the CO_2 injection rate is increased to 1.41 ml/min (brine remains at 0.5 ml/min), the porosity change is 1.59 %. Under these injection conditions, the inlet core section was also partially dissolved but not the extent of the previous core. When brine injection rate is increased to 1 ml/min (CO_2 remains at 1.41 ml/min), the porosity change is 2.79 %. Under these injection conditions, the residence time increases and the reactive fluid is able to penetrate up the core further causing a greater overall porosity change. With the

comparison of the inlet sections, there is an increase in porosity change as the mixing flow rates decrease. This evidence shows that the increase in residence time with the inlet core section translates to a greater reactivity with this section as mixing flow rate decreases. These porosity changes correlate with the ICP-MS data results, showing more reactivity at higher brine and CO_2 flow rates.

During preliminary experiments at the same injection conditions as the sandstone and limestone experiments, it was discovered that the core pressure nearly reached the pressure of the confining fluid. The increased pressure is caused by the low porosity within dolomite compared with sandstone and limestone. Due to safety issues, the experiments could not be run at these conditions; therefore, different injection conditions were selected. The injection rates selected go as followed: brine 0.6 ml/min for every experiment, CO_2 at 0 ml/min, 0.85 ml/min, and 1.70 ml/min. In the dolomite experiments, there is not a CO_2 only after saturating the core with brine result because a dolomite core with a consistent mineralogical composition was unavailable. In dolomite, in all cases, the porosity at the inlet is greater than the porosity at the outlet, like in the other two rock samples. The porosity increase is consistent in all the experiments indicated in Figure 28.

Dissolution does not significantly appear in dolomite under the brine without CO_2 condition; the porosity change is 0.42 %. When brine and CO_2 were injected together, the porosity change is greater than 1.58 % when the CO_2 flow rate is 0.85 ml/min and 2.52 % when the CO_2 flow rate is 1.70 ml/min. Similar to the limestone cores, the inlet sections of dolomite were also greatly dissolved. This dissolution is due to the rate at which the reactive fluid is passing through the core. As more fresh reactive

fluid passes through the core section, more of that section is dissolved. The greater porosity change under the higher CO_2 flow rate condition is consistent with the ICP-MS data results, showing more reactivity at higher CO_2 flow rates.

5.2 Core Analysis: Permeability Calculation

Comprehensive fluid flow studies were conducted through a single fracture to investigate the validity of cubic law.[144] Idealized fracture models were constructed by assuming that the fracture planes had contact area and roughness. The flow in a fracture is usually characterized by the classical cubic law equation, equation (4).

$$Q = 5.11 \times 10^6 \left[\frac{d\Delta P w^3}{L\mu}\right] \quad (4)$$

This equation neglects the matrix permeability compared to the fracture permeability. As a result, the classical cubic law does not account for any flow occurring through the matrix and assumes that the flow occurs entirely through the fracture. This assumption holds for low permeability reservoirs.

When fluid was injected through 7 inch in length different cores at fully saturated and at steady state conditions, pressure difference between injecting and producing ends is automatically recorded. According to Darcy's law, equation (5), permeability can be calculated by:

$$k_m = \frac{\mu Q L}{A\Delta P} \quad (5)$$

where μ is the viscosity of the fluid, Q is the volumetric flow rate of the fluid, L is the length of the core, A is the cross-sectional area, ΔP is the pressure difference between the inlet and outlet of the core. When water was injected through the fractured core, the average pressure difference due to the presence of fracture was obtained. According to Darcy's Law, average permeability in the fractured core can be calculated by, equation (6):

$$k_{avg} = \frac{\mu Q L}{A \Delta P_{avg}} \tag{6}$$

Table 2 shows the different core properties and the results obtained from experiments with different cores and the calculated permeability values, respectively. The viscosity of the fluid was assumed to be the same as pure water because the brine concentration was low. Matrix permeability was calculated using equation (6). The average differential pressure was calculated by averaging the differential pressure over each time step. The permeability changes are shown in Figures 29-31. Unreacted core permeability of sandstone, limestone, and dolomite is around 90 mD, 150 mD, and 25 mD, respectively. After the reaction, permeability changes in sandstone (Figure 29) are 0.21 % for the brine only experiment, 0.76 % for the 1 ml/min brine + 1.41 ml/min CO_2 experiment, and 1.43 % for the 1 ml/min brine + 2.82 ml/min CO_2 experiment. Permeability changes in limestone (Figure 30) are 1.06 % for the brine only experiment, 1.48 % for the 0.5 ml/min brine + 0.71 ml/min CO_2 experiment, 1.72 % for the 0.5 ml/min brine + 1.41 ml/min CO_2 experiment, and 3.42 % for the 1 ml/min brine + 1.41

Table 2. Different core properties and experimental flow rate conditions

	Length	Diameter	Fluid
Sandstone	17.78 cm	3.81 cm	1 ml/min brine
Sandstone	17.79 cm	3.80 cm	1.41 ml/min CO_2 + 1 ml/min brine
Sandstone	17.78 cm	3.80 cm	2.82 ml/min CO_2 + 1 ml/min brine
Limestone	17.73 cm	3.80 cm	1 ml/min brine
Limestone	17.76 cm	3.82 cm	0.71 ml/min CO_2 + 0.5 ml/min brine
Limestone	17.77 cm	3.81 cm	1.41 ml/min CO_2 + 0.5 ml/min brine
Limestone	17.74 cm	3.81 cm	1.41 ml/min CO_2 + 1 ml/min brine
Dolomite	17.83 cm	3.81 cm	0.6 ml/min brine
Dolomite	17.86 cm	3.81 cm	0.85 ml/min CO_2 + 0.6 ml/min brine
Dolomite	17.82 cm	3.81 cm	1.70 ml/min CO_2 + 0.6 ml/min brine

ml/min CO_2 experiment. In the limestone experiments, a wormhole was generated causing the rapid increase in permeability over a short time period, less than 3 days. Permeability changes in dolomite (Figure 31) are 0.51 % for the brine only experiment, 1.69 % for the 0.6 ml/min brine + 0.85 ml/min CO_2 experiment, and 2.41 % for the 0.6 ml/min brine + 1.70 ml/min CO_2 experiment.

5.3 Core Analysis: Micro-CT Imaging

Analysis via Micro-CT was performed on the unreacted and reacted 7 inch in length limestone cores, but not for the 7 inch in length sandstone and dolomite cores. The Micro-CT machine was only capable of supplying the necessary amount of energy to

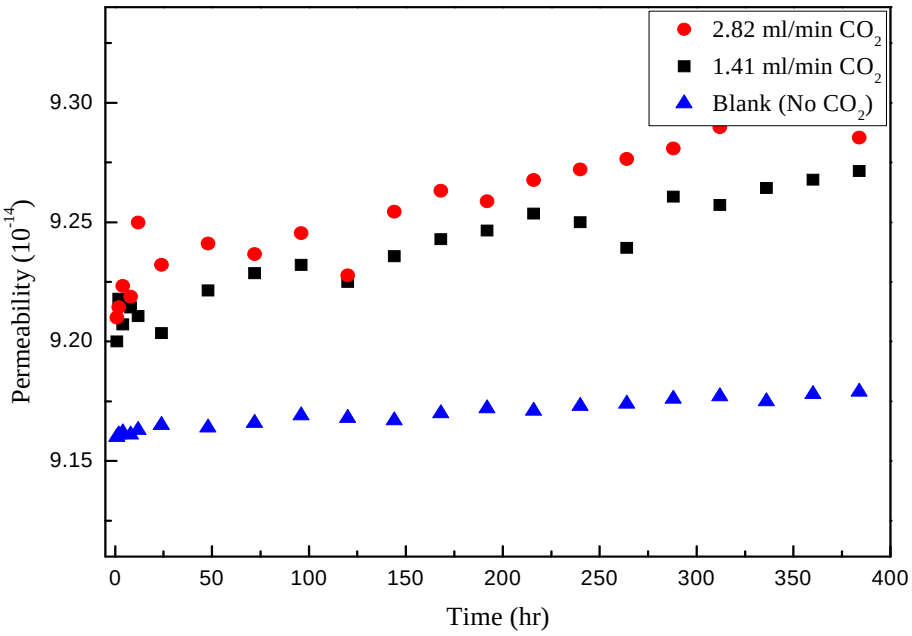

Figure 29. Permeability change in sandstone at different experimental conditions

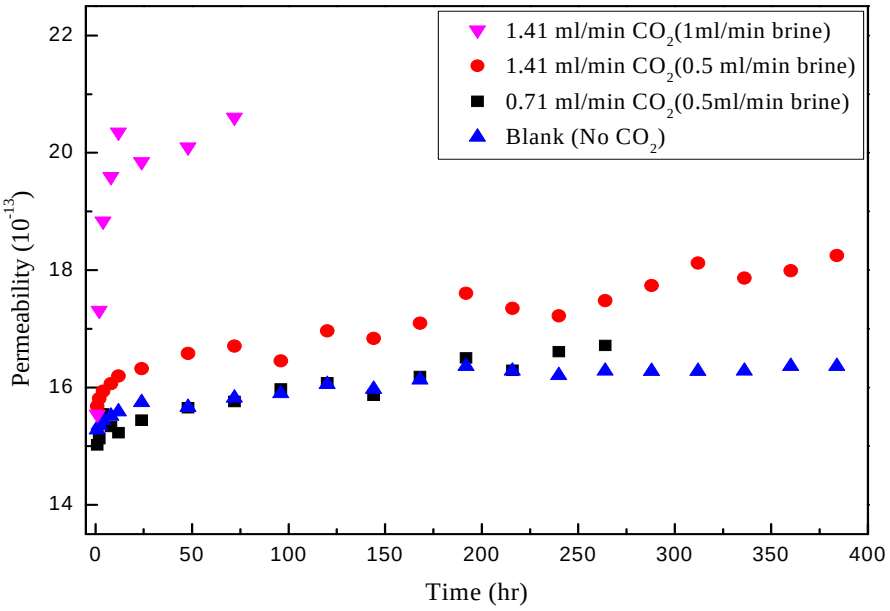

Figure 30. Permeability change in limestone at different experimental conditions

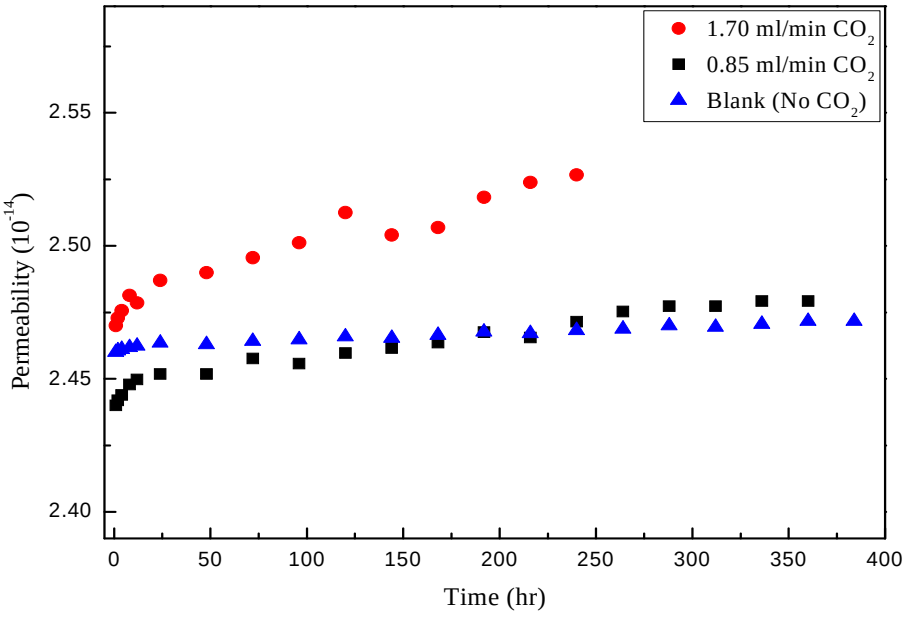

Figure 31. Permeability change in dolomite at different experimental conditions

penetrate the limestone cores with a 42 micron resolution. The energy required to penetrate the sandstone and dolomite cores was too great and thus could not be accomplished within a reasonable resolution. Four different scans of each core were taken - inlet, outlet, and two in between. Due to the angle limitations of the scanning device, a continuous scan of the entire core was not possible and small gap exists between each scanned section. The angle limitation also results in a distorted image on both ends of the scan due to the lower energy exhibited at both of the extremes of the angle range. Most of these distortions are not displayed for simplicity; however, the effect can be seen at both ends of each scan as per the rounded edges and solid coloring. The four different scans were taken at the same location for each reacted and unreacted core. The images have been displayed so as to properly see the porosity of each core section. Micro-CT scans a

surface generating a 2D raw image. The 2D raw images from Micro-CT were very dark and difficult to interpret. The brightness quality of the 2D raw images was improved using MIPAV software. After brightness was improved in all the images, they became much easier to interpret. Nothing more was altered other than the brightness of the images. The enhanced 2D images were then stacked on top of each other in order to generate a 3D image using different software called Drishti v2.4. Micro-CT detects the solid portions of each surface, but in the core flooding experiments, the dissolved portions are of more interest. Therefore, using Drishti v2.4 again, a negative image was created in order to show the portions of the limestone that were dissolved. The negative image was created by changing the settings to display the solid portions of the core as vacant, and the vacant core sections to display a solid.

Micro-CT images of limestone pre- and post-flood samples with different flow conditions are shown in Figures 32-36. In preliminary testing, a limestone core was flooded with 1.41 ml/min of CO_2 and 1.0 ml/min of brine in order to match the flow rate of the sandstone experiment. However, this resulted in wormhole generation within the limestone core after about two days, ending the experiment. The Micro-CT results of the unreacted and reacted cores in Figure 36 show the wormhole generation in the first and third sections and an expansion of the pre-existing wormhole in the second section. It was determined that in order to prevent such a rapid development of a wormhole, the overall flow rate would need to be decreased. Thus, the flow rate of brine was reduced to 0 ml/min and 0.5 ml/min for brine, and 0.71 ml/min and 1.41 ml/min for CO_2.

It is observed that the pore morphology is practically unchanged for the experimental runs with only brine and with CO_2 only with the core initially saturated with

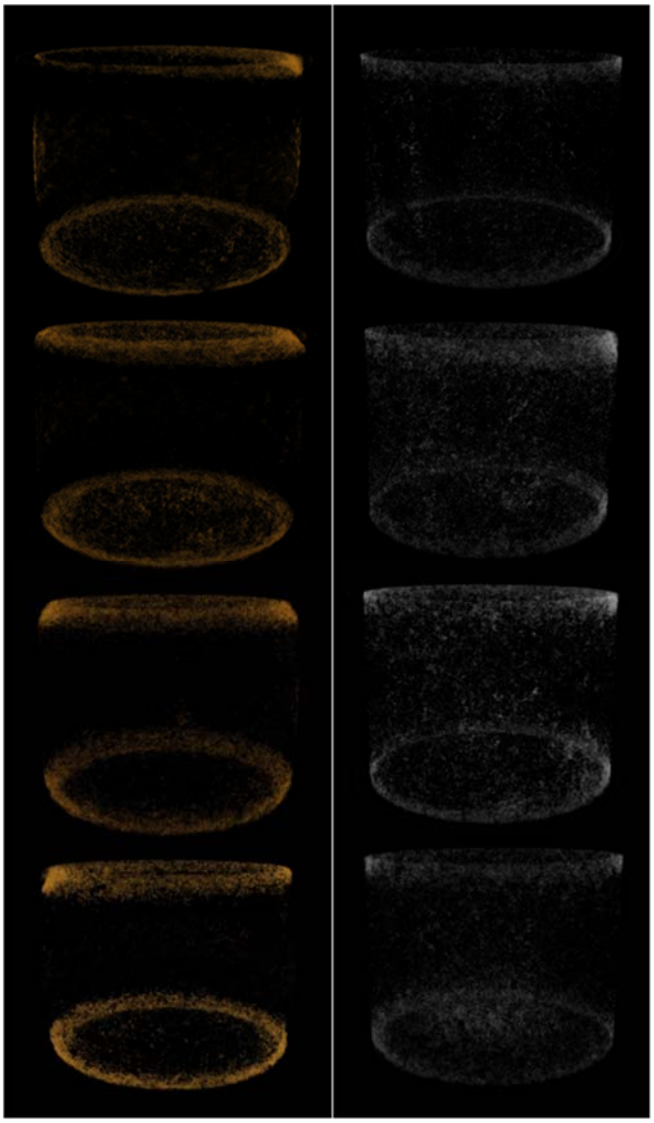

Figure 32. Images of different sections of limestone cores using Micro-CT pre- (left image) and post- (right image) flooding experiments with 0.5 ml/min brine only

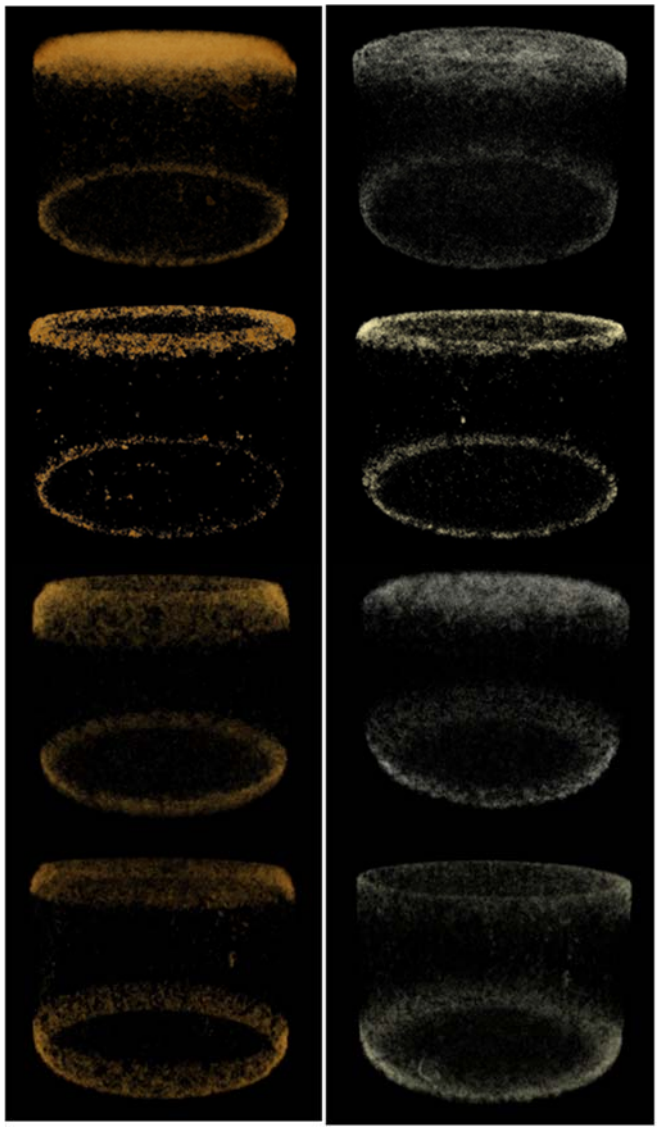

Figure 33. Images of different sections of limestone cores using Micro-CT pre- (left image) and post- (right image) flooding experiments with initially saturate brine + 0.71 ml/min CO_2

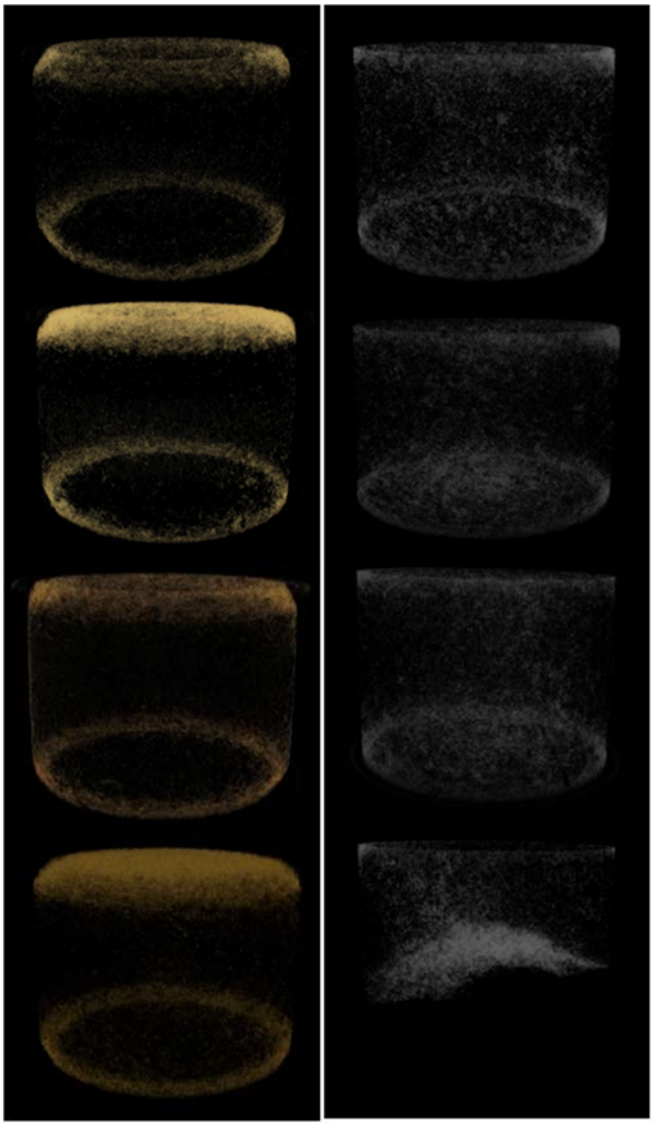

Figure 34. Images of different sections of limestone cores using Micro-CT pre- (left image) and post- (right image) flooding experiments with 0.5 ml/min brine + 0.71 ml/min CO_2

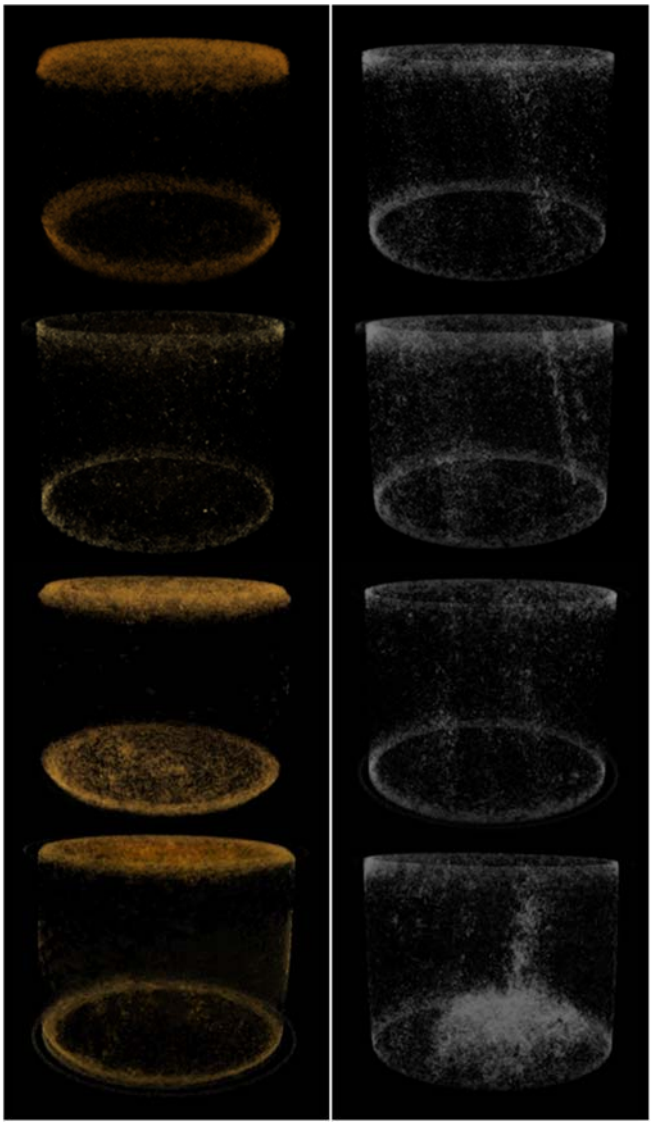

Figure 35. Images of different sections of limestone cores using Micro-CT pre- (left image) and post- (right image) flooding experiments with 0.5 ml/min brine + 1.41 CO_2

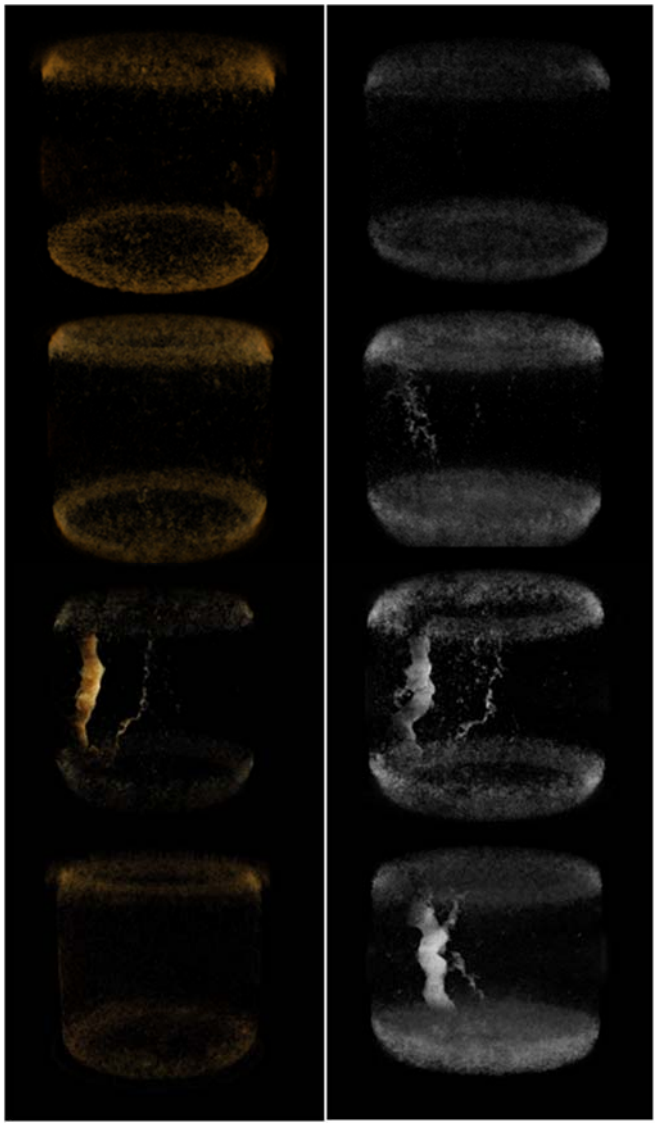

Figure 36. Images of different sections of limestone cores using Micro-CT pre- (left image) and post- (right image) flooding experiments with 1 ml/min brine + 1.41 CO_2

brine (Figure 32 and 33). Notice that the pore density is uniform throughout the core sections. Dissolution porosity is apparent in Figure 34 - the experiment conducted at low flow rates. Dissolution patterns and beginnings of the generation of wormhole type structures are evident for the experiment at the higher CO_2 flow rate (Figure 35). And finally, Figure 36 shows a fully developed wormhole. The existence of a small wormhole in the second core section obviously affected the growth of the wormhole in that section. Channeling of the CO_2-brine mixture through that section possibly resulted in the creation or acceleration of a wormhole in the first part of the core as well. The different flow rates show development in the dissolution of limestone. A low CO_2 flow rate demonstrated complete dissolution at the inlet, a high CO_2 flow rate demonstrated moderate dissolution at the inlet and a developing wormhole-like structure, and high CO_2 and brine flow rates demonstrated only a wormhole structure.

In analyzing the Micro-CT images, it can be seen that there is a general trend of increasing porosity between unreacted and reacted cores. The qualitative results of the Micro-CT are also consistent with the quantitative results of the helium porosimeter. Both Micro-CT results and helium porosimeter results show that the porosity is the greatest at the inlet and decreases as the distance from the inlet increases.

5.4 Summary

During core flooding experiments, petrophysical changes were also prominent, such as changes in porosity and permeability. Changes in porosity and permeability were quantified using a helium porosimeter. In sandstone, limestone, and dolomite, the porosity change ranged from 0.12 % to 1.01 %, from 0.55 % to 2.79 %, and from 0.42 %

to 2.52 %, respectively. Overall, higher flow rates increased the average porosity and porosity changes were greater at the inlet than at the outlet of each core sample. Permeability was calculated using Darcy's Law. In sandstone, permeability increased from 0.21 % to 1.43 %. Also, limestone and dolomite showed increases, from 1.06 % to 3.42 % and from 0.51 % to 2.41 %, respectively. Permeability increases were found in all core samples and showed a similar trend as porosity. Pore morphology changes were found particularly in limestone using Micro-CT. At lower flow rates, beginnings of wormhole type structures were observed, and at higher flow rates, fully developed wormholes were shown. The inlet of the dolomite cores displayed high dissolution phenomena as was also detected in the limestone core samples. The results of petrophysical changes observations were corroborated with measurements of concentrations of key cations in the effluent.

CHAPTER 6

SIMULATION STUDIES FOR CO_2 INJECTION PROCESS

6.1 Introduction

Numerous investigators have identified and assessed the impact of geochemical long-term reactions on storage reservoir performance and leakage risk through experiment and modeling.[145-150] High dissolved minerals have been noted in the field and in core flooding experiments. The modeling effort in this study accompanies the experimental work on sandstone. In this study, Numerical modeling of reactive transport near wellbore validated by the sandstone core flooding experiments at a brine flow rate of 1 ml/min and CO_2 flow rate of 1.41 ml/min described in detail in Chapter 3. In order to evaluate the experimental result, a simulation study is desired. Also, there are still a few remaining questions even though most experiments are well conducted. The questions to answer are:

(1) Which minerals are the primary sources for the high dissolved iron output?

(2)What interactions do they have during the kinetic dissolution and/or precipitation?

(3) How do porosity and permeability change as a result?

To answer these questions, the TOUGHREACT simulator has been employed. In the simulation model, equation of state module ECO2N is dedicated to CO_2-water-salt

mixture systems to model the processes in the system. Most of simulation conditions are match with core flooding experiment conditions.

TOGHREACT has several benefits, which are as follows:

- All the capabilities for simulating chemical reactions taking place between species are present both in the liquid and mineral phase
- Both dissolution and precipitation processes are integrated in this code with feedback on porosity and permeability changes
- Thermodynamic values for the density, viscosity, fugacity, and enthalpy of the CO_2 under supercritical conditions are calculated accurately
- An extensive geochemical thermodynamic database has been validated for a number of different applications

6.2 Core Flooding Experiment with Sandstone

The modeling effort in this study accompanies the experimental work on sandstone core samples. A brief description of the material and methods used in core flooding experiments is provided in detail, in section 3.2. The cores used are sandstone 7 inch in length and 1.5 inch in diameter. Sandstone has been widely used for tests of flow and transport in reservoirs throughout the world. The 7 inch length sandstone core sample is placed in the core holder that is under 3000 psi confining pressure and 2000 psi back regulating pressure at the outlet in an isothermal oven at 60 °C. The pressure and temperature used here represents a brine aquifer at the depth of approximately 3000 ft. core flooding system experiment conditions, which is consistent with some of the

potential CO_2 storage site selections.[151] Supercritical CO_2 and 2 wt. % NaCl brine are pumped continuously to the mixing chamber, and then injected uniformly into the core that is pre-saturated with the brine. The flow rates of CO_2 and brine are 1.41 ml/min and 1 ml/min, respectively. The pH of the mixed solutions was estimated to be 3.1 using published data on pH values of CO_2-brine mixtures at pressures and temperatures of our system.[152, 153] Porosity was measured by helium porosimeter. The porosity of sandstone used is 21.234 %. Effluent samples are collected at increasingly larger time intervals and chemically analyzed using ICP-MS for major cations. Initial mineral composition was determined by XRD and QEMSCAN on part of the unreacted core. The identified mineralogy recalculated of the sandstone is listed in Table 3. Based on the mineralogical

Table 3.Mineralogical composition of the sandstone and the amounts introduced in the model

Minerals	Initial volume fraction (%)	Modeled minerals
Quartz	60.85	Quartz
K-fieldspar	4.28	K-fieldspar
Illite	4.49	Illite
Plagioclase	2.16	Oligoclase
Kaolinite	2.34	Kaolinite
Chlorite	0.65	Chlorite
Smectite	0.54	Smectite-na
Ankerite	0.09	Ankerite
Muscovite	0.16	Not modeled
Micrite	0.13	Not modeled
Glauconite	0.10	Not modeled
Siderite	0.06	Siderite
Biotite	0.06	Not modeled
Rutile	0.05	Not modeled
Pores	21.0	Porosity
Total	96.5	-

composition as derived from the laboratory measurements, the ones that are of significant amount and of interest to this study are selected as well as can be accommodated by the simulator and introduced them into the geochemical model (also shown be accommodated by the simulator and introduced them into the geochemical model (also shown in Table 3). Since QEMSCAN produced more quantitative and comprehensive mineral composition, the average values of seven unreacted core slice measurements are used as the final volume fraction input.

6.3 Modeling Approach

In the TOUGHREACT simulator, flow transport and reactions are solved sequentially. In flow process, since there is excessive CO_2 in the inflow mixture, there will be two phases of an aqueous phase and a gas phase that models the supercritical CO_2. Figure 37 shows the core flooding concept image used in the TOUGHREACT simulator. As the injected fluids are distributed uniformly across the bottom of the core and material properties of the core are uniform, it is modeled as one-dimensional flow in a homogeneous medium. Along the z-direction, the model domain is a uniform structured grid of 60 cells divided over the 7 inch core. The flow at the bottom boundary is at constant mass flow rate for all three components: 1.65×10^{-5} kg/s for water, 1.65×10^{-5} kg/s for CO_2, and 3.33×10^{-7} kg/s for NaCl; and the top outlet is at constant pressure of 2000 psi. Flow process reaches steady state relatively fast, thus the time step controls are determined by the chemical processes. The time step size starts at 18 seconds and is allowed to increase to a maximum of 1800 seconds. Due to excessive supercritical CO_2, a two-phase flow model is needed. Van Genuchten-Mualem model is used for relative

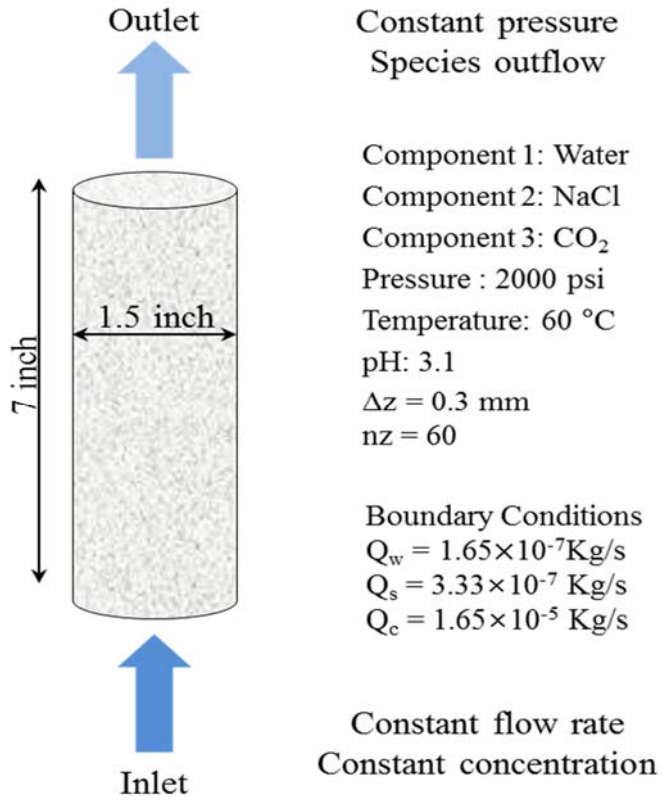

Figure 37. Core flooding concept image used in the TOUGHREACT simulator. Along with boundary conditions, core dimensions, and effluent properties

permeability calculations between CO_2 and brine, and Van Genuchten capillary pressure function is chosen.[154]

The chemical reactions induced by CO_2 injection are described in general. First, CO_2 dissolves in water to produce the weak carbonic acid. The dissolved bicarbonate species react with divalent cations to precipitate carbonate minerals. Formation of calcium, magnesium, and iron(II) carbonates are expected to be the primary means by which CO_2 is immobilized. For this system, 12 primary species were selected to simulate the transport and reactions that are solved following the primary species solution method. The mineral reactions in terms of primary species are listed in the stoichiometric matrix form in Table 4.

Table 4. Stoichiometric matrix for mineral reactions

	H_2O	H^+	Ca^{2+}	Mg^{2+}	Na^+	K^+	Fe^{2+}	SiO_2	HCO_3^-	AlO_2^-	Cl^-
Quartz	0	0	0	0	0	0	0	1	0	0	0
K-fieldspar	0	0	0	0	0	1	0	3	0	1	0
Illite	0.4	1.2	0	0.25	0	0.6	0	3.5	0	2.3	0
Kaolinite	1	2	0	0	0	0	0	2	0	2	0
Plagioclase	0	0	1	0	4	0	0	14	0	6	0
Smectite	0.52	0.96	0	0.26	0.29	0	0	3.97	0	1.77	0
Chlorite	8	-8	0	2.5	0	0	2.5	3	0	2	0
Siderite	0	-1	0	0	0	0	1	0	1	0	0
Ankerite	0	-2	1	0.3	0	0	0.7	0	2	0	0

All mineral dissolution and precipitation are considered to be kinetically controlled. A general form of rate law is used[155], equation (7):

$$r_n = k_n A_n \left(1 - {\Omega_n}^{\theta}\right)^{\eta} n = 1, \dots, N_q \tag{7}$$

where positive values of r_n indicate dissolution and negative values precipitation, k_n is the rate constant which is temperature dependent, A_n is the specific reactive surface area, Ω_n is the kinetic mineral saturation ratio defined as $\Omega_n = K_m^{-1} \prod c_j^{\nu} \gamma_j^{\nu}$, the ion activity product divided by the equilibrium constant K_m, θ and η are exponents determined from experiments, usually taken equal to 1. Ion activity coefficients are estimated using the Debye-Huckel equation since our system is at relatively low ionic strength. The kinetic rate constant k_n in equation (7) only considers the best-studied mechanism in pure H_2O at neutral pH. Dissolution and precipitation of some modeled minerals are catalyzed by

H^+ (acid mechanism) and OH^- (base mechanism). As a more general form of the kinetic rate constant, equation (8), Table 5 lists the values of the kinetic

$$k = k_{25} exp\left[\frac{-E_a}{R}\left(\frac{1}{T} - \frac{1}{298.15}\right)\right] + {k_{25}}^{H} exp\left[\frac{-{E_a}^{H}}{R}\left(\frac{1}{T} - \frac{1}{298.15}\right)\right] a_H^{n_H} + {k_{25}}^{OH} exp\left[\frac{-{E_a}^{OH}}{R}\left(\frac{1}{T} - \frac{1}{298.15}\right)\right] a_{OH}^{n_{OH}} \quad (8)$$

parameters used in the simulations. Note that the volume fraction values are referred to be the area fraction values QEMSCAN measures on a slice of the core for all of the inactive minerals. For active minerals of siderite and ankerite, volume fractions are calibrated. The volume fractions of the selected minerals and pore space sums up to be 96.6% of the volume. Specific reactive surface areas are assigned representative values for two mineral groups: clay minerals and non-clay minerals. Clay minerals have a higher surface area and non-clay minerals a lower surface area. Reaction rate constants at 25 °C for the selected minerals are taken from literature.[156] The kinetic rate constant for siderite was slightly adjusted to fit the effluent iron concentration. The set of values used to produce the best matches to the experimental data are presented.

Porosity changes in matrix are the results of volume changes due to mineral precipitation and dissolution. Using the option of Carman-Kozeny porosity-permeability relationship, changes in permeability are computed, equation (9):

$$kp/kp_i = (1 - \phi_i)^2/(1 - \phi)^2 \cdot (\phi/\phi_i)^3 \quad (9)$$

Table 5. Specific reactive surface areas and kinetic rate constants of minerals at 25 °C

	Reactive surface area (cm^2/g)	k^{nu} (mol/m^2s)	k^{H} (mol/m^2s)	k^{OH} (mol/m^2s)
Quartz	9.8	1.02×10^{-14}		
K-fieldspar	9.8	3.89×10^{-13}		
Illite	151.6	1.66×10^{-13}	1.05×10^{-11}	3.02×10^{-17}
Kaolinite	151.6	6.92×10^{-14}	4.90×10^{-12}	8.91×10^{-18}
Plagioclase	9.8	1.45×10^{-13}	2.14×10^{-11}	
Smectite	151.6	1.66×10^{-13}	1.05×10^{-11}	3.02×10^{-17}
Chlorite	9.8	3.02×10^{-13}	7.76×10^{-12}	
Siderite	9.8	1.26×10^{-08}	1.46×10^{-04}	
Ankerite	9.8	1.26×10^{-09}	6.46×10^{-04}	

where kp_i and ϕ_i are initial permeability and porosity, kp and ϕ are the final values.

6.4 Evaluation of Mineralogical Changes

Temporal evolution of major metal cation concentration in effluent has been used to calibrate the kinetic parameters in the model. In contrast to what was previously hypothesized, illite is not the main source of iron, from the two iron sources of siderite and ankerite identified in this model.

In Figures 38-41, four major elements are compared with the simulation result; iron, calcium, magnesium, and potassium, respectively. The line with the circles is the experimental ICP-MS data, and the line with the upside-down triangles is the simulation

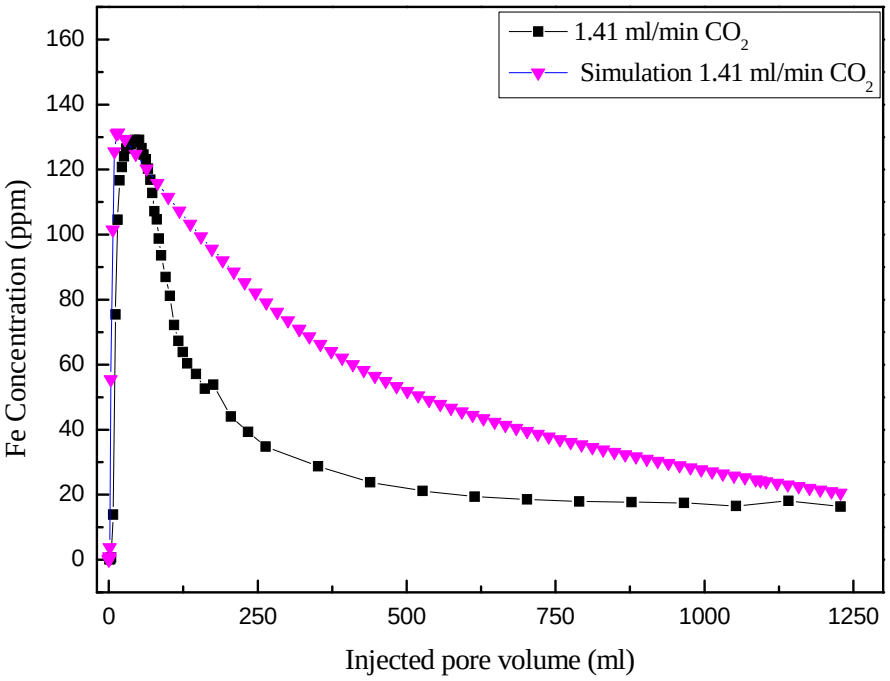

Figure 38.Comparison between simulation and experimental results for iron concentration change with injected pore volume at outlet

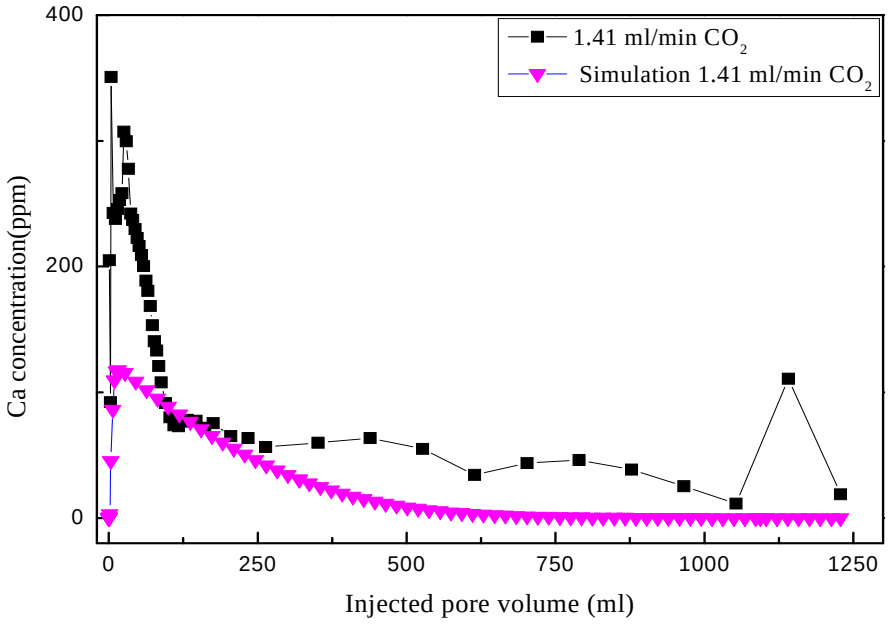

Figure 39.Comparison between simulation and experimental results for calcium concentration change with injected pore volume at outlet

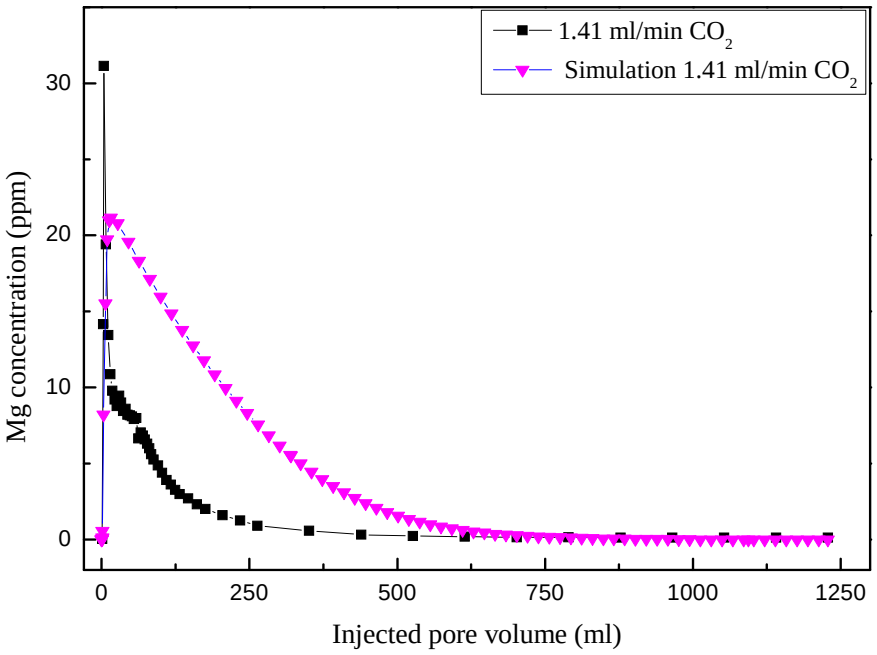

Figure 40. Comparison between simulation and experimental results for magnesium concentration change with injected pore volume at outlet

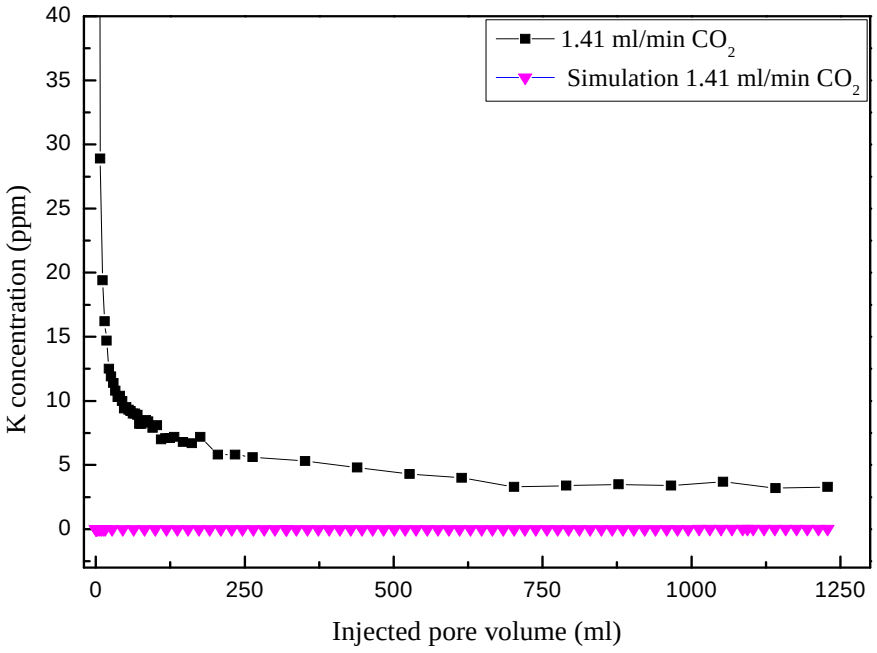

Figure 41. Comparison between simulation and experimental results for potassium concentration change with injected pore volume at outlet

data. The peak experimental value was used to calibrate the total mineral content and the tail calibrates the dissolution rate. The model is able to capture the general trend of a rapid increase to the peak value within the same injection pore volume values and then a more gradual decrease.

The total iron concentration with the injected pore volume was obtained at the outlet as shown in the Figure 38. Both simulation and experiment demonstrate the same trend, quickly increases to critical point and then gently stabilize. The critical value is around 130 ppm for both the simulation and the experiment. The experiment and simulation both show decreasing tails; the sudden increase is caused by the rapid dissolution of ankerite and the decreasing tail is due to the steady dissolution of siderite. The trend matches the QEMSCAN data that show siderite dissolution and complete ankerite dissolution.

Ankerite dissolution also produces calcium (Figure 39). The experimental values and simulation values are not well matched, but they show similar trends. Where they increase rapidly to the critical point, 360 ppm for experimental and 110 ppm for Ankerite dissolution also generates magnesium. A similar trend in magnesium concentration evolution is predicted. The maximum values are around 22 and 31 ppm in simulation and experiment, respectively. The general trend is captured well as a drastic increase followed by a drop to a steady value by the model as shown in Figure 40.

Illite dissolution produces potassium. The amounts of potassium containing minerals is very low and were not considered in the model, but were present in the experimental data (Figure 41). Therefore, in the experimental data initially, potassium concentration is around 40 ppm, and decreases to a low concentration, around 5 ppm.

The discrepancy in the iron, calcium, magnesium, and potassium concentrations between simulation and experiment results could imply that there are absent physical processes in the model, such as the incongruent dissolution of minerals in which one mineral transforms into a new mineral without releasing iron or magnesium into the solution. Also, the reaction rate was taken and may not have been completely accurate with the core flooding experiment. Another discrepancy could be the model is based on the mineral concentrations from QEMSCAN data. QEMSCAN uses area concentrations and the model uses volume fractions. A conversion was required to change from QEMSCAN area concentration to volume fraction for simulation model.

6.5 Porosity and Permeability Changes

As a result of mineral dissolution, porosity and permeability increases throughout the core. Porosity and permeability changes were calculated according to Darcy's Law. Due to the mineral kinetic rate distribution, more significant changes take place towards the inlet than towards the outlet. Maximum amount is predicted to be 0.5 % and 1.4 % for porosity and permeability, respectively. Figure 42 and 43 show the comparison between pre-experiment and post-experiment values of porosity and permeability distribution in the core (left to right is core inlet to outlet), respectively. The helium porosimeter data show that the overall porosity of the core is increased, as shown by the simulation. However, the individual core sections based on the helium porosimeter result have different porosity increases. A possible explanation is that a more complex relationship between mineral dissolution/precipitation and reaction affinity than what equation (7) proposes. Additional models may be needed such as the combined surface complication

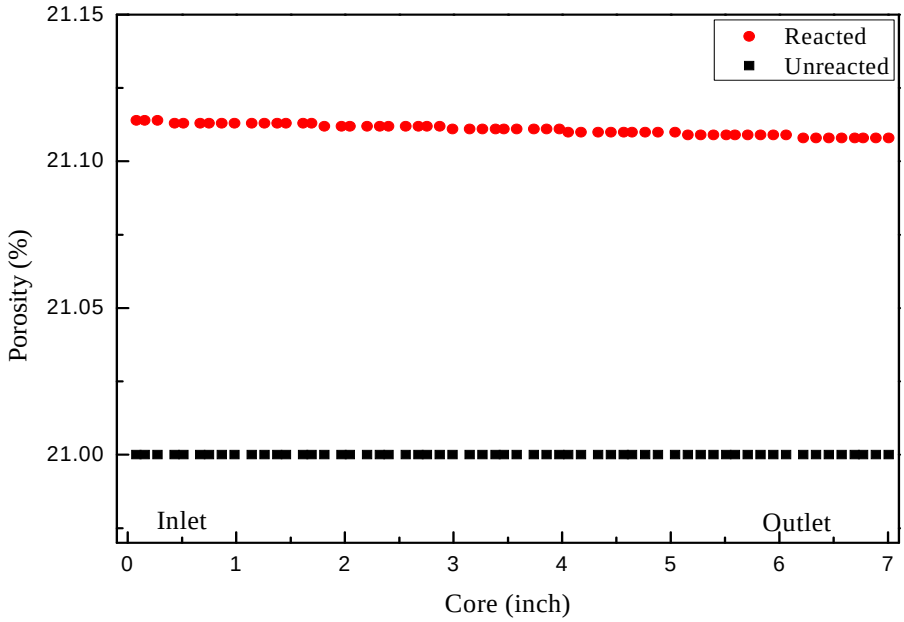

Figure 42. Predicted porosity changes along the core for initial and final values

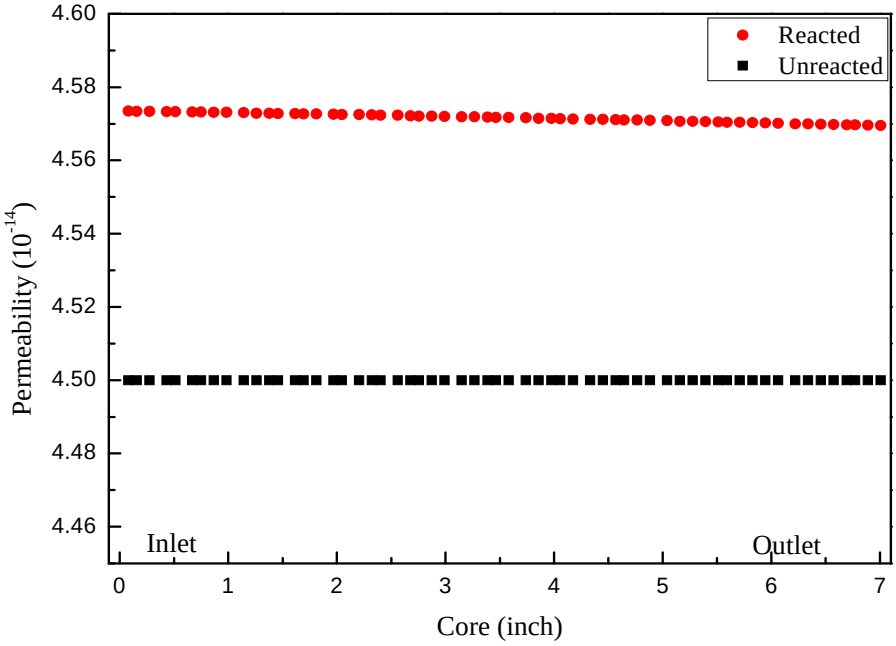

Figure 43. Predicted permeability changes along the core for initial and final values

model and transient state theory proposed by Schott et al. to fully capture the reactions that are indeed taking place on the surfaces.[157] The other consideration is that the heterogeneity was not incorporated in the model.

Although absolute changes in porosity and permeability are not significant, taking the very short time frame into consideration it will be significant long term. Both changes are underestimated in model, which may be caused by homogeneity assumption and indicate that the precipitation process is more complex than what equation (7) proposes.

6.6 Mineralogy Alteration in the Core

Both siderite and ankerite are completely dissolved at the end of the two-week period. Dissolution of the two source minerals takes place at different rates along the core, faster at inlet and slower towards outlet as pH increases from inlet to outlet. For both minerals, the volume fraction line for the near inlet location sits on top of that for the near outlet location throughout the simulation period. Figure 44 and Figure 45 show ankerite and siderite concentrations along the sandstone core at various times. These minerals are believed to be the main source of iron in the sandstone cores. Recall the ICP-MS result for iron concentration; notice in Figure 44 how the ankerite concentration rapidly decreases over time; at 87 hours it is nearly nonexistent and at 300 hours the ankerite is completely dissolved. The rapid dissolution of ankerite causes the iron and also the magnesium concentration peaks in the simulation and ICP-MS data (Figure 14 and Figure 15). Now looking at the siderite concentration, Figure 45, notice the gradual siderite concentration decrease over time. The siderite dissolution rate is much slower

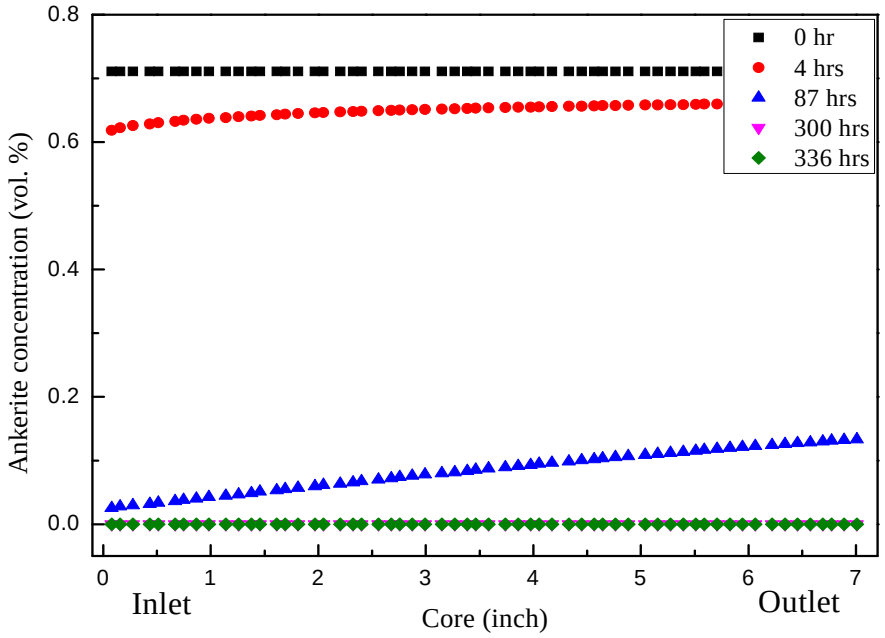

Figure 44. Simulation results of ankerite concentration change with time at different locations in the sandstone core

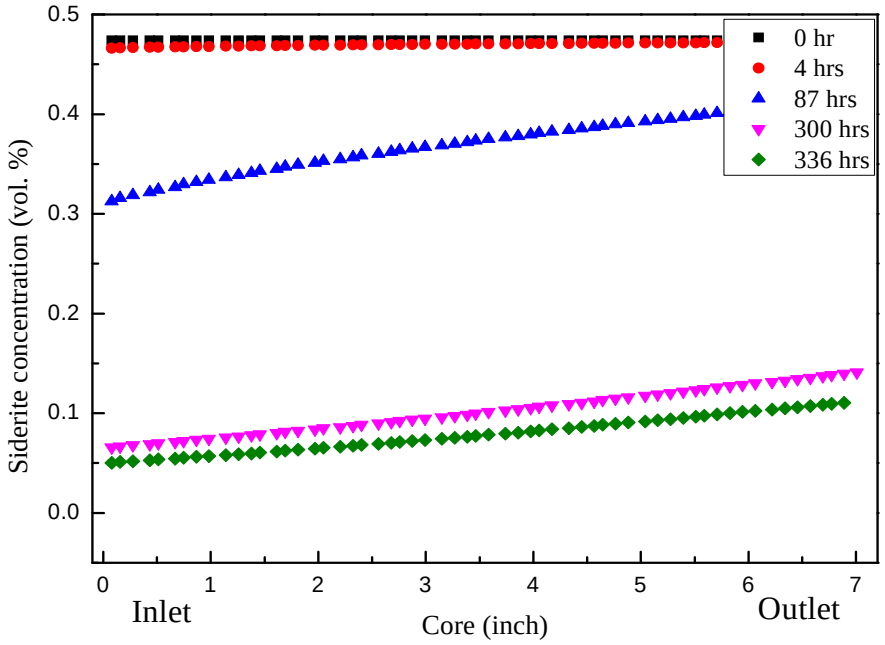

Figure 45. Simulation results of siderite concentration change with time

at different locations in the sandstone core than that of ankerite. This slower siderite dissolution rate causes the consistent release of iron into the effluent. This consistent dissolution is believed to correspond to the gradual decreasing tail in iron concentration in the simulation and the ICP-MS data (Figure 14).

Other iron source minerals are smectite and chlorite. These minerals have very slow dissolution rates according to the QEMSCAN result, Figure 9. Smectite and chlorite concentrations are essentially constant over the two-week period. At the end of two weeks, there is evidence that these minerals begin to dissolve based on the simulation model.

6.7 Summary

TOUGHREACT simulator closely evaluated the results of the core flooding experiments over a two-week simulation period. Trends and peaks of effluent cation concentrations (particularly, iron) were matched by the simulations. Simulations showed that ankerite dissolution was fast relative to siderite leading to the characteristic iron effluent profile observed in the core flooding experiments. The fast dissolution of ankerite caused the steep peak in iron concentration and slow dissolution of siderite lead to the gradually decreasing tail in the profile. Calcium and magnesium showed a similar elemental concentration and dissolution trend as in the core flooding experiments. Potassium concentration was not present in the simulation because the reaction rate of potassium containing minerals was lower than expected. Porosity and permeability changes predicted in the simulation were reasonably close to the experimental values. The porosity change under this flow rate condition was 0.6 % from experiment, and the

simulation found the porosity change to be 1.0 %. As for permeability, experimentally the change was 0.76 % and from the simulation it was 1.02 %.

CHAPTER 7

MINERALOGICAL CHANGES IN BATCH REACTOR SYSTEM

7.1 Reaction Pressure

The initial batch reactor pressures were determined to be around 830-840 psi. After the reactors were filled with CO_2, the batch reactors were placed in the oven at 60 ˚C. Upon being inserted into the oven, the pressure of the reactors gradually rises until reaching target pressure around 2400 psi. The batch reactor experiments were successively completed for a two-week period. The pressure was recorded throughout the two-week period in order to detect drastic changes in pressure. If the pressure of any one reactor fell below the 2000 psi mark, it would then be removed from the oven, cooled to room temperature, refilled with CO_2, and reinserted into the oven.

Table 6 shows the pressure of each batch reactor on each day of the experiment. Notice the gradual decrease in pressure over the initial couple of days. This pressure drop is likely due to the CO_2 being dissolved in the brine and reaching equilibrium. After the first few days, the pressure continued to slowly decrease; this pressure drop is due to the mineralogical reactions with carbonate taking place. When the pressure leakage happened very rarely, the reactor was refilled with CO_2 again. The target pressure was tried to match when the reactor was removed. Sometimes, the pressure was stable or increased compared with previous dates; possible discrepancies are the temperature fluctuation

Table 6. The reactor pressure profiles according to different sample types and forms

Core plug samples	Initial	1st	2nd	3rd	4th	5th	6th	7th	8th	9th	10th	11th	12th	13th	14th
Blank	842	2450	2400	2370	2350	2350	2350	2350	2350	2350	2300	2350	2350	2350	2350
Sandstone	830	2340	2320	2300	2300	2280	2280	2250	2250	2240	2240	2220	2200	2200	2200
Limestone	833	2350	2300	2300	2300	2280	2250	2250	2250	2200	2180	2150	2100	2080	2080
Dolomite	835	2400	2350	2350	2360	2320	2300	2300	2300	2300	2300	2300	2320	2300	2300
Fracture samples	Initial	1st	2nd	3rd	4th	5th	6th	7th	8th	9th	10th	11th	12th	13th	14th
Blank	840	2450	2400	2380	2360	2360	2360	2350	2350	2350	2300	2350	2350	2350	2350
Sandstone	834	2400	2350	2350	2300	2300	2300	2280	2250	2250	2240	2220	2200	2180	2150
Limestone	832	2350	2300	2300	2250	2250	2250	2250	2240	2240	2220	2220	2200	2200	2200
Dolomite	836	2400	2350	2350	2350	2330	2320	2320	2300	2300	2280	2280	2260	2260	2250
Powder samples	Initial	1st	2nd	3rd	4th	5th	6th	7th	8th	9th	10th	11th	12th	13th	14th
Blank	841	2450	2400	2380	2380	2360	2360	2360	2350	2350	2300	2350	2350	2350	2340
Sandstone	836	2420	2400	2350	2300	2280	2280	2250	2250	2240	2230	2200	2180	2160	2150
Limestone	832	2350	2300	2250	2250	2200	2200	2150	2140	2140	2120	2100	2100	2050	2050
Dolomite	831	2350	2300	2300	2280	2260	2250	2250	2220	2220	2200	2200	2280	2260	2250

within the oven (Figure 46), and the pressure gauges used are not digital and subject to reading error.

7.2 Mineralogy Changes: ICP-MS

Before studying effects of different surface area of core (different forms), mineral dissolution patterns were determined and plotted by cation concentration over time (Figures 47-50).

Iron (Figure 47) and magnesium (Figure 48) concentrations before 48 hours and after 48 hours show different dissolution rates; this is believed to be caused by the rapid dissolution of ankerite minerals. In the iron case, siderite mineral dissolution also affects the iron concentration profile by the slow dissolution rate, as in the core flooding

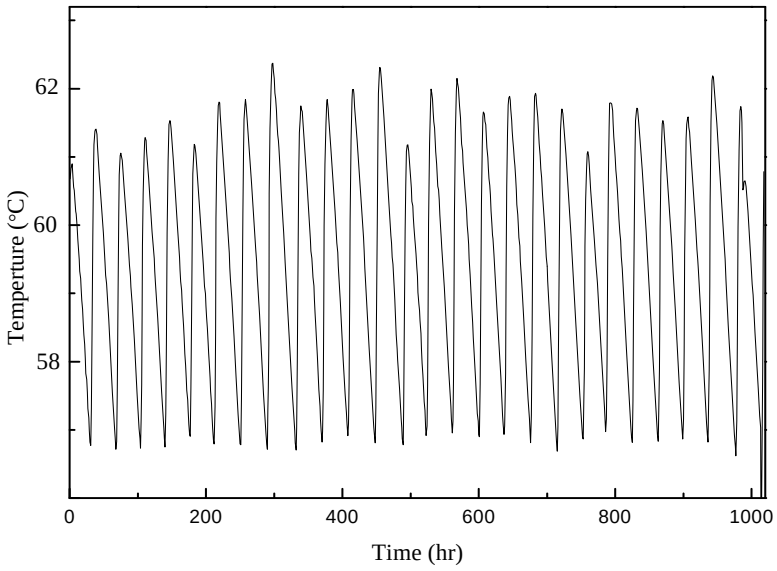

Figure 46. Oven temperature profile over the 1000 hours

experiments. The calcium concentration profile (Figure 49) is similar to that of iron and magnesium, but the profile change did not occur until 96 hours. The extended time of rapid dissolution is caused by simultaneous dissolution ankerite and calcite minerals. The slow concentration change after 96 hours is believed to be the dissolution of remaining calcium containing minerals. The potassium concentration profile (Figure 50) shows a completely different pattern. In these sandstone samples, illite is the only possible potassium containing mineral. As was also found in the core flooding experiments, the potassium ion concentration profile is also very different than the other elemental profiles.

7.3 Mineralogy Changes by Different Surface Area: ICP-MS

Upon completion of the experiment, each of the collected fluids was analyzed using ICP-MS. The data set is shown in Table 7. For most of the experiments, there was

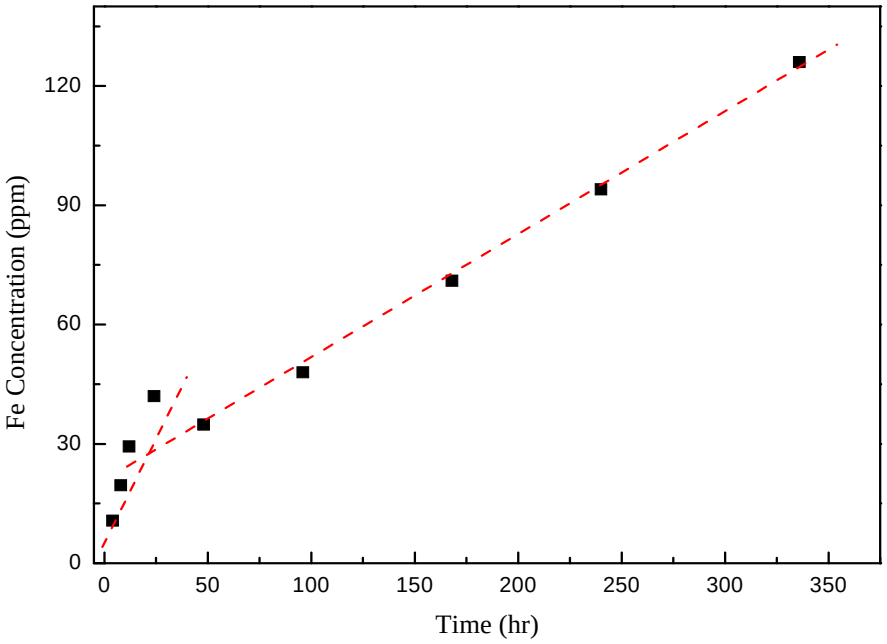

Figure 47. Concentration of iron ions as measured by ICP-MS in the effluent for sandstone time step batch experiments

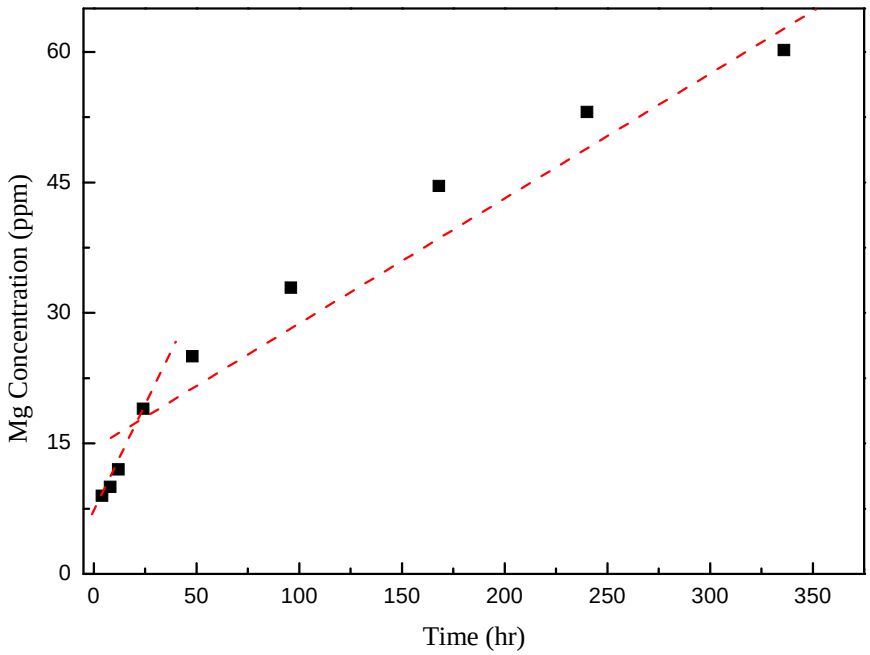

Figure 48. Concentration of magnesium ions as measured by ICP-MS in the effluent for sandstone time step batch experiments

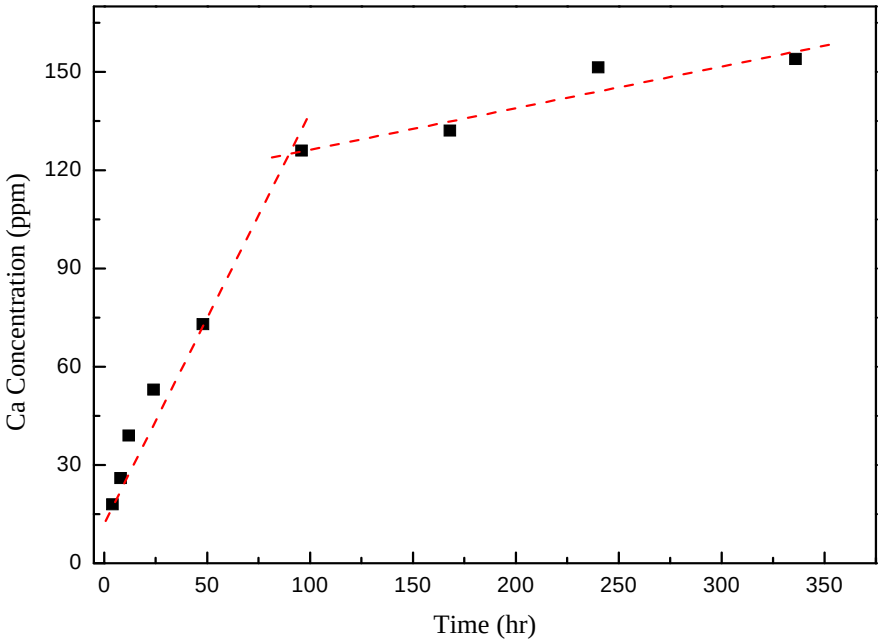

Figure 49. Concentration of calcium ions as measured by ICP-MS in the effluent for sandstone time step batch experiments

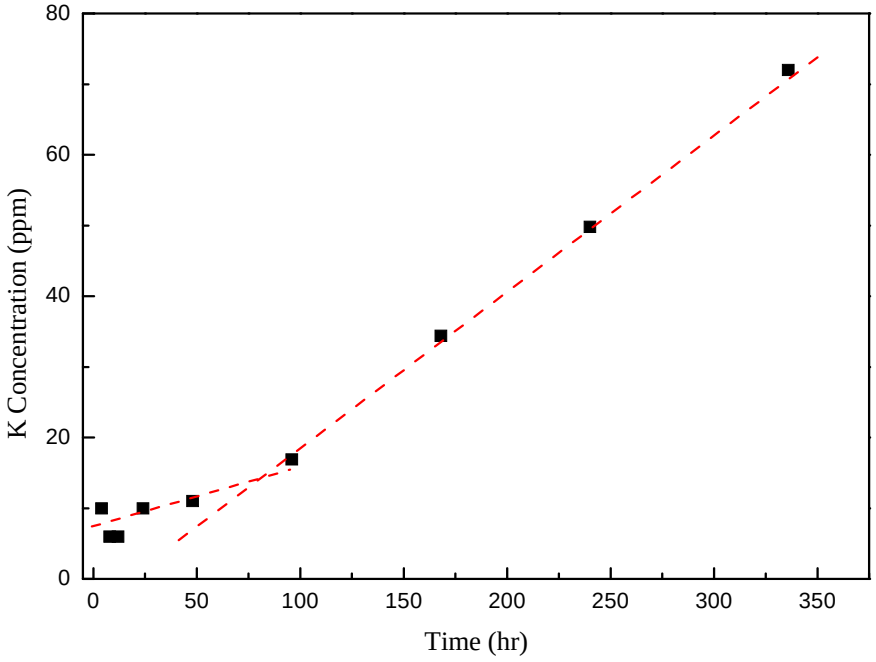

Figure 50. Concentration of potassium ions as measured by ICP-MS in the effluent for sandstone time step batch experiments

Table 7. ICP-MS results for core plug, fractured core, and powdered core after two-week batch experiment at 60 °C and over 2000 psi

	Na (mg/kg)	Mg (mg/kg)	Al (mg/kg)	Si (mg/kg)	K (mg/kg)	Ca (mg/kg)	Fe (mg/kg)
LoD	2	0.004	0.06	0.06	7	13	0.05
Core plug samples							
Blank	7024	0.68	0.64	0.22	<7	<13	1.92
Sandstone	7108	60.2	27.2	3.8	72	154	126
Limestone	7024	24	2.43	1.16	64	571	0.08
Dolomite	7188	302	0.87	5.04	80	428	0.08
Fracture samples							
Blank	7096	0.82	<0.06	0.25	<9	<13	1.14
Sandstone	7103	109	64.9	8.4	140	204	192.1
Limestone	7028	29	1.39	3.07	96	708	0.07
Dolomite	7097	444	0.15	2.37	137	543	0.08
Powder samples							
Blank	7018	0.74	0.32	1.68	<4	<13	1.53
Sandstone	6904	167.2	98.5	17.2	211	384	271.44
Limestone	7103	28.4	1.32	2.32	163	1226	0.07
Dolomite	7062	705	0.36	8.46	190	960	0.06

little change in the concentration of sodium from the relatively high values, because of the 2% NaCl brine. The concentrations of sodium in each sample were slightly different although the same concentration of brine was used. The error range is less than 5% which is acceptable for these experiments.

These results are likely related to operational error, such as dilution, and other contaminants. In the blank test, the concentrations of minerals such as magnesium, aluminum, and iron throughout the experiment were slightly over the ICP-MS detection

limit. This suggests some possible evidence for reactor corrosion. To minimize the reactor corrosion effect, the reactors were replaced after a couple experiments.

Based on Table 7, most of elements concentrations are increased, when surface area of the sample is increased matching the purposed hypothesis, which is that mineral reactivity is affected by surface area changes. Magnesium exhibits a trend of increasing concentration as the surface area of the sample is increased. This is especially true in the case of sandstone and dolomite, but the effect is less in that of limestone. Illite and ankerite dissolution would be the source of the magnesium concentration increase in sandstone; in dolomite, magnesium is one of the main elements in the dolomite mineral and the obvious cause of the magnesium concentration increase. In limestone, there are very few minor minerals containing magnesium. This magnesium concentration change is consistent with the core flooding experiment results.

Aluminum and silica did not display a significant change in concentration in the limestone and dolomite core forms (core plug, fractured, powder). In these two rocks, minerals containing aluminum and silica are present in small quantities and are primarily unreactive. In sandstone, there is a large concentration difference in aluminum concentration when compared with limestone and dolomite, especially in powder samples. Two possible sources of silica are quartz and illite. Quartz is unreactive with the CO_2 and brine solution; therefore, illite would be the primary source of silica in the effluent. Potassium similarly shows little changes by the different forms during the experiment. The concentrations are also relatively similar in each rock type (sandstone, limestone, and dolomite).

Calcium has the same trend, in that it tends to increase with surface area. Dolomite and limestone show the greatest changes. The main minerals found in limestone and dolomite are primarily made up of calcium. Sandstone shows relatively small changes in calcium concentration. The main reactive mineral containing calcium in sandstone is ankerite which is found at a low concentration. The concentration of iron in each of the reactors seems to be consistent with the concentrations of iron in the dolomite and limestone samples. However, iron concentration in sandstone is quite interesting. Each of the samples with sandstone results in large concentrations of iron, indicating dissolution of iron containing minerals. Based on the core flooding experimental results and simulation, these minerals are mainly ankerite and siderite. However, the dolomite and limestone samples show comparatively low amounts of iron concentration. The total mineralogical changes in the batch experiments are lower than those found in the core flooding experiments and simulation results. In the core flooding experiments, reactive fluid was continuous injected. However, in batch experiments, the rock samples were contained in the same fluid over the two-week period. The different fluid conditions caused different dissolved element concentrations.

7.4 Mineralogy Changes by Different Surface Area: XRD

XRD was used to detect mineralogical changes found in the unreacted and reacted different core and form samples. Even though the form of the rock was changed (core plug, fractured, powder), there was no significant change in the XRD results. This is because the XRD analysis is more of a bulk measurement, and does not accurately detect the small changes that accompany the difference in sample form. Therefore, a similar

approach was used in analyzing XRD data from the batch experiments as was used in the core flooding experiments. The quartz intensity in each sandstone form was determined before and after the experiment. The unreacted core is made up of around 86 % quartz. This value was compared with the value found for each of the various sandstone forms. Figure 51 shows the quartz intensities for unreacted, reacted core plug, reacted fractured core, and reacted powder. The quartz intensities of the reacted core plug, fractured core, and powder are around 88 %, 90 %, and 92 %, respectively.

XRD spectra (Figure 52 and Figure 53) of unreacted and reacted limestone and dolomite core samples were also taken. As in the core flooding experiment, the purity of limestone and dolomite cause the XRD spectra comparison to be inconclusive.

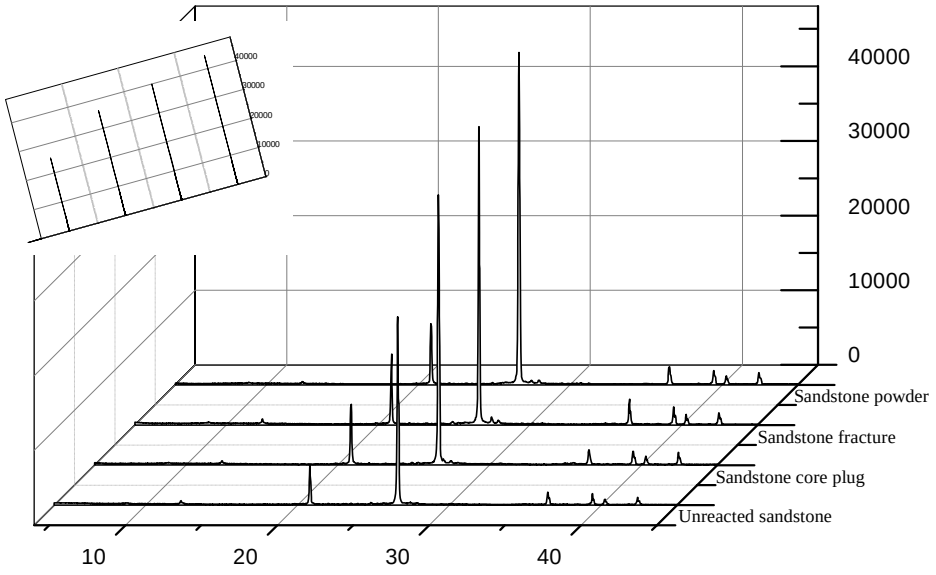

Figure 51. XRD Spectra lines of unreacted and various reacted sandstone core forms such as plug, fracture, and powder samples

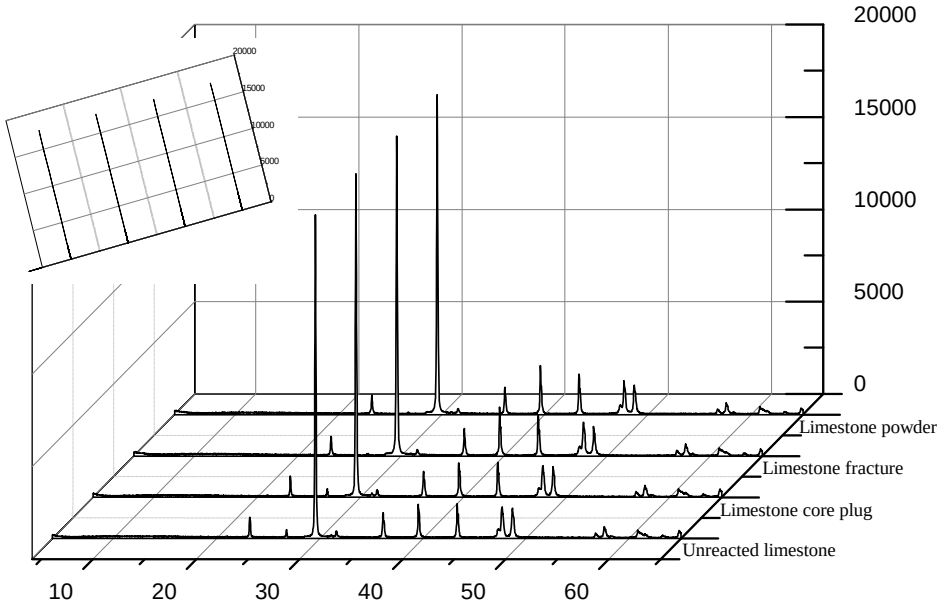

Figure 52. XRD Spectra lines of unreacted and various reacted limestone core forms such as plug, fracture, and powder samples

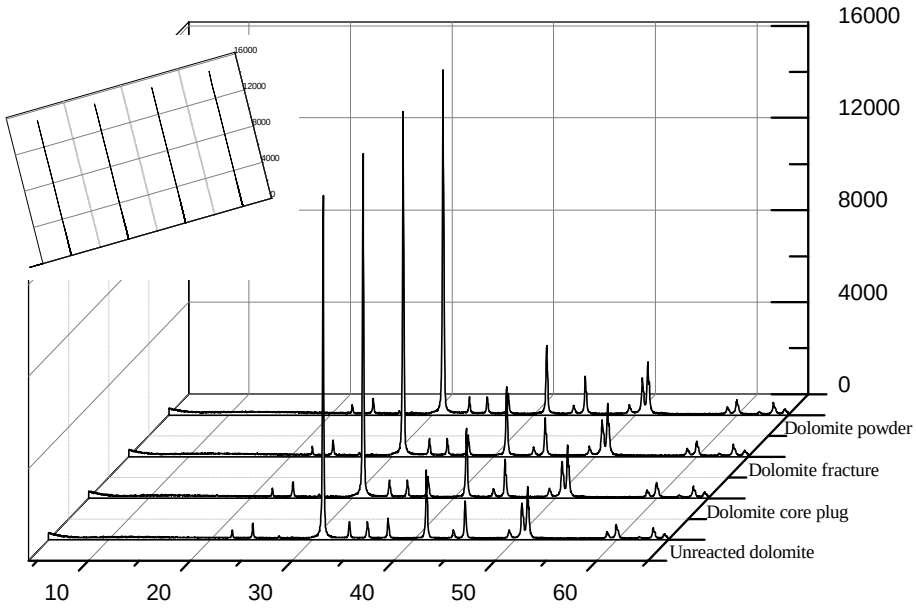

Figure 53. XRD Spectra lines of unreacted and various reacted dolomite core forms such as plug, fracture, and powder samples

7.5 Mineralogy Changes by Different Surface Area: QEMSCAN

QEMSCAN was used to obtain better understanding of mineralogical change in the batch experiments with different core plugs as was done for the core flooding experiments. The QEMSCAN images of unreacted and reacted different core plugs are presented in Figures 54-59. The QEMSCAN analysis confirmed that calcite, dolomite, and quartz were the dominant minerals in the rocks, with minor amounts of alkali feldspar, illite, plagioclase, kaolinite, and other lower amounts of various minerals.

Figure 54 shows the surface image and the mineralogical composition of the unreacted sandstone core plug. Quartz is the main mineral with a composition around 77.83 % by area. Illite is the second most dominant at 5.74 % by area. After the two-week batch experiment, Figure 55 shows the image and mineralogical composition of the reacted sandstone core plug. The two most dominant mineral compositions are compared, quartz concentration increased to 84.50 % by area, and illite concentration decreased to 3.84 % by area relatively. The reactive minerals like illite dissolved during the batch experiment causing unreactive mineral concentration such as quartz to increase, confirming the XRD observation. Also, the background surface area is increased meaning the porosity has increased.

Figure 56 shows the surface image and the mineralogical composition of the unreacted limestone core plug. Calcite is the main mineral with a composition around 99.08 % by area. After the two-week batch experiment, Figure 57 shows the image and mineralogical composition of the reacted limestone core plug. Calcite concentration did not changed significantly, less than 0.3 %; the reacted calcite concentration is 98.80 % by area. QEMSCAN uses mineralogical surface percentages based on relative amounts of

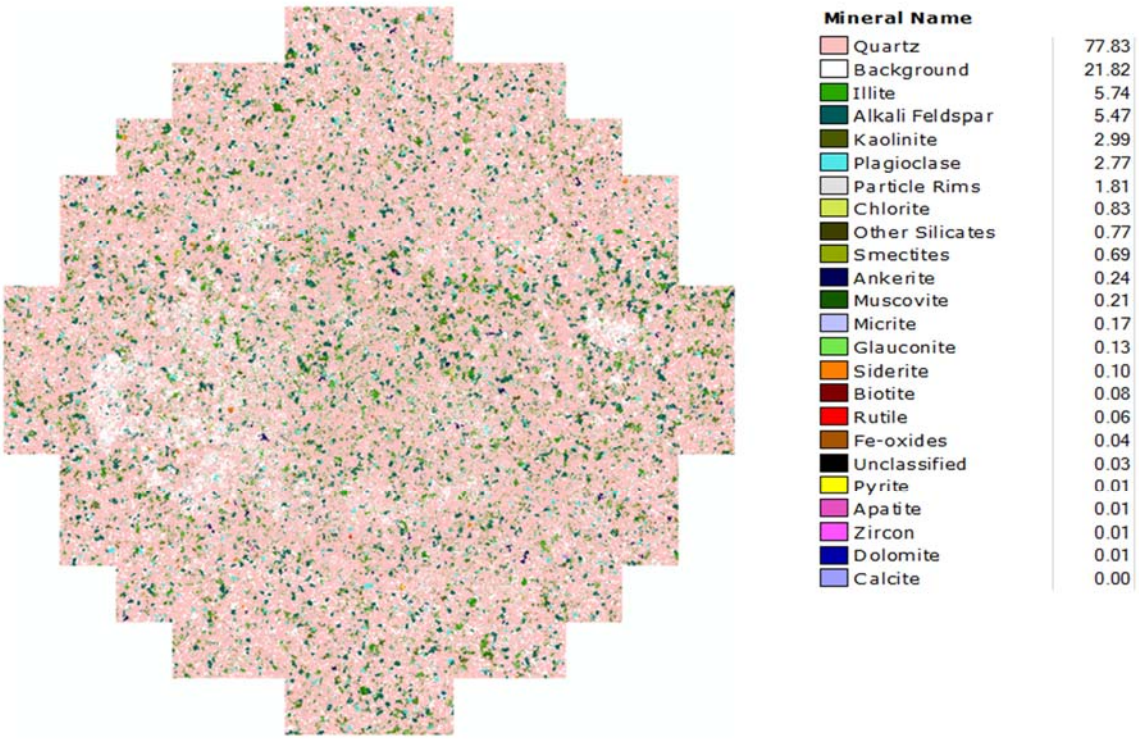

Figure 54. QEMSCAN result of unreacted sandstone core plug

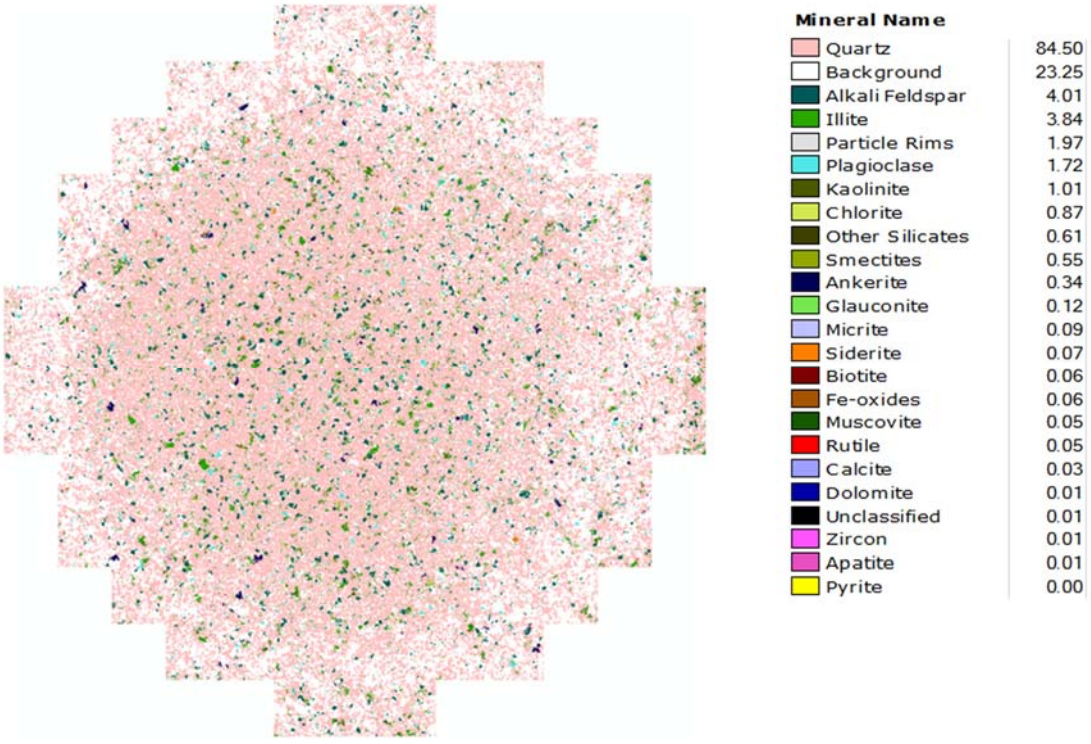

Figure 55. QEMSCAN result of reacted sandstone core plug

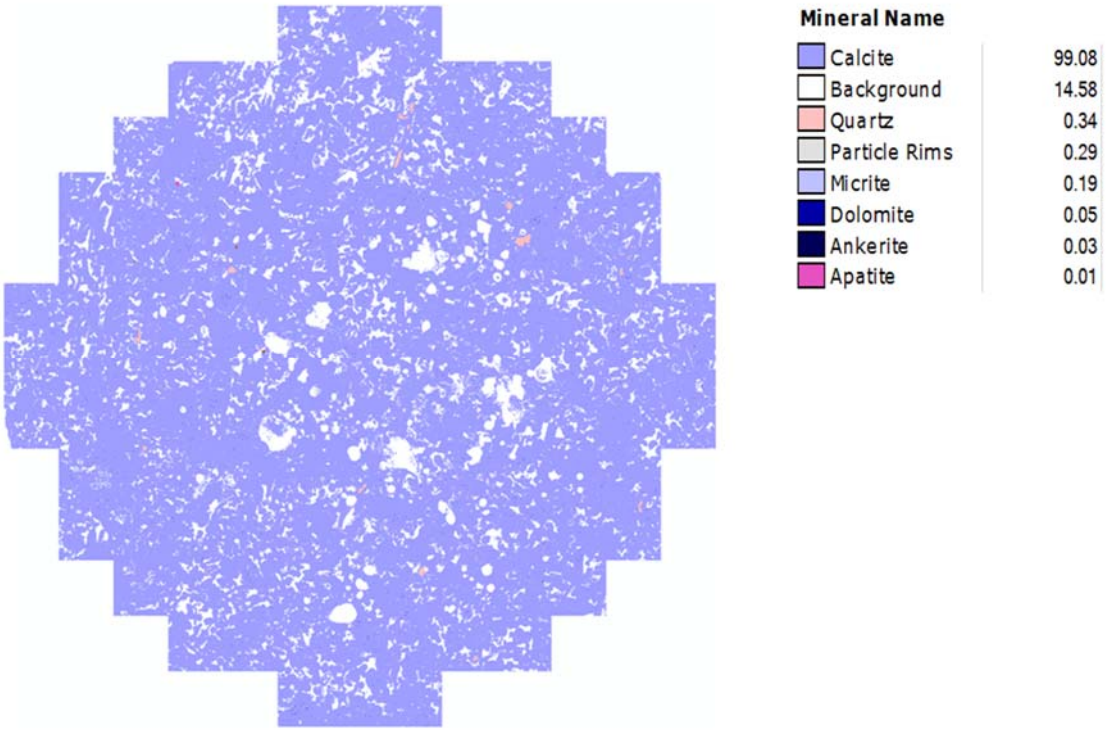

Figure 56. QEMSCAN result of unreacted limestone core plug

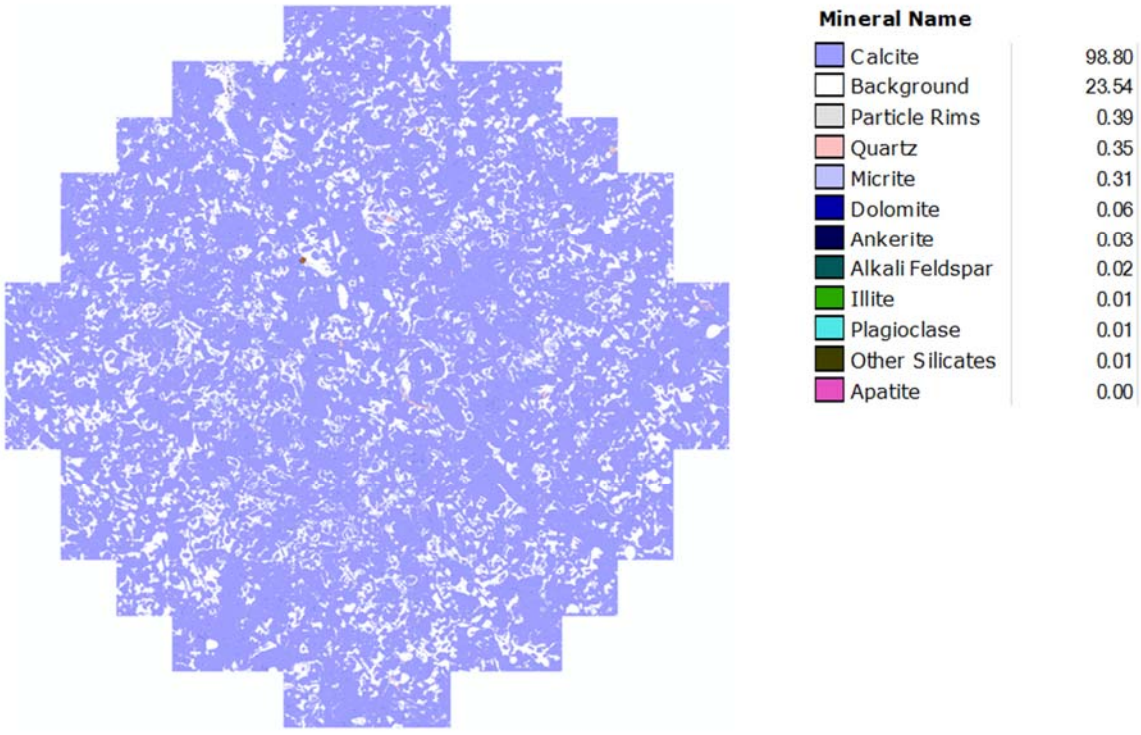

Figure 57. QEMSCAN result of reacted limestone core plug

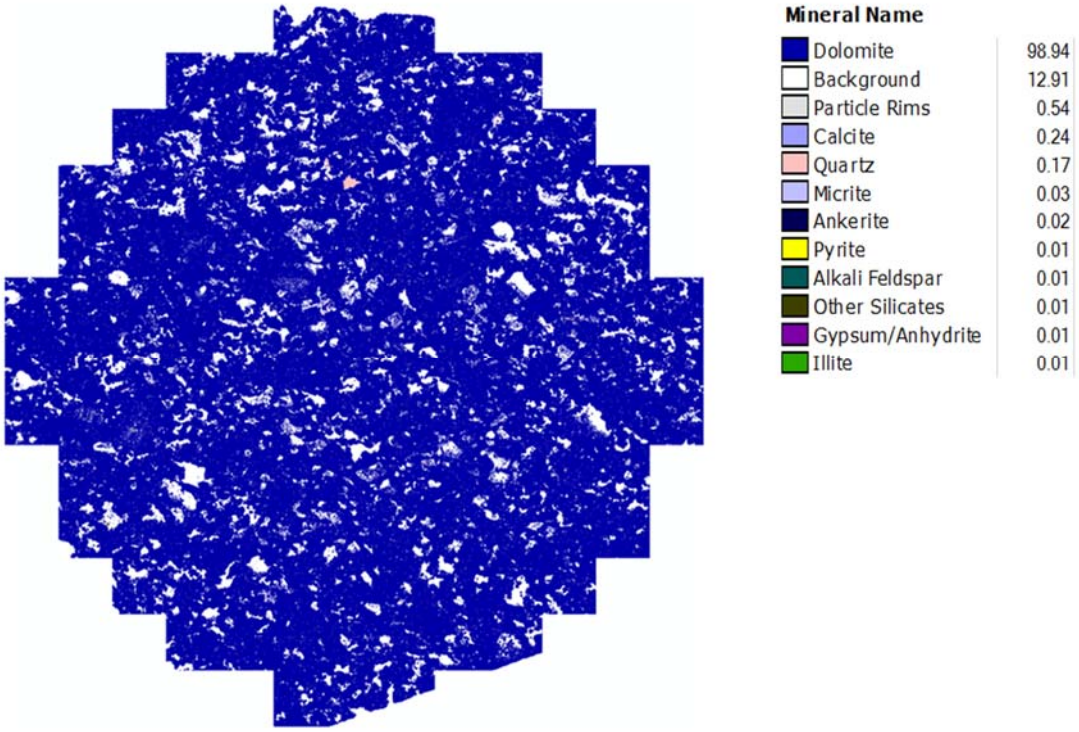

Figure 58. QEMSCAN result of unreacted dolomite core plug

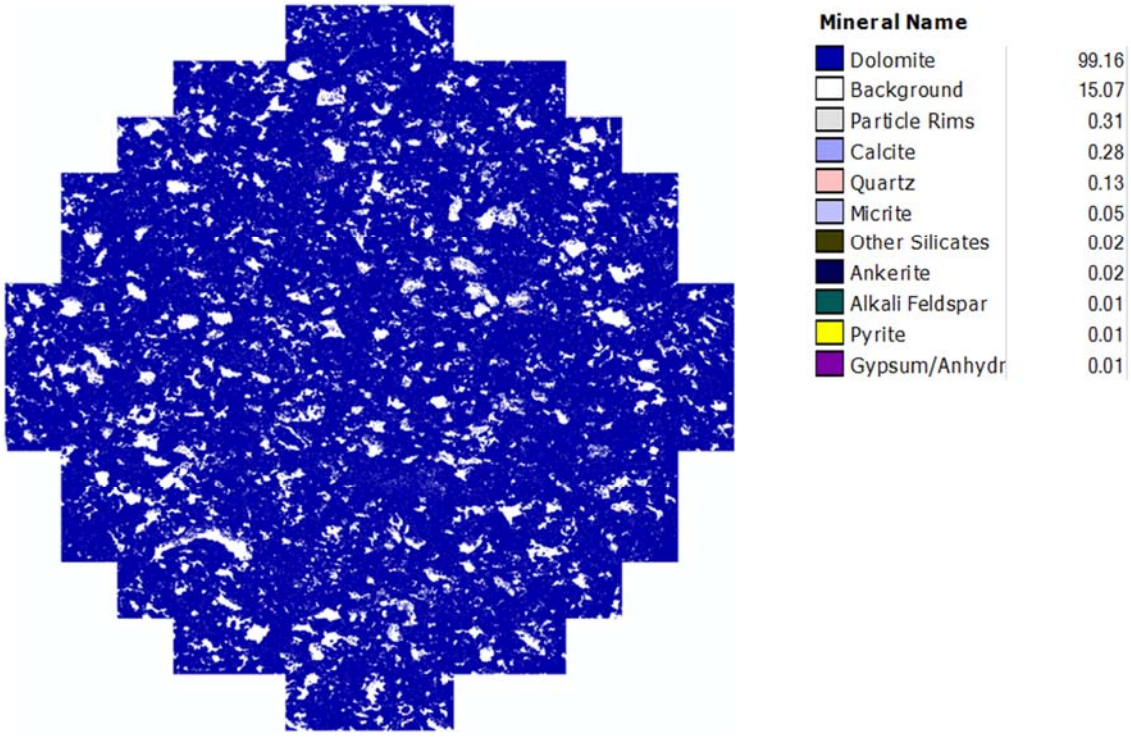

Figure 59. QEMSCAN result of reacted dolomite core plug

minerals on the sample. In the case of limestone, although, calcite is dissolved it still remains in high percent (nearly 100 %) relative to the other minerals, but the background area percentage has significantly increased from 14.58 % to 23.54 %. Based on the background area percentage increase, it concluded calcite has dissolved. Figure 58 and Figure 59 show the unreacted and reacted dolomite core plug, respectively. The result is very similar to the limestone result and the background area percentage change is what shows that dolomite has dissolved. The background area percent changed from 12.91 % to 15.07 %. When compared, limestone and dolomite surface area percentage limestone (Calcite) is more reacted with CO_2 and brine than dolomite.

Comparison of the XRD and QEMSCAN data indicates broad agreement between the two techniques because of differences in sampling location (i.e., the analyses are collected on adjacent rock surfaces but are still not exactly the same piece of material). In both QEMSCAN and XRD analysis, the mineralogical percentages are based on relative amounts of each mineral in the sample. This makes comparing absolute mineralogical amounts between samples and analytical methods difficult. In addition, the QEMSCAN percentages are based on a surface area, whereas, XRD represents volumetric mass fractions, and the analytical techniques are different.

The QEMSCAN images also show the pore surface area (background area) of the samples. This surface area is represented as the background in the images. Due to the 2D nature of the images, the pore surface area is approximated as the area of the blank regions of the sample image. These surface area approximations can be loosely compared with the surface area results from the BET analysis.

7.6 Mineralogy Changes by Different Brine Concentration: ICP-MS

The NaCl salinity level may vary from 0 to 36 wt. % depending on the geological conditions.[158, 159] In the present study, 2 wt.%, 5wt. %, and 10 wt. % NaCl concentrations were chosen to represent low and medium salinity environments. In order to better understand mineralogical changes at different salinity concentration, a batch reactor system was used. The effluents are analyzed by ICP-MS, and then results are compared. Figure 60 shows the iron concentration of the brine at different experimental conditions and brine concentrations. Iron concentration change is minimal at different brine concentrations, 125 ppm at 2 wt. % NaCl to 110 ppm at 10 wt. % NaCl. Figure 61 shows the calcium concentration distribution at different experiment conditions and brine concentrations. A similar result as found in iron is found for calcium. The calcium concentration is 150 ppm at 2 wt. % NaCl to 130 ppm at 10 wt. % NaCl.

The iron and calcium sources are likely ankerite based on the core flooding experiments and simulation; ankerite is dissolved more than the other iron containing minerals. Another calcium mineral source in sandstone is calcite. The amount is very small but it is very reactive and because of this, the total calcium concentration is higher than the total iron concentration. Figure 62 and Figure 63 show the magnesium and potassium concentration distribution at different experiment conditions and brine concentrations. A similar trend as found in iron and calcium is found for magnesium and potassium as well. The magnesium concentration is 60 ppm at 2 wt. % NaCl to 40 ppm at 10 wt. % NaCl, and the potassium concentration is 70 ppm at 2 wt. % to 30 ppm at 10 wt. %. Although the concentration difference for each element is slightly different at the different brine concentration, the difference is very small because the CO_2 solubility at

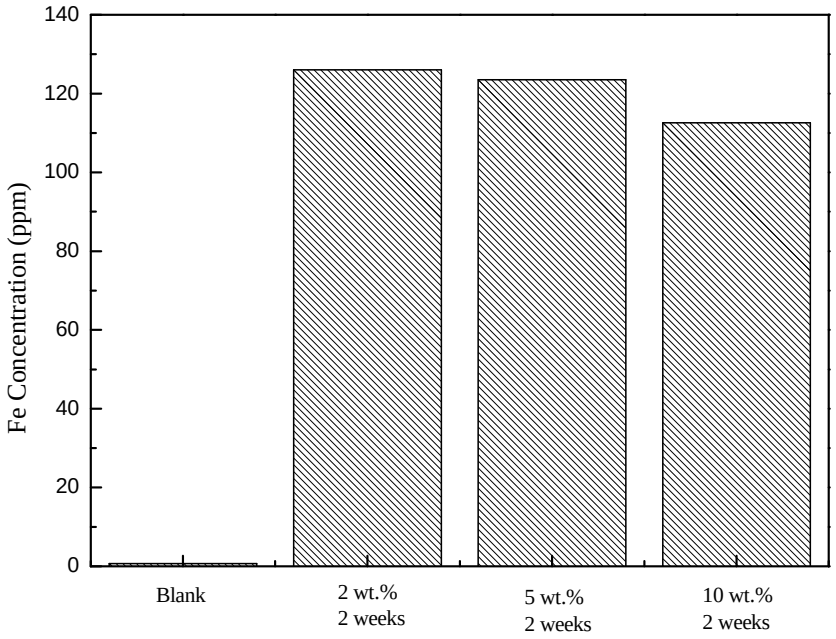

Figure 60. Iron concentration from ICP-MS after two week batch experiments with different brine concentrations

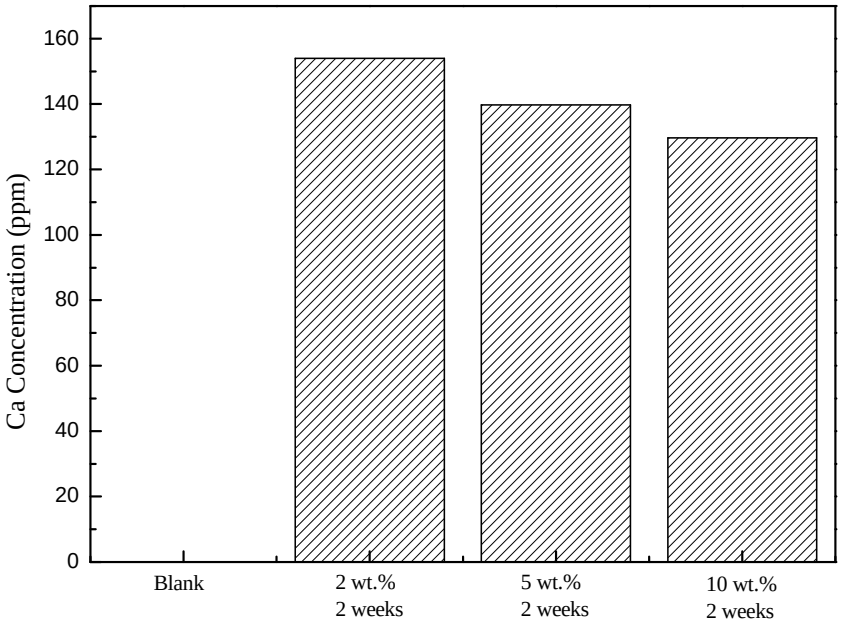

Figure 61. Calcium concentration from ICP-MS after two week batch experiments with different brine concentrations

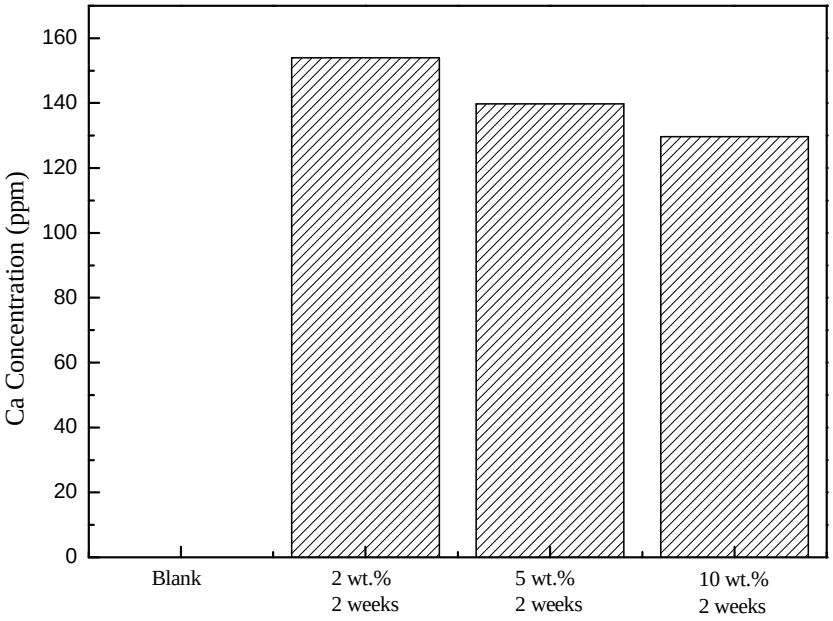

Figure 62. Magnesium concentration from ICP-MS after two week batch experiments with different brine concentrations

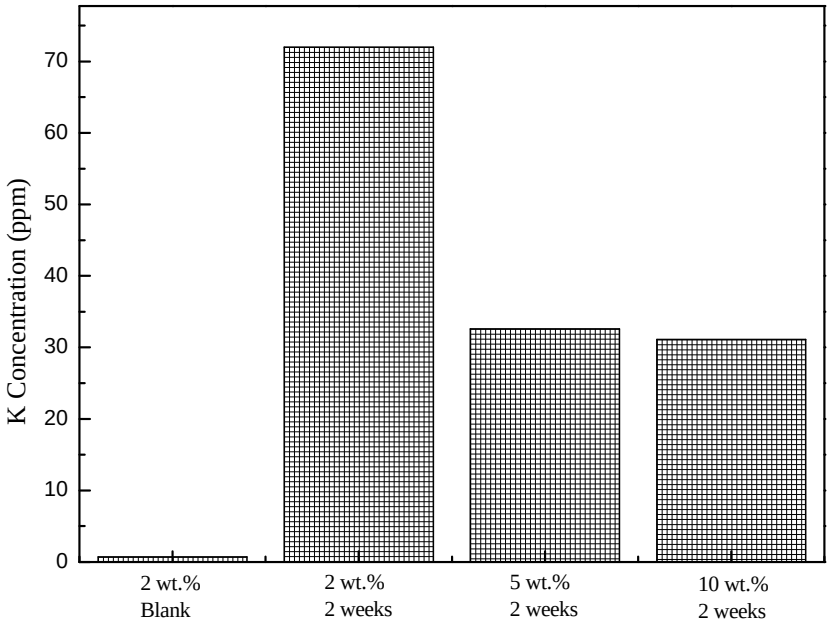

Figure 63. Potassium concentration from ICP-MS after two week batch experiments with different brine concentrations

the different brine concentration has little effect on dissolution mechanisms within the minerals in sandstone.[160-162]

7.7 Summary

Batch experiments were set up and performed at high pressure (2,400 psi) and temperature (60 °C) for two weeks under various experimental conditions. Patterns of mineralogical changes were measured over time using ICP-MS. Iron and magnesium concentration displayed similar trends. During the first 48 hours, there was a rapid increase in iron and magnesium concentration. Calcium has a similar trend over the initial 96 hours. After the point of inflection, the dissolution of iron, magnesium, and calcium containing minerals becomes much slower. Surface area was another factor in the dissolution rate. Surface area changes affected mineral dissolution rates. As expected, increased sample surface area resulted in enhanced mineral dissolution. The QEMSCAN results with the core plugs showed that dissolution on the surface was dominant for sandstone. The changes were more widespread for limestone and dolomite. Brine concentrations were varied as a factor in mineral dissolution. Higher concentration caused lower CO_2 solubility, which in turn caused less mineral dissolution.

CHAPTER 8

PETROPHYSICAL CHANGES IN BATCH REACTOR SYSTEM

8.1 Core Analysis: Micro-CT Imaging

Analysis via Micro-CT was performed on the unreacted and reacted sandstone, limestone, and dolomite core plugs samples only (1/2 inch in length and 3/8 inch in diameter), but not for fracture and powder samples. The Micro-CT machine was capable of supplying the necessary amount of energy to penetrate all the core plugs with a 1.85 micron resolution which was impossible for all the 7 inch cores. The three different core plug scans were taken at the same location for each unreacted and reacted core plugs. Figures 64-66 show the Micro-CT images of sandstone, limestone, and dolomite. Again, by converting to a negative image and showing the void portion of each core plug, the reactivity of each core sample is more readily determined. Figures 64-66 shows a cross section, a solid portion, and a void portion of the unreacted and reacted sandstone, limestone, and dolomite core plugs. Notice the definite porosity change at the circled sections, indicating mineral dissolution within the core. In the cross section 2D images, the spots marked by A, B, and C indicate specific spots on the surface. These markers do not have any other purpose other than to indicate the same spots on the unreacted and reacted surface images.

Figure 64 are the Micro-CT images for sandstone. In the cross-sectional 2D

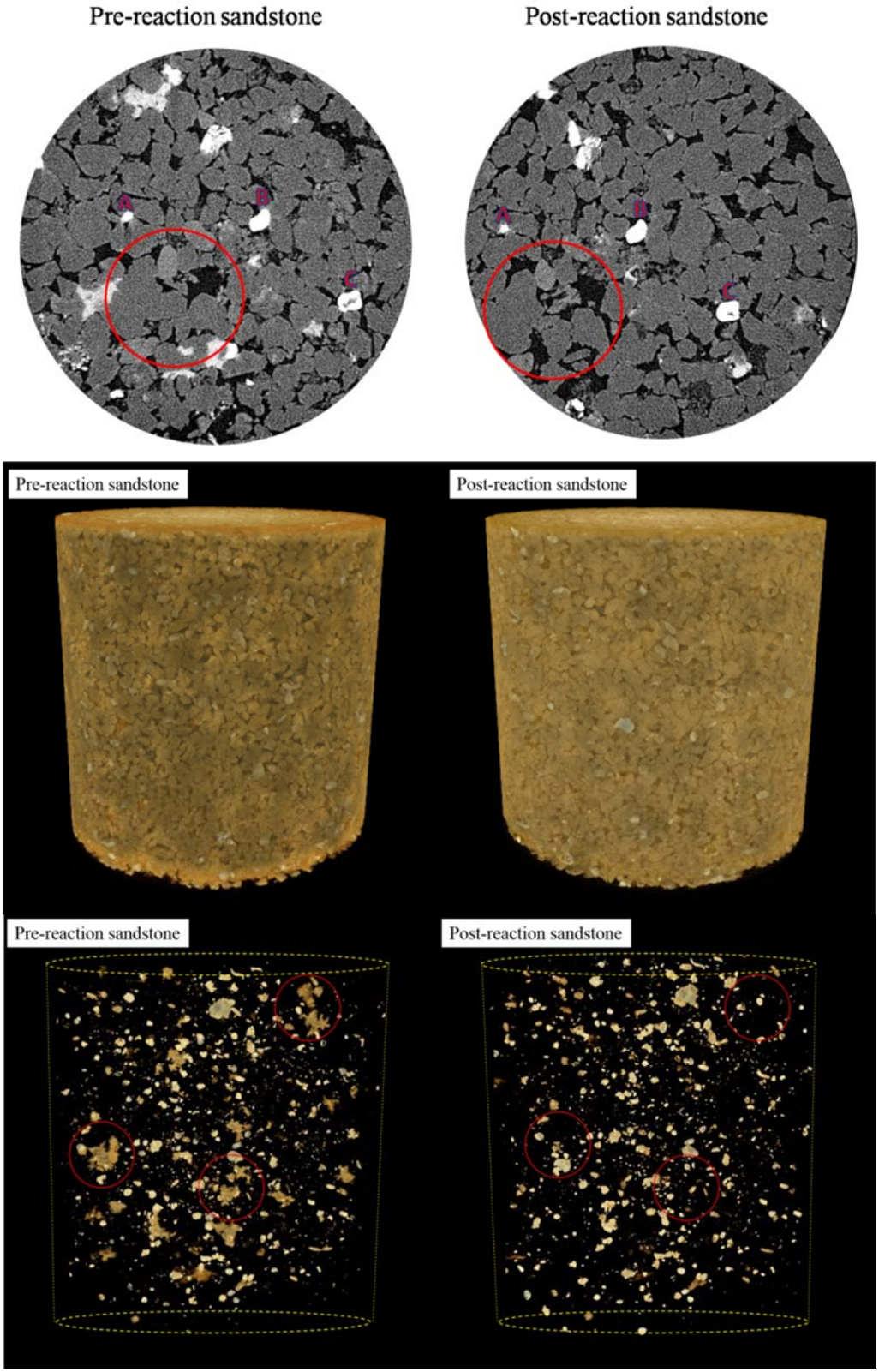

Figure 64. Micro-CT images of sandstone pre- and post-reaction in a batch reactor system

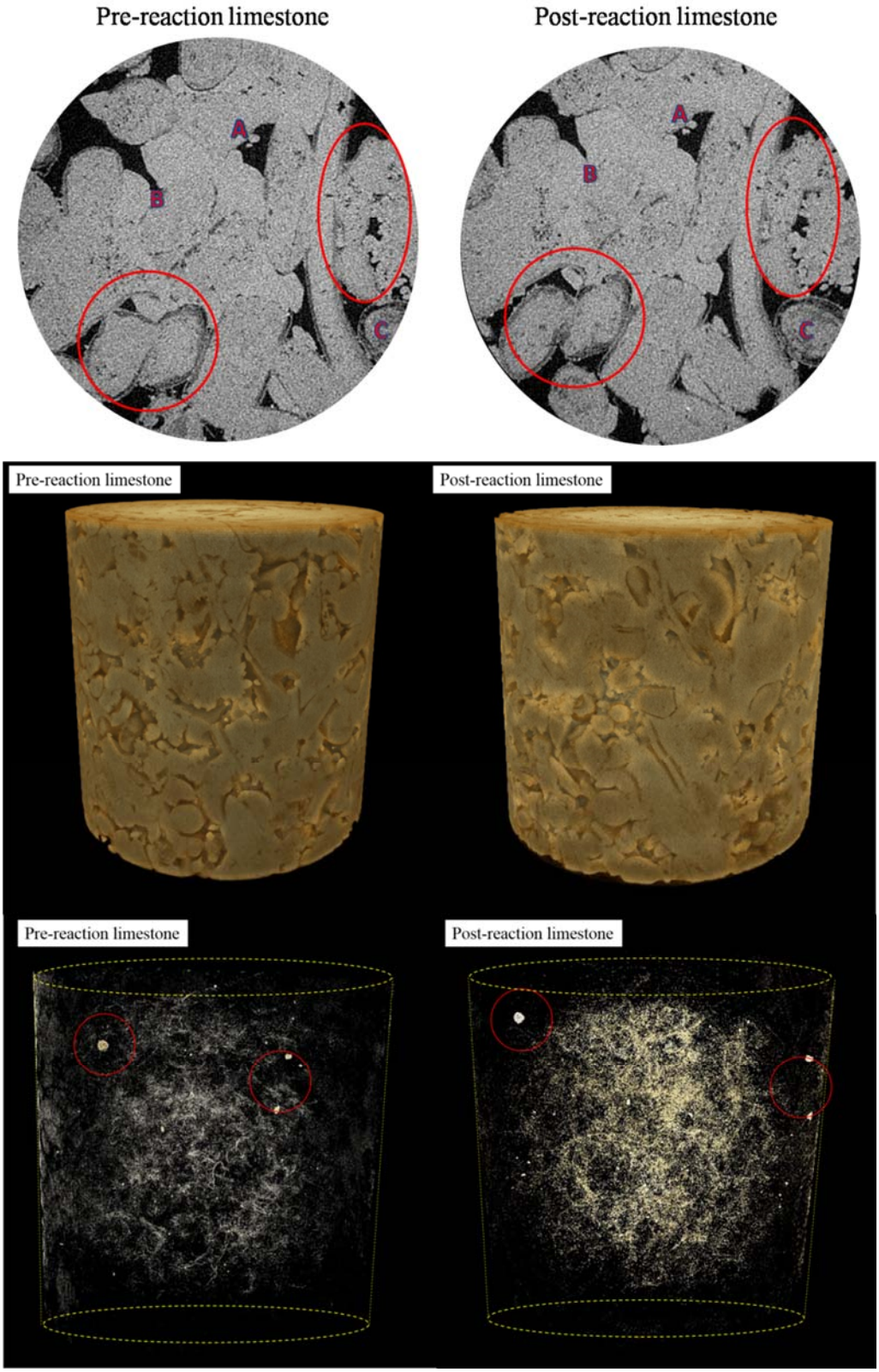

Figure 65. Micro-CT images of limestone pre- and post-reaction in a batch reactor system

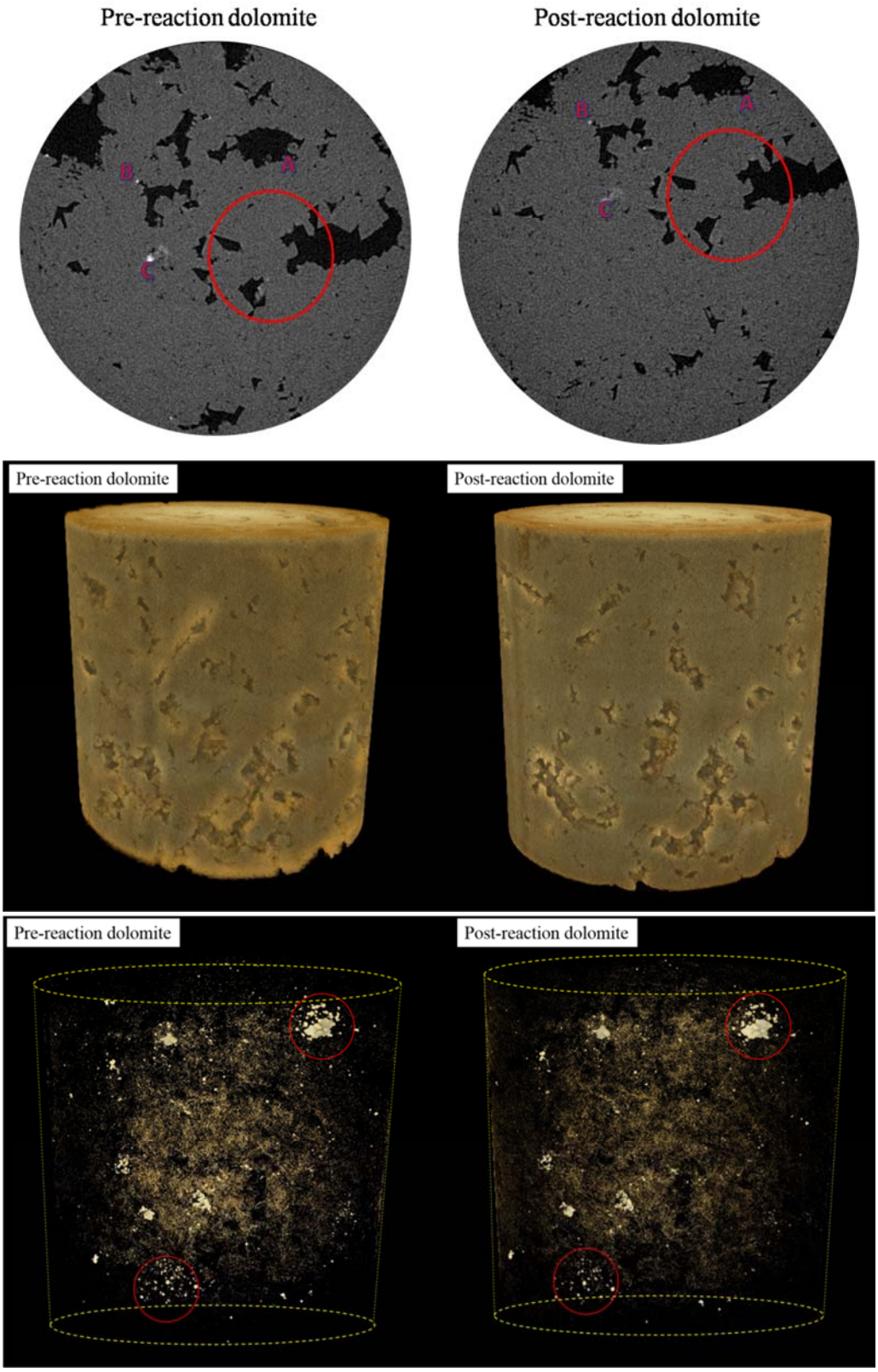

Figure 66. Micro-CT images of dolomite pre- and post-reaction in a batch reactor system

images, the porosity change is easily recognized in the circle area. In the 3D solid image, it is difficult to see mineral dissolution; the images show some differences, but it is hard to see what happened. The 3D negative image shows more clearly the dissolution of minerals within the sandstone core plug, but it is impossible to determine which minerals are dissolved. Based on the previous experiments, the dissolved mineral is thought to be ankerite or reactive clay minerals.

In limestone, Figure 65, the cross-sectional 2D images, the porosity change is easily recognized in the circle area. The reaction expanded the pore size of already existent pores. In the 3D solid image, there are many pore changes on the surface of the core plug, indicating mineral dissolution on the surface. The negative 3D image is cloudier after the reaction, which was also shown in the 7 inch length limestone sample used in the core flooding experiment. The images from the batch experiments are much different than the images from the core flooding experiments. In the batch experiments, the fluid penetration is all particle diffusion, but in core flooding, there is flow through the core. The flow through the core caused mineral dissolution to occur in the core at a much higher reaction rate than in the batch experiments.

Figure 66 shows the dolomite Micro-CT images. In the cross section 2D image, it is hard to detect any porosity change. It is believed that the permeability is much lower than that of sandstone and limestone. Therefore, the fluid does not penetrate the inside of the core as easily. The solid 3D image shows that the surface of the dolomite core plug is dissolved. The 3D negative image shows mineral dissolution on the surfaces of the core plug.

8.2 Core Analysis: Surface Area and Pore Volume

In the post-experiment sample images of QEMSCAN, surface area change is very prominent in the edges of the samples. Also, visible porosity changes in Micro-CT results reveal some minor changes in the fluid-rock interface area over the two-week period. These are some of the evidence that CO_2-related reactions are present to some extent in all studied samples. However, one of the weak points in the Micro-CT analysis is that the surface areas cannot be accurately distinguished on the 2D and 3D images, and the surface area represents the whole surface area of the void mineral interface. The surface area increase is related to the pore volume and pore size decreases. These changes are explained by a decrease in mineral mass/concentration and an increase in the pore volume as porosity increases. Qualitative observations of the Micro-CT images show that pore size increases with reaction time in the sandstone and limestone samples (Figure 64 and Figure 65).[163] However, it can also be seen that the dolomite sample is relatively unreactive and show little to no changes in pore size. Because the Micro-CT results are only a qualitative analysis of surface area, the changes in surface area were measured using the BET. Micro-CT software does exist that could calculate the pore volume based on each slice of the Micro-CT analysis. However, the exterior surface of the core plug would not be adequately measured due to the parameters of the software.

Surface area values for both unreacted and reacted samples according to the BET results were very low, naturally reflecting the low surface areas of the component minerals. Based on Table 8, the unreacted samples have different surface area range; 0.8269 to 1.0953 m^2/g in sandstone, 0.3235 to 1.4086 m^2/g in limestone, and 0.0023 to 1.2132 m^2/g in dolomite; reacted samples have little spacious gap compare with

Table 8. Summary of BET results for the core samples regarding different types and forms

	Surface area (m^2/g)			Pore volume (cm^3/g)						Pore size (Å)					
				BJH Adsorption			BJH Desorption			BJH Adsorption			BJH Desorption		
	Before	After	Variation	Before	After	Variation	Before	After	Variation	Before	After	Variation	Before	After	Variation
Core plug samples															
A 103 II Sandstone	0.8926	1.1095	24.3%	0.003105	0.003447	11.01%	0.006651	0.010389	56.20%	205.146	178.477	-13.00%	284.877	193.789	-31.97%
B 101c II Limestone	0.3235	0.3558	9.98%	0.001996	0.002202	10.32%	0.005659	0.004957	-12.40%	467.950	412.815	-11.78%	507.039	516.123	1.79%
B 109 II Dolomite	0.0023	0.0026	13.04%	0.000276	0.000392	42.02%	0.004264	0.006208	45.59%	758.470	618.912	-18.40%	1108.067	1041.231	-6.03%
Fracture samples															
A 103 I Sandstone	0.8269	1.0888	31.67%	0.004035	0.003462	16.55%	0.010786	0.005411	99.33%	202.368	157.662	-22.09%	424.687	183.089	-56.89%
B 101c I Limestone	0.2740	0.3260	18.98%	0.002172	0.002379	9.53%	0.011667	0.014070	20.60%	665.902	559.280	-16.01%	838.847	844.428	0.67%
B 109 I Dolomite	0.0550	0.0591	7.45%	0.000182	0.000316	73.62%	0.001307	0.002872	119.73%	1056.849	677.555	-35.89%	1040.645	1004.298	-3.49%
Powder samples															
A 103 I Sandstone	1.0953	1.4838	35.47%	0.004544	0.006392	40.67%	0.013551	0.009903	-26.92%	188.044	206.468	9.80%	453.838	275.288	-39.34%
B 101c I Limestone	1.4086	1.6845	19.58%	0.006417	0.008594	33.93%	0.009659	0.019082	-49.38%	230.183	318.434	-27.71%	328.629	521.676	-37.01%
B 109 I Dolomite	1.2132	1.7099	40.94%	0.005749	0.011135	93.69%	0.011996	0.018627	55.28%	251.649	240.143	-4.57%	458.214	419.728	-8.40%

unreacted samples; 1.0888 to 1.4838 m^2/g in sandstone, 0.3558 to 1.5845m^2/g in limestone, and 0.0026 to 1.7099 m^2/g in dolomite. These characteristics result in a small difference in the sandstone surface area due to homogeneity, and large differences in the dolomite and limestone surface areas due to heterogeneity.

When comparing the surface areas before and after the reaction, it can be seen that the surface area increases after the reaction with the least amount of surface area change being 7.45 % and the greatest amount of surface area change being 40.94 %, relatively. The surface area generally increases after the reaction, and the pore size generally decreases after the reaction. The reduced pore size range is from the lowest reduction being 3.49 % and the greatest reduction being 56.89 %. These results imply that despite the very low surface areas, there appears to be a trend that may reflect the dissolution observed during the reaction. This also suggests that the reaction occurs on the core surface, where it generates new pores. The implications of the data infer that the generation of new pores is more dominant than the expansion of existing pores, thus resulting in a lower average pore size and a greater surface area.

If the reactions were to be continued for more than the two-week period, it is speculated that the pore size would increase and the surface area would decrease. This would be the result of new pores being generated and connecting to each other, as well as increased dissolution of the rock. To sum up, the reactions occur primarily on the surface of the minerals, and then secondary pores - new small pores - are generated by the reactions.

8.3 Summary

Mineral dissolution caused the growth and expansion of pores in all mineralogies. To determine petrophysical changes, Micro-CT and BET instruments were used. The 2D cross section Micro-CT results showed pore expansion within the sandstone and limestone core plugs. The 3D solid images showed pore changes on the surface of sandstone, limestone, and dolomite. The 3D negative images displayed removed particles and increased porosity. Surface area changes were measured by BET instruments. Increased surface area in sandstone, limestone, and dolomite ranged from 24.30 % to 35.47 %, 9.98 % to 19.58 %, and 7.45 % to 40.94 %, respectively.

CHAPTER 9

CONCLUSIONS

To better understand mineralogical and petrophysical changes near wellbore host rocks during CO_2 injection, core flooding experiments were designed and set up to model reservoir conditions. Core flooding experiments were performed during which mixtures of CO_2 and brine at different flow rates were injected through near homogenous sandstone, limestone, and dolomite cores at 2000 psi and 60 °C. Mineralogical changes after two weeks of injection have the potential to cause significant petrophysical and subsequent structural changes in sandstone, limestone, and dolomite formations under carbon dioxide sequestration conditions. This was the original hypothesis that was validated using high pressure core floods in this work. Iron chemistry plays an unexpectedly larger role in sequestration in sandstone formations. Dissolution of ankerite and siderite leads to large iron effluent concentrations. A reactive transport model such as TOUGHREACT may be used to explain the complex interconnected reactions with flow. Both simulation and experiment demonstrated the same trend in mineral dissolution, a rapid increase to the critical point and then stabilization. However, some of the flow rate effects observed in the experiments could not be reproduced in the model. In limestone and dolomite, calcium and magnesium bearing minerals dissolve, leading to formation of large dissolution zones, including wormholes. The beginnings of the generation of

wormhole type structures were evident at the lower brine and CO_2 flow rate. And finally, a fully developed wormhole was created in limestone when exposed to higher brine and CO_2 flow rates. Similar to the limestone cores, the inlet sections of dolomite were also greatly dissolved. Porosity and permeability changes are small – of the order of 1-2% and similar values result from TOUGHREACT.

Batch experiments were set up and performed at high pressure (2,400 psi) and temperature (60 °C) for two weeks under various experimental conditions to simulate reservoir conditions for CO_2 storage. These experiments showed similar trends in iron in sandstones, and calcium and magnesium in limestone and dolomite. As the surface areas increase by using fracture and powder samples, reactivities increased leading to larger cationic concentrations in brine. Approximate morphology of the reacted volume is viewed using QEMSCAN and Micro-CT for batch samples. Reactions appear to be uniform throughout the volume for limestone and dolomite, whereas they appear to be limited more to the surface in sandstone. When the brine concentration was increased, CO_2 solubility was affected causing slower mineral dissolution rates.

APPENDIX

TOUGHREACT SIMULATION CODE

The purpose of this appendix is to provide the computer code used for the CO_2 injection simulations used in this study. The code has been annotated to help to readers understand what each input means in the hope that this code could be used by others to perform their own CO_2 injection simulations.

CHEMICAN INPUT

```
# Title
Problem 3:  1_D rad      ial        CO2 injection
#--------------------        ------------------------------------------------------------
# DEFINITION OF THE          GE       OCHEMICAL SYSTEM'
# PRIMARY AQUEOUS S          PEC      IES
'h2o'         0
'h+'          0
'ca+2'        0
'mg+2'        0
'na+'         0
'k+'          0
'fe+2'        0
'sio2(aq)'    0
'hco3-'       0
'alo2-'       0
'cl-'         0
'o2(aq)'      0
'*'

# AQUEOUS KINETICS
'*'

# AQUEOUS COMPLEXES
'oh-'
'al+3'
'halo2(aq)'
'naalo2(aq)'
'aloh+2'
'al(oh)2+'
'al(oh)3(aq)'
'cacl+'
'cacl2(aq)'
'nacl(aq)'
'fecl+'
'fehco3+'
'feco3(aq)'
'fecl4-2'
'nahco3(aq)'
```

```
'cahco3+'
'mghco3+'
'co2(aq)'
'co3-2'
'caco3(aq)'
'kcl(aq)'
'mgcl+'
'nahsio3(aq)'
'caoh+'
'naoh(aq)'
'naco3-'
'h3sio4-'
'fe+3'
'ch4(aq)'
'h2(aq)'
'acetic~acid(aq)'
'*'

# MINERALS   ! e        quilibrium minerals are listed first
'calcite' 0  0  0              0
0. 0. 0.
'quartz'  1          3     0    0
1.023    3e-        14 0 1.0 1.0 87.7 0.0 0.0 0.0    ! prec.
1.023    3e-        14 0 1.0 1.0 87.7 0.0 0.0 0.0  1.e-6   0
0.0   0.    000.00
'kaolinite'       1             3     0    0
6.9183  e-1        4    2   1.0  1.0  22.20  0.0  0.0  0.0
                   2
                   4.8978e-12   65.90    1   'h+'   0.777     ! acid
                   8.9125e-18   17.90    1   'h+'  -0.472     ! base
6.9183  e-1        4    0   1.0  1.0  22.20  0.0  0.0  0.0  1.e-6   0
0.0   0.    000.00
'illite'       1                3     0    0
1.6596  e-1        3    2   1.0  1.0  35.00  0.0  0.0  0.0
                   2
                   1.0471e-11   23.6    1   'h+'  0.34
                   3.0200e-17   58.9    1   'h+' -0.40
1.6596  e-1        3  0  1.0  1.0  35.00  0.0  0.0  0.0  1.e-6   0
0.0   0.    000.00
'oligoclase'                   1      3     0    0
1.4454  e-1        3    2   1.0  1.0  69.80  0.0  0.0  0.0
                   1
                   2.1380e-11   65.0    1   'h+'  0.457
1.4454  e-1        3  0  1.0  1.0  69.80  0.0  0.0  0.0  1.e-6   0
0.0   0.    000.00
'smectite-na'      1          3     0    0
1.6596  e-1        3    2   1.0  1.0  35.00  0.0  0.0  0.0
                   2
                   1.0471e-11   23.6    1   'h+'  0.34
                   3.0200e-17   58.9    1   'h+' -0.40
1.6596  e-1        3  0  1.0  1.0  35.00  0.0  0.0  0.0  1.e-6   0
```

```
0.0   0.    000.00
'k-feldspar'    1           3    0    0
3.8905  e-1       3    2   1.0  1.0  38.00  0.0  0.0  0.0
                  2
                  8.7096e-11   51.7    1   'h+'   0.5      ! acid mechanism
                  6.3096e-22   94.1    1   'h+'  -0.823    ! base
3.8905  e-1       3  0  1.0  1.0  38.00  0.0  0.0  0.0  1.e-6   0
0.0   0.    000.00
'chlorite'    1             3    0    0
3.02      e-1       0  2  1.0  1.0  88.00  0.0  0.0  0.0
                  1
                  7.7624e-12   88.0    1   'h+'   0.5      ! acid mechanism
3.02      e-1       3  0  1.0  1.0  88.00  0.0  0.0  0.0  1.e-6   0
0.0   0.    000.00
'siderite-2'        1          3    0    0
9.00E+00          7          2   1.0  1.0  62.76  0.0  0.0  0.0
                  1
                  6.4565e-04  36.1    1   'h+'   0.5
1.2589  e-0       9    0   1.0  1.0  62.76  0.0  0.0  0.0  1.e-6   0
0.0   0.    000.00
'ankerite-2'        1          3    0    0
1.2598  e-0       9    2   1.0  1.0  62.76  0.0  0.0  0.0
                  1
                  6.4565e-04  36.1    1   'h+'   0.5
1.2589  e-0       9    0   1.0  1.0  62.76  0.0  0.0  0.0  1.e-6   0
0.0   0.    000.00
'*'

# GASES
'co2(g)'   0
'*'

# SURFACE COMPLEXES
'*'

# Secies with Kd an       d d       ecay
'*'

# EXCHANGEABLE CATI       ONS
'*'

#---------------------        ------------------------------------------------------
# INITIAL AND BOUND          ARY     WATER TYPES
1   1   !niwtype, n          bwt       ype = number of initial and boundary waters

# Index  Speciation        T(         C)  P(bar)
1        60.0                    "138.0E0                      "

#        icon        g          uess         ctot   constraint log(Q/K)
'h2o'      1    0.1  0          E+01    0.1000E+01    ' '     0.0
'na+'      1    0.3  480        E-05    0.3480E-05    ' '     0.0
```

```
'cl-'      1    0.3   480       E-05    0.3480E-05    ' '     0.0
'h+'       1    1.0   0         E-07    1.0000E-07    ' '     0.0
'ca+2'     1    1.0 0           E-15    1.0000E-15    ' '     0.0
'mg+2'     1    1.0             0         E-15    1.0000E-15    ' '     0.0
'k+'       1    1.0   0         E-15    1.0000E-15    ' '     0.0
'fe+2'     1    1.0 0           E-15    1.0000E-15    ' '     0.0
'sio2(aq)' 1    1.0             0         E-15    1.0000E-15    ' '     0.0
'hco3-'    1    1.0 0           E-15    1.0000E-15    ' '     0.0
'alo2-'    1    1.0 0           E-15    1.0000E-15    ' '     0.0
'o2(aq)'   1    1.00            E-65    1.0000E-65    ' '     0.0
'*'

# Index  Speciation        T(        C)  P(bar)
1        60.0                  1.40E+02

#        icon          g          uess         ctot   constraint log(Q/K)
'h2o'      1    0.1  0          E+01    0.1000E+01    ' '     0.0
'na+'      1    0.3  480        E-06    0.3480E-05    ' '     0.0
'cl-'      1    0.3   480       E-06    0.3480E-05    ' '     0.0
'h+'       1    8.2   134       E-04    2.2806E-02    ' '     0.0
'ca+2'     1    1.0 0           E-15    1.0000E-15    ' '     0.0
'mg+2'     1    1.0             0         E-15    1.0000E-15    ' '     0.0
'k+'       1    1.0   0         E-15    1.0000E-15    ' '     0.0
'fe+2'     1    1.0 0           E-15    1.0000E-15    ' '     0.0
'sio2(aq)' 1    1.0             0         E-15    1.0000E-15    ' '     0.0
'hco3-'    1    0.2 300         E-02    0.2300E-01    ' '     0.0
'alo2-'    1    1.0 0           E-15    1.0000E-15    ' '     0.0
'o2(aq)'   1    1.00            E-65    1.0000E-65    ' '     0.0
'*'

#----------------------        ------------------------------------------------------------
# INITIAL MINERAL Z            ONE     S
2              !nm    typ       e= number of mineral zones

#Mineral zone 1
1              !im    typ       e= index of mineral zone
# 'mineral          vol       .frac.'
'calcite'      0.0    0         0
'quartz'  0           .6085     1
0.0             98    .0e       -1        0
'kaolinite'           0         .0234     1
0.0          1516.    3e-       1         0
'illite'    0         .0449     1
0.0          1516.    3e-       1         0
'oligoclase'          0         .0216     1
0.0             98.   0e-       1         0
'smectite-na'         0         .0054     1
0.0          1516.    3e-       1         0
'k-feldspar'          0         .0428     1
0.0             98.   0e-       1         0
'chlorite'            0         .0065     1
```

```
0.0          98.   0e-      1        0
'siderite-2'      0        .0008    1
0.0          98.   0e-      1        0
'ankerite-2'      0        0019     1
0.0          98.   0e-      1        0
'*'
#Mineral zone 2, fo      r t       he injection cell only
2            !im   typ      e= index of mineral zone
# 'mineral        vol      .frac.'
'calcite'    0.0   0        0
'quartz'  0        .6085    1
0.0          0.    0e-      0        0
'kaolinite'       0        .0234    1
0.0          0.    0e-      0        0
'illite'    0     .0449    1
0.0          0.    0e-      0        0
'oligoclase'      0        .0216    1
0.0          0.    0e-      0        0
'smectite-na'     0        .0054    1
0.0          0.    0e-      0        0
'k-feldspar'      0        .0428    1
0.0          0.    0e-      0        0
'chlorite'        0        .0065    1
0.0          0.    0e-      0        0
'siderite-2'      0        .0008    1
0.0          0.    0e-      0        0
'ankerite-2'      0        0019     1
0.0          0.    0e-      0        0
'*'

#---------------------      ----------------------------------------------------------
# INITIAL an Inject       ion       Gas ZONES
1    0              !ngtype= number of gas zones

# Gas Zone 1
1                   !igtype
#'gas     partial  pre      ssure'    !at 25 C equil w/ water
'co2(g)' 0
'*'

#---------------------      ----------------------------------------------------------
#'Permeability-Poro      sit       y Zones'
1

# Perm-poros zone 1
1
# perm law   a-par        b         #NAME?
3    0.0000E+00         0.00E+00
'*'

#---------------------      ----------------------------------------------------------
```

```
# INITIAL SURFACE A          DSO     RPTION ZONES'
'*'

#--------------------        ----------------------------------------------------------

# INITIAL LINEAR EQ          UIL     IBRIUM Kd ZONE
'*'

#--------------------        ----------------------------------------------------------
# INITIAL ZONES OF  CAT     ION EXCHANGE
'*'

#--------------------        ----------------------------------------------------------
#'end'


File is not read be        low     the 'end' above

Exsample sandstone         wat     er composition

'h2o'      1          1          000d+0      1.000d+0    ' '  0.0    !    Sandstone
'h+'       3          4          5415d-8     4.5415d-8   ' '  0.0    ! pH=7.3427
'ca+2'     1          1          000d-3      3.232d-3    ' '  0.0
'mg+2'     1          1          000d-7      1.532d-7    ' '  0.0
'na+'      1          0          900d-0      0.9889d-0   ' '  0.0
'k+'       1          1          000d-3      7.517d-3    ' '  0.0
'fe+2'     1          1          000d-6      2.421d-5    ' '  0.0
'sio2(aq)' 1          1          000d-4      7.262d-4    ' '  0.0
'hco3-'    1          1          000d-2      4.320d-2    ' '  0.0
'so4-2'    1          1          000d-17     1.323d-9    ' '  0.0
'alo2-'    1          1          000d-10     2.657d-8    ' '  0.0
'cl-'      1          1          000d-0      1.000d+0    ' '  0.0
'o2(aq)'   3          4          879d-68     4.879d-68   ' '  0.0
'*'

'co2(g)'   0
0     0                !ngtype= number of gas zones
# Gas Zone 1
1                      !igtype
#'gas      partial  pre       ssure'    !at 25 C equil w/ water
'co2(g)' 0

'h+'       1    0.8  480       E-07    0.4320E-01    ' '     0.0
'ca+2'     1    0.4 479        E-02    0.4737E-02    ' '     0.0
'mg+2'     1    0.2            348      E-04    0.2669E-04    ' '     0.0
'k+'       1    0.5  805       E-02    0.5980E-02    ' '     0.0
'fe+2'     1    0.2  615       E-06    0.3022E-06    ' '     0.0
'sio2(aq)' 1    0.9            203      E-03    0.1034E-02    ' '     0.0
'hco3-'    1    0.1 841        E-02    0.4562E-01    ' '     0.0
'so4-2'    1    0.1 443        E-15    0.1324E-08    ' '     0.0
'alo2-'    1    0.1  78        E-07    0.1361E-07    ' '     0.0
```

```
'o2(aq)'   1    0.2763      E-65   -0.8646E-01    ' '     0.0

'calcite'      0.0   192      9         0
'quartz'  0          .7783    1
0.0            98    .0e      -1        0
'kaolinite'          0        .0299     1
0.0          1516.   3e-      1         0
'illite'    0        .0574    1
0.0          1516.   3e-      1         0
'oligoclase'         0        .0277     1
0.0            98.   0e-      1         0
'smectite-na'        0        .0069     1
0.0          1516.   3e-      1         0
'k-feldspar'         0        .0547     1
0.0            98.   0e-      1         0
'chlorite'   0.008 3          1
0.0            98.   0e-      1         0
'siderite-2'                  0.001     1
0.0            98.   0e-      1         0

#            1.259  8e-       04    2   1.0  1.0  62.76  0.0  0.0  0.0
```

FLOW INPUT

```
# Problem 3: 1-D radial flow problem for CO2 injection into a saline aquifer
ROCKS----1----*----2----*----3----*----4----*----5----*----6----*----7----*----8
SAND     2  2080.e00       .21   45.e-15   45.e-15   45.e-15      2.51      920.
4.50E-10
   7          .457       .30        1.       .05
   7          .457       .00     5.1e-5      1.e7      .999

MULTI----1----*----2----*----3----*----4----*----5----*----6----*----7----*----8
   3    3    3    6
SELEC....2....3....4....5....6....7....8....9...10...11...12...13...14...15...16
   1                                   0    0    0    0    0    0    2
     3.0   .8
SOLVR----1----*----2----*----3----*----4----*----5----*----6----*----7----*----8
5  Z1   O0    8.0e-1    1.0e-7
START----1----*----2----*----3----*----4----*----5----*----6----*----7----*----8
REACT----1MOPR(20)-2----*----3----*----4----*----5----*----6----*----7----*----8
201040000
----*----1 MOP: 123456789*123456789*1234 ---*----5----*----6----*----7----*----8
PARAM----1----*----2----*----3----*----4----*----5----*----6----*----7----*----8
  19999    9999 000 01000010  41000500
          1.21E06  1.800E02  1.800E04AU1 1           9.81
    1.E-4     1.E00
            138.e5               .02            0.00000               60.
```

```
TIMES----1----*----2----*----3----*----4----*----5----*----6----*----7----*----8
4
 3.15569E3 1.57788E4 3.15569E5 1.07788E6
ELEME----1----*----2----*----3----*----4----*----5----*----6----*----7----*----8
BDY 2              10.1000E+300.5000E-04          0.1000E-020.1250E-01-.9000E-03 ! Infinitive
block for the boundary
A11-1          10.1470E-040.4900E-02        0.3500E-010.3500E-01-.1500E-02
A21 1          10.1470E-040.0000E+00         0.3500E-010.3500E-01-.4500E-02
A31 1          10.1470E-040.0000E+00         0.3500E-010.3500E-01-.7500E-02
A41 1          10.1470E-040.0000E+00         0.3500E-010.3500E-01-.1050E-01
A51 1          10.1470E-040.0000E+00         0.3500E-010.3500E-01-.1350E-01
A61 1          10.1470E-040.0000E+00         0.3500E-010.3500E-01-.1650E-01
A71 1          10.1470E-040.0000E+00         0.3500E-010.3500E-01-.1950E-01
A81 1          10.1470E-040.0000E+00         0.3500E-010.3500E-01-.2250E-01
A91 1          10.1470E-040.0000E+00         0.3500E-010.3500E-01-.2550E-01
AA1 1           10.1470E-040.0000E+00         0.3500E-010.3500E-01-.2850E-01
AB1 1           10.1470E-040.0000E+00         0.3500E-010.3500E-01-.3150E-01
AC1 1           10.1470E-040.0000E+00         0.3500E-010.3500E-01-.3450E-01
AD1 1           10.1470E-040.0000E+00         0.3500E-010.3500E-01-.3750E-01
AE1 1           10.1470E-040.0000E+00         0.3500E-010.3500E-01-.4050E-01
AF1 1          10.1470E-040.0000E+00         0.3500E-010.3500E-01-.4350E-01
AG1 1           10.1470E-040.0000E+00         0.3500E-010.3500E-01-.4650E-01
AH1 1           10.1470E-040.0000E+00         0.3500E-010.3500E-01-.4950E-01
AI1 1          10.1470E-040.0000E+00        0.3500E-010.3500E-01-.5250E-01
AJ1 1          10.1470E-040.0000E+00        0.3500E-010.3500E-01-.5550E-01
AK1 1           10.1470E-040.0000E+00         0.3500E-010.3500E-01-.5850E-01
AL1 1           10.1470E-040.0000E+00         0.3500E-010.3500E-01-.6150E-01
AM1 1            10.1470E-040.0000E+00          0.3500E-010.3500E-01-.6450E-01
AN1 1           10.1470E-040.0000E+00         0.3500E-010.3500E-01-.6750E-01
AO1 1           10.1470E-040.0000E+00         0.3500E-010.3500E-01-.7050E-01
AP1 1          10.1470E-040.0000E+00        0.3500E-010.3500E-01-.7350E-01
AQ1 1           10.1470E-040.0000E+00         0.3500E-010.3500E-01-.7650E-01
AR1 1           10.1470E-040.0000E+00         0.3500E-010.3500E-01-.7950E-01
AS1 1          10.1470E-040.0000E+00         0.3500E-010.3500E-01-.8250E-01
AT1 1          10.1470E-040.0000E+00         0.3500E-010.3500E-01-.8550E-01
AU1 1           10.1470E-040.0000E+00         0.3500E-010.3500E-01-.8850E-01
AV1 1          10.1470E-040.0000E+00         0.3500E-010.3500E-01-.9150E-01
AW1 1            10.1470E-040.0000E+00          0.3500E-010.3500E-01-.9450E-01
AX1 1           10.1470E-040.0000E+00         0.3500E-010.3500E-01-.9750E-01
AY1 1          10.1470E-040.0000E+00         0.3500E-010.3500E-01-.1005E+00
AZ1 1          10.1470E-040.0000E+00         0.3500E-010.3500E-01-.1035E+00
B11 1          10.1470E-040.0000E+00        0.3500E-010.3500E-01-.1065E+00
B21 1          10.1470E-040.0000E+00        0.3500E-010.3500E-01-.1095E+00
B31 1          10.1470E-040.0000E+00        0.3500E-010.3500E-01-.1125E+00
B41 1          10.1470E-040.0000E+00        0.3500E-010.3500E-01-.1155E+00
B51 1          10.1470E-040.0000E+00        0.3500E-010.3500E-01-.1185E+00
B61 1          10.1470E-040.0000E+00        0.3500E-010.3500E-01-.1215E+00
B71 1          10.1470E-040.0000E+00        0.3500E-010.3500E-01-.1245E+00
B81 1          10.1470E-040.0000E+00        0.3500E-010.3500E-01-.1275E+00
B91 1          10.1470E-040.0000E+00        0.3500E-010.3500E-01-.1305E+00
BA1 1           10.1470E-040.0000E+00         0.3500E-010.3500E-01-.1335E+00
```

```
BB1 1          10.1470E-040.0000E+00        0.3500E-010.3500E-01-.1365E+00
BC1 1          10.1470E-040.0000E+00        0.3500E-010.3500E-01-.1395E+00
BD1 1          10.1470E-040.0000E+00        0.3500E-010.3500E-01-.1425E+00
BE1 1          10.1470E-040.0000E+00        0.3500E-010.3500E-01-.1455E+00
BF1 1          10.1470E-040.0000E+00        0.3500E-010.3500E-01-.1485E+00
BG1 1          10.1470E-040.0000E+00        0.3500E-010.3500E-01-.1515E+00
BH1 1          10.1470E-040.0000E+00        0.3500E-010.3500E-01-.1545E+00
BI1 1          10.1470E-040.0000E+00        0.3500E-010.3500E-01-.1575E+00
BJ1 1          10.1470E-040.0000E+00        0.3500E-010.3500E-01-.1605E+00
BK1 1          10.1470E-040.0000E+00        0.3500E-010.3500E-01-.1635E+00
BL1 1          10.1470E-040.0000E+00        0.3500E-010.3500E-01-.1665E+00
BM1 1          10.1470E-040.0000E+00        0.3500E-010.3500E-01-.1695E+00
BN1 1          10.1470E-040.0000E+00        0.3500E-010.3500E-01-.1725E+00
BO1 1          10.1470E-040.0000E+00        0.3500E-010.3500E-01-.1755E+00
BP1 1          10.1470E-040.4900E-02        0.3500E-010.3500E-01-.1785E+00
BDY 1          10.8751E-040.5000E-04        0.1000E-020.1250E-01-.1815E+00

CONNE----1----*----2----*----3----*----4----*----5----*----6----*----7----*----8
BDY 2A11-1          30.1000E-020.1000E-020.5000E-040.1000E+01
A11-1A21 1          30.1500E-020.1500E-020.4900E-020.1000E+01
A21 1A31 1          30.1500E-020.1500E-020.4900E-020.1000E+01
A31 1A41 1          30.1500E-020.1500E-020.4900E-020.1000E+01
A41 1A51 1          30.1500E-020.1500E-020.4900E-020.1000E+01
A51 1A61 1          30.1500E-020.1500E-020.4900E-020.1000E+01
A61 1A71 1          30.1500E-020.1500E-020.4900E-020.1000E+01
A71 1A81 1          30.1500E-020.1500E-020.4900E-020.1000E+01
A81 1A91 1          30.1500E-020.1500E-020.4900E-020.1000E+01
A91 1AA1 1          30.1500E-020.1500E-020.4900E-020.1000E+01
AA1 1AB1 1          30.1500E-020.1500E-020.4900E-020.1000E+01
AB1 1AC1 1          30.1500E-020.1500E-020.4900E-020.1000E+01
AC1 1AD1 1          30.1500E-020.1500E-020.4900E-020.1000E+01
AD1 1AE1 1          30.1500E-020.1500E-020.4900E-020.1000E+01
AE1 1AF1 1          30.1500E-020.1500E-020.4900E-020.1000E+01
AF1 1AG1 1          30.1500E-020.1500E-020.4900E-020.1000E+01
AG1 1AH1 1          30.1500E-020.1500E-020.4900E-020.1000E+01
AH1 1AI1 1          30.1500E-020.1500E-020.4900E-020.1000E+01
AI1 1AJ1 1          30.1500E-020.1500E-020.4900E-020.1000E+01
AJ1 1AK1 1          30.1500E-020.1500E-020.4900E-020.1000E+01
AK1 1AL1 1          30.1500E-020.1500E-020.4900E-020.1000E+01
AL1 1AM1 1          30.1500E-020.1500E-020.4900E-020.1000E+01
AM1 1AN1 1          30.1500E-020.1500E-020.4900E-020.1000E+01
AN1 1AO1 1          30.1500E-020.1500E-020.4900E-020.1000E+01
AO1 1AP1 1          30.1500E-020.1500E-020.4900E-020.1000E+01
AP1 1AQ1 1          30.1500E-020.1500E-020.4900E-020.1000E+01
AQ1 1AR1 1          30.1500E-020.1500E-020.4900E-020.1000E+01
AR1 1AS1 1          30.1500E-020.1500E-020.4900E-020.1000E+01
AS1 1AT1 1          30.1500E-020.1500E-020.4900E-020.1000E+01
AT1 1AU1 1          30.1500E-020.1500E-020.4900E-020.1000E+01
AU1 1AV1 1          30.1500E-020.1500E-020.4900E-020.1000E+01
AV1 1AW1 1          30.1500E-020.1500E-020.4900E-020.1000E+01
AW1 1AX1 1          30.1500E-020.1500E-020.4900E-020.1000E+01
```

```
AX1 1AY1 1               30.1500E-020.1500E-020.4900E-020.1000E+01
AY1 1AZ1 1               30.1500E-020.1500E-020.4900E-020.1000E+01
AZ1 1B11 1               30.1500E-020.1500E-020.4900E-020.1000E+01
B11 1B21 1               30.1500E-020.1500E-020.4900E-020.1000E+01
B21 1B31 1               30.1500E-020.1500E-020.4900E-020.1000E+01
B31 1B41 1               30.1500E-020.1500E-020.4900E-020.1000E+01
B41 1B51 1               30.1500E-020.1500E-020.4900E-020.1000E+01
B51 1B61 1               30.1500E-020.1500E-020.4900E-020.1000E+01
B61 1B71 1               30.1500E-020.1500E-020.4900E-020.1000E+01
B71 1B81 1               30.1500E-020.1500E-020.4900E-020.1000E+01
B81 1B91 1               30.1500E-020.1500E-020.4900E-020.1000E+01
B91 1BA1 1               30.1500E-020.1500E-020.4900E-020.1000E+01
BA1 1BB1 1               30.1500E-020.1500E-020.4900E-020.1000E+01
BB1 1BC1 1               30.1500E-020.1500E-020.4900E-020.1000E+01
BC1 1BD1 1               30.1500E-020.1500E-020.4900E-020.1000E+01
BD1 1BE1 1               30.1500E-020.1500E-020.4900E-020.1000E+01
BE1 1BF1 1               30.1500E-020.1500E-020.4900E-020.1000E+01
BF1 1BG1 1               30.1500E-020.1500E-020.4900E-020.1000E+01
BG1 1BH1 1               30.1500E-020.1500E-020.4900E-020.1000E+01
BH1 1BI1 1               30.1500E-020.1500E-020.4900E-020.1000E+01
BI1 1BJ1 1               30.1500E-020.1500E-020.4900E-020.1000E+01
BJ1 1BK1 1               30.1500E-020.1500E-020.4900E-020.1000E+01
BK1 1BL1 1               30.1500E-020.1500E-020.4900E-020.1000E+01
BL1 1BM1 1               30.1500E-020.1500E-020.4900E-020.1000E+01
BM1 1BN1 1               30.1500E-020.1500E-020.4900E-020.1000E+01
BN1 1BO1 1               30.1500E-020.1500E-020.4900E-020.1000E+01
BO1 1BP1 1               30.1500E-020.1500E-020.4900E-020.1000E+01
BP1 1BDY 1               30.1500E-020.1000E-020.5000E-040.1000E+01

GENER----1----*----2----*----3----*----4----*----5----*----6----*----7----*----8
BDY 1inj 3               0    WATE  1.654E-05
BDY 1inj 2               0    COM2  3.333E-07
BDY 1inj 1               0    COM3  0.165E-04

INCON----1----*----2----*----3----*----4----*----5----*----6----*----7----*----8
BDY 1
          138.e5              .02             0.285               60.
BDY 2
          138.e5              .02                              60.

ENDCY----1----*----2----*----3----*----4----*----5----*----6----*----7----*----8




MESHMAKER1----*----2----*----3----*----4----*----5----*----6----*----7----*----8
XYZ
0
NX       1  7.00E-02
```

```
NY       1  7.00E-02
NZ      60  3.00E-03

MESHMAKER1----*----2----*----3----*----4----*----5----*----6----*----7----*----8
RZ2D
RADII
1
0
EQUID
   1           .3
LOGAR
  20          5.E2
EQUID
  10         100.0
EQUID
  10         200.0
LOGAR
   9         1.E4
LAYER----1----*----2----*----3----*----4----*----5----*----6----*----7----*----8
1
100
BDY 1            10.8751E+080.5000E-04         0.1000E-020.1250E-01-.1000E-00
BF1 1BDY 1                 30.1000E-020.1000E-020.5000E-040.1000E+01
BDY 1A11 1                 30.1000E-020.1000E-020.5000E-040.1000E+01
BDY 1inj 1                 0    COM3  1.800E-03
BDY 1inj 2                 0    COM2  5.000E+01
BDY 1inj 3                 0    COM1  5.000E+03
BDY 2
                          .02                          60.


ENDFI----1----*----2----*----3----*----4----*----5----*----6----*----7----*----8
```

SOLUTE INPUT

```
# Title
Problem 3: 1-D CO2 injection

#options for reactive chemical transport
# ISPIA ITERSFA ISOLVC NGAMM NGAS1 ichdump kcpl Ico2h2o  nu
   2      1     5     1   1      0      1     2      0

#constraints for reactive chemical transport
# SL1MIN        rcour     STIMAX    CNFACT(=1 fully implicit)
  1.00e-5       0.0       4.0       1.0

#Read input and output file names:
```

```
databas1.dat                ! thermodynamic database
iter.out                    ! iteration information
co2d_conc.out               ! aqueous concentrations in tecplot form
co2d_min.out                ! mineral data  in tecplot form
co2d_gas.out                ! gas data  in tecplot form
co2d_tim.out                ! concentrations at specific elements over time

# Weighting space/time, aq. and gas diffusion coeffs
# ITIME     WUPC   DFFUN     DFFUNG
  1.0       1.0   1.0d-09   1.1d-05

# Convergence and tolerance parameters
# MAXITPTR  TOLTR    MAXITPCH  TOLCH    NOT-USED  NOT-USED    TOLDC
TOLDR
   1      0.100E-03    200   0.100E-05   0.0       0.0        0.0      0.0

# Printout control variables:
# NWTI NWNOD NWCOM NWMIN NWAQ NWADS NWEXC iconflag minflag  igasflag
  10    1     0    0     1    0    0       3      2        0

# Nodes for which to output data in time file (15a5):
A11-1

# Primary (total) aqueous species for which to output concentrations in time and plot files:
0

# Minerals for which to output data in time and plot files:
0

# Individual aqueous species for which to output concentrations in time and plot files:
30

# Adsorption species for which to output concentrations in time and plot files:

# Exchange species for which to output concentrations in time and plot files:

# Default types of chemical zones
# Initial  Boundary                                Porosity/
#  Water    Water    Minerals   Gases Adsorption Exchange  Permeab  Kd zones Inj Gas
# IZIWDF   IZBWDF    IZMIDF   IZGSDF   IZADDF    IZEXDF   IZPPDF    IZKDDF
IZBGDF
    1        0        1        1       0         0        1         0       0

# Types of chemical zones for specific nodes (optional)
# Elem    #Seq   Incr  Water  Water Min  Gases Adsorp  Exchg  Perm    Kd    Inj Gas
# ELEM(a5) NSEQ  NADD  IZIW   IZBW  IZMI  IZGS  IZAD   IZEX   izpp   IZKD    IZBG
BDY 1      0     0    1      1     2     1     0      0      1      0       0

# this "end" record is needed now
end
```

REFERENCES

1. Sohrabi, M.; Kechut, N. I.; Riazi, M.; Jamiolahmady, M.; Ireland, S.; Robertson, G., Coreflooding Studies to Investigate the Potential of Carbonated Water Injection as an Injection Strategy for Improved Oil Recovery and CO_2 Storage. *Transport in Porous Media* **2012,** 91, (1), 101-121.

2. Wang, Q.; Luo, J.; Zhong, Z.; Borgna, A., CO_2 capture by solid adsorbents and their applications: Current status and new trends. *Energy and Environmental Science* **2011,** 4, (1), 42-55.

3. Salimi, H.; Wolf, K.-H.; Bruining, J., The influence of capillary pressure on the phase equilibrium of the CO_2–water system: Application to carbon sequestration combined with geothermal energy. *International Journal of Greenhouse Gas Control* **2012,** 11, Supplement, S47-S66.

4. Hoffert, M. I.; Caldeira, K.; Benford, G.; Criswell, D. R.; Green, C.; Herzog, H.; Jain, A. K.; Kheshgi, H. S.; Lackner, K. S.; Lewis, J. S.; Lightfoot, H. D.; Manheimer, W.; Mankins, J. C.; Mauel, M. E.; Perkins, L. J.; Schlesinger, M. E.; Volk, T.; Wigley, T. M. L., Engineering: Advanced technology paths to global climate stability: Energy for a greenhouse planet. *Science* **2002,** 298, (5595), 981-987.

5. Oelkers, E. H.; Schott, J., Geochemical aspects of CO_2 sequestration. *Chemical Geology* **2005,** 217, (3–4), 183-186.

6. Keeling, C. D., Climate change and carbon dioxide: An introduction. *Proceedings of the National Academy of Sciences* **1997,** 94, (16), 8273-8274.

7. Olajire, A. A., A review of mineral carbonation technology in sequestration of CO_2. *Journal of Petroleum Science and Engineering* **2013,** 109, 364-392.

8. Siegenthaler, U.; Oeschger, H., Biospheric CO_2 emissions during the past 200 years reconstructed by deconvolution of ice core data. *Tellus B* **1987,** 39, (1-2), 140-154.

9. Bachu, S.; Bennion, D. B., Chromatographic partitioning of impurities contained in a CO_2 stream injected into a deep saline aquifer: Part 1. Effects of gas composition and in situ conditions. *International Journal of Greenhouse Gas Control* **2009,** 3, (4), 458-467.

10. Court, B.; Bandilla, K. W.; Celia, M. A.; Janzen, A.; Dobossy, M.; Nordbotten, J. M., Applicability of vertical-equilibrium and sharp-interface assumptions in CO_2 sequestration modeling. *International Journal of Greenhouse Gas Control* **2012,** 10, 134-147.

11. Mora, C.; Frazier, A. G.; Longman, R. J.; Dacks, R. S.; Walton, M. M.; Tong, E. J.; Sanchez, J. J.; Kaiser, L. R.; Stender, Y. O.; Anderson, J. M.; Ambrosino, C. M.; Fernandez-Silva, I.; Giuseffi, L. M.; Giambelluca, T. W., The projected timing of climate departure from recent variability. *Nature* **2013,** 502, (7470), 183-187.

12. Zhou, Q.; Birkholzer, J. T.; Tsang, C.-F.; Rutqvist, J., A method for quick assessment of CO_2 storage capacity in closed and semi-closed saline formations. *International Journal of Greenhouse Gas Control* **2008,** 2, (4), 626-639.

13. Morris, J. P.; Detwiler, R. L.; Friedmann, S. J.; Vorobiev, O. Y.; Hao, Y., The large-scale geomechanical and hydrogeological effects of multiple CO_2 injection sites on formation stability. *International Journal of Greenhouse Gas Control* **2011,** 5, (1), 69-74.

14. Bachu, S., CO_2 storage in geological media: Role, means, status and barriers to deployment. *Progress in Energy and Combustion Science* **2008,** 34, (2), 254-273.

15. Rathnaweera, T. D.; Ranjith, P. G.; Perera, M. S. A.; Yang, S. Q., Determination of effective stress parameters for effective CO_2 permeability in deep saline aquifers: An experimental study. *Journal of Natural Gas Science and Engineering* **2015,** 24, 64-79.

16. De Silva, G. P. D.; Ranjith, P. G.; Perera, M. S. A., Geochemical aspects of CO_2 sequestration in deep saline aquifers: A review. *Fuel* **2015,** 155, 128-143.

17. Song, Z.; Song, H.; Cao, Y.; Killough, J.; Leung, J.; Huang, G.; Gao, S., Numerical research on CO_2 storage efficiency in saline aquifer with low-velocity non-Darcy flow. *Journal of Natural Gas Science and Engineering* **2015,** 23, 338-345.

18. Castelletto, N.; Teatini, P.; Gambolati, G.; Bossie-Codreanu, D.; Vincké, O.; Daniel, J.-M.; Battistelli, A.; Marcolini, M.; Donda, F.; Volpi, V., Multiphysics modeling of CO_2 sequestration in a faulted saline formation in Italy. *Advances in Water Resources* **2013,** 62, Part C, 570-587.

19. Okwen, R. T.; Stewart, M. T.; Cunningham, J. A., Analytical solution for estimating storage efficiency of geologic sequestration of CO_2. *International Journal of Greenhouse Gas Control* **2010,** 4, (1), 102-107.

20. Kharaka, Y. K.; Cole, D. R.; Thordsen, J. J.; Kakouros, E.; Nance, H. S., Gas–water–rock interactions in sedimentary basins: CO_2 sequestration in the Frio Formation, Texas, USA. *Journal of Geochemical Exploration* **2006,** 89, (1–3), 183-186.

21. Kongsjorden, H.; Kårstad, O.; Torp, T. A., Saline aquifer storage of carbon dioxide in the Sleipner project. *Waste Management* **1998,** 17, (5–6), 303-308.

22. Navarre-Sitchler, A.; Thyne, G., Effects of carbon dioxide on mineral weathering rates at earth surface conditions. *Chemical Geology* **2007,** 243, (1–2), 53-63.

23. Wilson, E. J.; Johnson, T. L.; Keith, D. W., Regulating the Ultimate Sink: Managing the Risks of Geologic CO_2 Storage. *Environmental Science & Technology* **2003,** 37, (16), 3476-3483.

24. Bachu, S.; Gunter, W. D.; Perkins, E. H., Aquifer disposal of CO_2: Hydrodynamic and mineral trapping. *Energy Conversion and Management* **1994,** 35, (4), 269-279.

25. Aycaguer, A. C.; Lev-On, M.; Winer, A. M., Reducing carbon dioxide emissions with enhanced oil recovery projects: A life cycle assessment approach. *Energy and Fuels* **2001,** 15, (2), 303-308.

26. Gaspar Ravagnani, A. T. F. S.; Ligero, E. L.; Suslick, S. B., CO_2 sequestration through enhanced oil recovery in a mature oil field. *Journal of Petroleum Science and Engineering* **2009,** 65, (3–4), 129-138.

27. Walter, L.; Binning, P. J.; Oladyshkin, S.; Flemisch, B.; Class, H., Brine migration resulting from CO_2 injection into saline aquifers – An approach to risk estimation including various levels of uncertainty. *International Journal of Greenhouse Gas Control* **2012,** 9, 495-506.

28. Ruan, B.; Xu, R.; Wei, L.; Ouyang, X.; Luo, F.; Jiang, P., Flow and thermal modeling of CO_2 in injection well during geological sequestration. *International Journal of Greenhouse Gas Control* **2013,** 19, 271-280.

29. Duan, Z.; Sun, R., An improved model calculating CO_2 solubility in pure water and aqueous NaCl solutions from 273 to 533 K and from 0 to 2000 bar. *Chemical Geology* **2003,** 193, (3–4), 257-271.

30. Mandalaparty, P.; Deo, M.; Moore, J., Gas-compositional effects on mineralogical reactions in carbon dioxide sequestration. *Soc Pet Engineers J* **2011,** 16, (4), 949-958.

31. Baranes, E.; Mirabel, F.; Poudou, J.-C., Access to natural gas storage facilities: Strategic and regulation issues. *Energy Economics* **2014,** 41, 19-32.

32. Deshpande, K. B.; Zimmerman, W. B.; Tennant, M. T.; Webster, M. B.; Lukaszewski, M. W., Optimization methods for the real-time inverse problem posed by modelling of liquefied natural gas storage. *Chemical Engineering Journal* **2011,** 170, (1), 44-52.

33. Chiou-Wei, S.-Z.; Linn, S. C.; Zhu, Z., The response of U.S. natural gas futures and spot prices to storage change surprises: Fundamental information and the effect of escalating physical gas production. *Journal of International Money and Finance* **2014,** 42, 156-173.

34. Imbus, S. W.; Orr, F. M.; Kuuskraa, V. A.; Kheshgi, H.; Bennaceur, K.; Gupta, N.; Rigg, A.; Hovorka, S.; Myer, L. R.; Benson, S. M., Critical Issues in CO_2 Capture and Storage: Findings of the SPE Advanced Technology Workshop (ATW) on Carbon Sequestration. In Society of Petroleum Engineers. **2006,** SPE 102968.

35. Mander, S.; Polson, D.; Roberts, T.; Curtis, A., Risk from CO_2 storage in saline aquifers: A comparison of lay and expert perceptions of risk. *Energy Procedia* **2011,** 4, 6360-6367.

36. van Leeuwen, C.; Hensen, A.; Meijer, H. A. J., Leak detection of CO_2 pipelines with simple atmospheric CO_2 sensors for carbon capture and storage. *International Journal of Greenhouse Gas Control* **2013,** 19, 420-431.

37. Connell, L.; Down, D.; Lu, M.; Hay, D.; Heryanto, D., An investigation into the integrity of wellbore cement in CO_2 storage wells: Core flooding experiments and simulations. *International Journal of Greenhouse Gas Control* **2015,** 37, 424-440.

38. Farquhar, S. M.; Pearce, J. K.; Dawson, G. K. W.; Golab, A.; Sommacal, S.; Kirste, D.; Biddle, D.; Golding, S. D., A fresh approach to investigating CO_2 storage: Experimental CO_2–water–rock interactions in a low-salinity reservoir system. *Chemical Geology* **2015,** 399, 98-122.

39. Gaus, I., Role and impact of CO_2–rock interactions during CO_2 storage in sedimentary rocks. *International Journal of Greenhouse Gas Control* **2010,** 4, (1), 73-89.

40. Apps, J. A.; Zheng, L.; Zhang, Y.; Xu, T.; Birkholzer, J. T., Evaluation of potential changes in groundwater quality in response to CO_2 leakage from deep geologic storage. *Transport in Porous Media* **2010,** 82, (1), 215-246.

41. Gunter, W. D.; Perkins, E. H.; McCann, T. J., Aquifer disposal of CO_2-rich gases: Reaction design for added capacity. *Energy Conversion and Management* **1993,** 34, (9–11), 941-948.

42. Kaszuba, J. P.; Janecky, D. R.; Snow, M. G., Experimental evaluation of mixed fluid reactions between supercritical carbon dioxide and NaCl brine: Relevance to the integrity of a geologic carbon repository. *Chemical Geology* **2005,** 217, (3–4), 277-293.

43. Gibson-Poole, C. M.; Root, R. S.; Lang, S. C.; Streit, J. E.; Hennig, A. L.; Otto, C. J.; Underschultz, J., Conducting comprehensive analyses of potential sites for geological CO_2 storage. In *Greenhouse Gas Control Technologies 7*, Wilson, E. S. R. W. K. F. G.; Thambimuthu, T. M. G., Eds. Elsevier Science Ltd: Oxford, **2005**; pp 673-681.

44. Rosenbauer, R. J.; Koksalan, T.; Palandri, J. L., Experimental investigation of CO_2–brine–rock interactions at elevated temperature and pressure: Implications for CO_2 sequestration in deep-saline aquifers. *Fuel Processing Technology* **2005,** 86, (14–15), 1581-1597.

45. Shukla, R.; Ranjith, P.; Haque, A.; Choi, X., A review of studies on CO_2 sequestration and caprock integrity. *Fuel* **2010,** 89, (10), 2651-2664.

46. Alemu, B. L.; Aker, E.; Soldal, M.; Johnsen, Ø.; Aagaard, P., Influence of CO_2 on rock physics properties in typical reservoir rock: a CO_2 flooding experiment of brine saturated sandstone in a CT-scanner. *Energy Procedia* **2011,** 4, 4379-4386.

47. Kvamme, B.; Liu, S., Reactive transport of CO_2 in saline aquifers with implicit geomechanical analysis. *Energy Procedia* **2009,** 1, (1), 3267-3274.

48. Kweon, H.; Payne, C.; Deo, M., Reactive and Pore Structure Changes in Carbon Dioxide Sequestration. *Industrial & Engineering Chemistry Research* **2015,** 54, (16), 4552-4560.

49. McGarr, A., Seismic moments and volume changes. *Journal of Geophysical Research* **1976,** 81, (8), 1487-1494.

50. Shapiro, S.; Dinske, C.; Kummerow, J., Probability of a given-magnitude earthquake induced by a fluid injection. *Geophysical research letters* **2007,** 34, (22).

51. Kutchko, B. G.; Strazisar, B. R.; Dzombak, D. A.; Lowry, G. V.; Thauiow, N., Degradation of well cement by CO_2 under geologic sequestration conditions. *Environmental Science and Technology* **2007,** 41, (13), 4787-4792.

52. Kutchko, B. G.; Strazisar, B. R.; Lowry, G. V.; Dzombak, D. A.; Thaulow, N., Rate of CO_2 attack on hydrated class H well cement under geologic sequestration conditions. *Environmental Science and Technology* **2008,** 42, (16), 6237-6242.

53. Mason, H. E.; Du Frane, W. L.; Walsh, S. D. C.; Dai, Z.; Charnvanichborikarn, S.; Carroll, S. A., Chemical and mechanical properties of wellbore cement altered by CO_2-rich brine using a multianalytical approach. *Environmental Science and Technology* **2013,** 47, (3), 1745-1752.

54. Strazisar, B.; Kutchko, B.; Huerta, N., Chemical Reactions of Wellbore Cement Under CO_2 Storage Conditions: Effects of Cement Additives. *Energy Procedia* **2009,** 1, (1), 3603-3607.

55. Benge, G., Improving wellbore seal integrity in CO_2 injection wells. *Energy Procedia* **2009,** 1, (1), 3523-3529.

56. Watson, T. L.; Bachu, S., Evaluation of the Potential for Gas and CO_2 Leakage Along Wellbores. *Society of Petroleum Engineers Drilling & Completion*, **2009,** 24, (1), 115-126.

57. Carey, J. W.; Wigand, M.; Chipera, S. J.; WoldeGabriel, G.; Pawar, R.; Lichtner, P. C.; Wehner, S. C.; Raines, M. A.; Guthrie Jr, G. D., Analysis and performance of oil well cement with 30 years of CO_2 exposure from the SACROC Unit, West Texas, USA. *International Journal of Greenhouse Gas Control* **2007,** 1, (1), 75-85.

58. Crow, W.; Carey, J. W.; Gasda, S.; Brian Williams, D.; Celia, M., Wellbore integrity analysis of a natural CO_2 producer. *International Journal of Greenhouse Gas Control* **2010,** 4, (2), 186-197.

59. Bacci, G.; Korre, A.; Durucan, S., An experimental and numerical investigation into the impact of dissolution/precipitation mechanisms on CO_2 injectivity in the wellbore and far field regions. *International Journal of Greenhouse Gas Control* **2011,** 5, (3), 579-588.

60. McMillan, B.; Kumar, N.; Bryant, S. L., Time-Dependent Injectivity During CO_2 Storage in Aquifers. In Society of Petroleum Engineers. **2008,** SPE 113937.

61. Oh, J.; Kim, K.-Y.; Han, W. S.; Kim, T.; Kim, J.-C.; Park, E., Experimental and numerical study on supercritical CO_2/brine transport in a fractured rock: Implications of mass transfer, capillary pressure and storage capacity. *Advances in Water Resources* **2013,** 62, Part C, 442-453.

62. Peysson, Y.; André, L.; Azaroual, M., Well injectivity during CO_2 storage operations in deep saline aquifers—Part 1: Experimental investigation of drying effects, salt precipitation and capillary forces. *International Journal of Greenhouse Gas Control* **2014,** 22, 291-300.

63. Kim, K. Y.; Han, W. S.; Oh, J.; Kim, T.; Kim, J. C., Characteristics of Salt-Precipitation and the Associated Pressure Build-Up during CO_2 Storage in Saline Aquifers. *Transport in Porous Media* **2012,** 92, (2), 397-418.

64. Alkan, H.; Cinar, Y.; Ülker, E. B., Impact of Capillary Pressure, Salinity and In situ Conditions on CO_2 Injection into Saline Aquifers. *Transport in Porous Media* **2010,** 84, (3), 799-819.

65. André, L.; Audigane, P.; Azaroual, M.; Menjoz, A., Numerical modeling of fluid–rock chemical interactions at the supercritical CO_2–liquid interface during CO_2 injection into a carbonate reservoir, the Dogger aquifer (Paris Basin, France). *Energy Conversion and Management* **2007,** 48, (6), 1782-1797.

66. Giorgis, T.; Carpita, M.; Battistelli, A., 2D modeling of salt precipitation during the injection of dry CO_2 in a depleted gas reservoir. *Energy Conversion and Management* **2007,** 48, (6), 1816-1826.

67. Mitrović, M.; Malone, A., Carbon capture and storage (CCS) demonstration projects in Canada. *Energy Procedia* **2011,** 4, 5685-5691.

68. Tao, Q.; Checkai, D.; Huerta, N.; Bryant, S. L., An improved model to forecast CO_2 leakage rates along a wellbore. *Energy Procedia* **2011,** 4, 5385-5391.

69. Ravi, K.; Bosma, M.; Gastebled, O., Safe and Economic Gas Wells through Cement Design for Life of the Well. In Society of Petroleum Engineers. **2002,** SPE75700.

70. Lee, J.; Kang, J. M.; Choe, J., Experimental analysis on the effects of variable apertures on tracer transport. *Water Resources Research* **2003,** 39, (1), SBH 7-1.

71. Watanabe, N.; Hirano, N.; Tsuchiya, N., Determination of aperture structure and fluid flow in a rock fracture by high-resolution numerical modeling on the basis of a flow-through experiment under confining pressure. *Water Resources Research* **2008,** 44, (6), W06412.

72. Boutt, D. F.; Grasselli, G.; Fredrich, J. T.; Cook, B. K.; Williams, J. R., Trapping zones: The effect of fracture roughness on the directional anisotropy of fluid flow and colloid transport in a single fracture. *Geophysical research letters* **2006,** 33, (21), L21402.

73. Singurindy, O.; Berkowitz, B., The role of fractures on coupled dissolution and precipitation patterns in carbonate rocks. *Advances in Water Resources* **2005,** 28, (5), 507-521.

74. Dijk, P.; Berkowitz, B., Precipitation and dissolution of reactive solutes in fractures. *Water Resources Research* **1998,** 34, (3), 457-470.

75. de Best-Waldhober, M.; Brunsting, S.; Paukovic, M., Public concepts of CCS: Understanding of the Dutch general public and its reflection in the media. *International Journal of Greenhouse Gas Control* **2012,** 11, Supplement, S139-S147.

76. Fu, Q.; Lu, P.; Konishi, H.; Dilmore, R.; Xu, H.; Seyfried Jr, W. E.; Zhu, C., Coupled alkali-feldspar dissolution and secondary mineral precipitation in batch systems: 1. New experiments at 200 °C and 300 bars. *Chemical Geology* **2009,** 258, (3–4), 125-135.

77. Carroll, S. A.; McNab, W. W.; Dai, Z.; Torres, S. C., Reactivity of Mount Simon Sandstone and the Eau Claire Shale Under CO_2 Storage Conditions. *Environmental Science & Technology* **2013,** 47, (1), 252-261.

78. Soong, Y.; Hedges, S. W.; Howard, B. H.; Dilmore, R. M.; Allen, D. E., Effect of contaminants from flue gas on CO_2 sequestration in saline formation. *International Journal of Energy Research* **2014,** 38, (9), 1224-1232.

79. Emberley, S.; Hutcheon, I.; Shevalier, M.; Durocher, K.; Gunter, W. D.; Perkins, E. H., Geochemical monitoring of fluid-rock interaction and CO_2 storage at the Weyburn CO_2-injection enhanced oil recovery site, Saskatchewan, Canada. *Energy* **2004,** 29, (9–10), 1393-1401.

80. Lebedev, M.; Mikhaltsevich, V.; Bilenko, O.; Dance, T.; Pervukhina, M.; Gurevich, B., Experimental Laboratory Study on the Acoustic Response of Sandstones During Injection of Supercritical CO_2 on CRC2 Sample from Otway Basin Australia. *Energy Procedia* **2013,** 37, 4106-4113.

81. Chang, C.; Zhou, Q.; Xia, L.; Li, X.; Yu, Q., Dynamic displacement and non-equilibrium dissolution of supercritical CO_2 in low-permeability sandstone: An experimental study. *International Journal of Greenhouse Gas Control* **2013,** 14, 1-14.

82. Berg, S.; Oedai, S.; Ott, H., Displacement and mass transfer between saturated and unsaturated CO_2–brine systems in sandstone. *International Journal of Greenhouse Gas Control* **2013,** 12, 478-492.

83. Fischer, S.; Zemke, K.; Liebscher, A.; Wandrey, M., Petrophysical and petrochemical effects of long-term CO_2 -exposure experiments on brine-saturated reservoir sandstone. *Energy Procedia* **2011,** 4, 4487-4494.

84. Kogure, T.; Nishizawa, O.; Chiyonobu, S.; Yazaki, Y.; Shibatani, S.; Xue, Z., Effect of Sub-core Scale Heterogeneity on Relative Permeability Curves of Porous Sandstone in a Water-supercritical CO_2 System. *Energy Procedia* **2013,** 37, 4491-4498.

85. Ruprecht, C.; Pini, R.; Falta, R.; Benson, S.; Murdoch, L., Hysteretic trapping and relative permeability of CO_2 in sandstone at reservoir conditions. *International Journal of Greenhouse Gas Control* **2014,** 27, 15-27.

86. Bertier, P.; Swennen, R.; Laenen, B.; Lagrou, D.; Dreesen, R., Experimental identification of CO_2–water–rock interactions caused by sequestration of CO_2 in Westphalian and Buntsandstein sandstones of the Campine Basin (NE-Belgium). *Journal of Geochemical Exploration* **2006,** 89, (1–3), 10-14.

87. Luquot, L.; Andreani, M.; Gouze, P.; Camps, P., CO_2 percolation experiment through chlorite/zeolite-rich sandstone (Pretty Hill Formation – Otway Basin–Australia). *Chemical Geology* **2012,** 294–295, 75-88.

88. Ketzer, J. M.; Iglesias, R.; Einloft, S.; Dullius, J.; Ligabue, R.; de Lima, V., Water–rock–CO_2 interactions in saline aquifers aimed for carbon dioxide storage: Experimental and numerical modeling studies of the Rio Bonito Formation (Permian), southern Brazil. *Applied Geochemistry* **2009,** 24, (5), 760-767.

89. Wigand, M.; Carey, J. W.; Schütt, H.; Spangenberg, E.; Erzinger, J., Geochemical effects of CO_2 sequestration in sandstones under simulated in situ conditions of deep saline aquifers. *Applied Geochemistry* **2008,** 23, (9), 2735-2745.

90. Wilke, F. D. H.; Vásquez, M.; Wiersberg, T.; Naumann, R.; Erzinger, J., On the interaction of pure and impure supercritical CO_2 with rock forming minerals in saline aquifers: An experimental geochemical approach. *Applied Geochemistry* **2012,** 27, (8), 1615-1622.

91. Yu, Z.; Liu, L.; Yang, S.; Li, S.; Yang, Y., An experimental study of CO_2–brine–rock interaction at in situ pressure–temperature reservoir conditions. *Chemical Geology* **2012,** 326–327, 88-101.

92. Smyth, R. C.; Hovorka, S. D.; Lu, J.; Romanak, K. D.; Partin, J. W.; Wong, C.; Yang, C., Assessing risk to fresh water resources from long term CO_2 injection–laboratory and field studies. *Energy Procedia* **2009,** 1, (1), 1957-1964.

93. Nicot, J.-P., Evaluation of large-scale CO_2 storage on fresh-water sections of aquifers: An example from the Texas Gulf Coast Basin. *International Journal of Greenhouse Gas Control* **2008,** 2, (4), 582-593.

94. Birkholzer, J. T.; Zhou, Q.; Tsang, C.-F., Large-scale impact of CO_2 storage in deep saline aquifers: A sensitivity study on pressure response in stratified systems. *International Journal of Greenhouse Gas Control* **2009,** 3, (2), 181-194.

95. Kaszuba, J. P.; Janecky, D. R.; Snow, M. G., Carbon dioxide reaction processes in a model brine aquifer at 200 °C and 200 bars: implications for geologic sequestration of carbon. *Applied Geochemistry* **2003,** 18, (7), 1065-1080.

96. Daccord, G., Chemical dissolution of a porous medium by a reactive fluid. *Physical review letters* **1987,** 58, (5), 479.

97. Hoefner, M.; Fogler, H. S., Pore evolution and channel formation during flow and reaction in porous media. *AIChE Journal* **1988,** 34, (1), 45-54.

98. Wang, Y.; Hill, A.; Schechter, R., The optimum injection rate for matrix acidizing of carbonate formations. Society of Petroleum Engineers Annual Technical Conference and Exhibition **1993,** SPE 26578.

99. Bazin, B.; Bieber, M. T.; Roque, C.; Bouteca, M., Improvement in the Characterization of the Acid Wormholing by "In Situ" X-Ray CT Visualizations. In Society of Petroleum Engineers. **1996,** SPE 31073.

100. Fredd, C. N.; Tjia, R.; Fogler, H. S., The Existence of an Optimum Damkohler Number for Matrix Stimulation of Carbonate Formations. In Society of Petroleum Engineers. **1997,** SPE 38167.

101. Buijse, M. A.; Glasbergen, G., A Semi-Empirical Model To Calculate Wormhole Growth in Carbonate Acidizing. In Society of Petroleum Engineers. **2005,** SPE 96892.

102. Alemu, B. L.; Aker, E.; Soldal, M.; Johnsen, Ø.; Aagaard, P., Influence of CO_2 on rock physics properties in typical reservoir rock: A CO_2 flooding experiment of brine saturated sandstone in a CT-scanner. *Energy Procedia* **2011,** 4, 4379-4386.

103. Shi, J.-Q.; Xue, Z.; Durucan, S., History matching of CO_2 core flooding CT scan saturation profiles with porosity dependent capillary pressure. *Energy Procedia* **2009,** 1, (1), 3205-3211.

104. Vogt, S. J.; Shaw, C. A.; Maneval, J. E.; Brox, T. I.; Skidmore, M. L.; Codd, S. L.; Seymour, J. D., Magnetic resonance measurements of flow-path enhancement during supercritical CO_2 injection in sandstone and carbonate rock cores. *Journal of Petroleum Science and Engineering* **2014,** 122, 507-514.

105. Balashov, V. N.; Guthrie, G. D.; Hakala, J. A.; Lopano, C. L.; Rimstidt, J. D.; Brantley, S. L., Predictive modeling of CO_2 sequestration in deep saline sandstone reservoirs: Impacts of geochemical kinetics. *Applied Geochemistry* **2013,** 30, 41-56.

106. Cao, P.; Karpyn, Z. T.; Li, L., Dynamic alterations in wellbore cement integrity due to geochemical reactions in CO_2-rich environments. *Water Resources Research* **2013,** 49, (7), 4465-4475.

107. Newell, D. L.; Carey, J. W., Experimental Evaluation of Wellbore Integrity Along the Cement-rock Boundary. *Environmental Science & Technology* **2013,** 47, (1), 276-282.

108. Brunet, J.-P. L.; Li, L.; Karpyn, Z. T.; Kutchko, B. G.; Strazisar, B.; Bromhal, G., Dynamic Evolution of Cement Composition and Transport Properties under Conditions Relevant to Geological Carbon Sequestration. *Energy & Fuels* **2013,** 27, (8), 4208-4220.

109. Burton, M.; Kumar, N.; Bryant, S. L., CO_2 injectivity into brine aquifers: Why relative permeability matters as much as absolute permeability. *Energy Procedia* **2009,** 1, (1), 3091-3098.

110. Izgec, O.; Demiral, B.; Bertin, H. J.; Akin, S., CO_2 Injection in Carbonates. In Society of Petroleum Engineers Western Regional Meeting, Society of Petroleum Engineers. **2005,** SPE 93773.

111. Izgec, O.; Demiral, B.; Bertin, H.; Akin, S., CO_2 injection into saline carbonate aquifer formations I: laboratory investigation. *Transport in Porous Media* **2008,** 72, (1), 1-24.

112. Izgec, O.; Keys, R. S.; Zhu, D.; Hill, A. D., An Integrated Theoretical and Experimental Study on the Effects of Multiscale Heterogeneities in Matrix Acidizing of Carbonates. In *PE ANNUAL TECHNICAL CONFERENCE AND EXHIBITION*, Society of Petroleum Engineers: **2008,** pp 781-794.

113. Wellman, T. P.; Grigg, R. B.; McPherson, B. J.; Svec, R. K.; Lichtner, P. C., Evaluation of CO_2-Brine-Reservoir Rock Interaction with Laboratory Flow Tests and Reactive Transport Modeling. In *International Symposium on Oilfield Chemistry*, Society of Petroleum Engineers: Houston, Texas, **2003,** SPE 80228.

114. Czernichowski-Lauriol, I.; Rochelle, C.; Gaus, I.; Azaroual, M.; Pearce, J.; Durst, P., GEOCHEMICAL INTERACTIONS BETWEEN CO_2, PORE-WATERS AND RESERVOIR ROCKS. In *Advances in the Geological Storage of Carbon Dioxide*, Lombardi, S.; Altunina, L. K.; Beaubien, S. E., Eds. Springer Netherlands: **2006,** Vol. 65, pp 157-174.

115. Rochelle, C. A.; Czernichowski-Lauriol, I.; Milodowski, A. E., The impact of chemical reactions on CO_2 storage in geological formations: a brief review. *Geological Society, London, Special Publications* **2004,** 233, (1), 87-106.

116. Lasaga, A. C.; Luttge, A., Variation of Crystal Dissolution Rate Based on a Dissolution Stepwave Model. *Science* **2001,** 291, (5512), 2400-2404.

117. Beig, M. S.; Lüttge, A., Albite dissolution kinetics as a function of distance from equilibrium: Implications for natural feldspar weathering. *Geochimica et Cosmochimica Acta* **2006,** 70, (6), 1402-1420.

118. Zhu, C.; Veblen, D. R.; Blum, A. E.; Chipera, S. J., Naturally weathered feldspar surfaces in the Navajo Sandstone aquifer, Black Mesa, Arizona: Electron microscopic characterization. *Geochimica et Cosmochimica Acta* **2006,** 70, (18), 4600-4616.

119. Lüttge, A., Crystal dissolution kinetics and Gibbs free energy. *Journal of Electron Spectroscopy and Related Phenomena* **2006,** 150, (2–3), 248-259.

120. Hellmann, R.; Daval, D.; Tisserand, D., The dependence of albite feldspar dissolution kinetics on fluid saturation state at acid and basic pH: Progress towards a universal relation. *Comptes Rendus Geoscience* **2010,** 342, (7–8), 676-684.

121. Arvidson, R. S.; Luttge, A., Mineral dissolution kinetics as a function of distance from equilibrium – New experimental results. *Chemical Geology* **2010,** 269, (1–2), 79-88.

122. Knauss, K. G.; Johnson, J. W.; Steefel, C. I., Evaluation of the impact of CO_2, co-contaminant gas, aqueous fluid and reservoir rock interactions on the geologic sequestration of CO_2. *Chemical Geology* **2005,** 217, (3–4), 339-350.

123. Xu, T.; Apps, J. A.; Pruess, K.; Yamamoto, H., Numerical modeling of injection and mineral trapping of CO_2 with H_2S and SO_2 in a sandstone formation. *Chemical Geology* **2007,** 242, (3–4), 319-346.

124. Liu, F.; Guo, H.; Smallwood, G. J., The chemical effect of CO_2 replacement of N_2 in air on the burning velocity of CH_4 and H_2 premixed flames. *Combustion and Flame* **2003,** 133, (4), 495-497.

125. Ueda, A.; Yajima, T.; Kaieda, H.; Ohsumi, T., CO_2 sequestration into geothermal fields. In *Greenhouse Gas Control Technologies 7*, Wilson, E. S. R. W. K. F. G.; Thambimuthu, T. M. G., Eds. Elsevier Science Ltd: Oxford, **2005,** pp 2007-2010.

126. Ueda, A.; Nakatsuka, Y.; Kunieda, M.; Kuroda, Y.; Yajima, T.; Satoh, H.; Sugiyama, K.; Ozawa, A.; Ohsumi, T.; Wakahama, H.; Mito, S.; Kaji, Y.; Kaieda, H., Laboratory and field tests of CO_2–water injection into the Ogachi hot dry rock site, Japan. *Energy Procedia* **2009,** 1, (1), 3669-3674.

127. Wakahama, H.; Mitoa, S.; Ohsumi, T.; Ueda, A.; Yajima, T.; Satoh, H.; Sugiyama, K.; Ozawa, A.; Ajima, S.; Todaka, N.; Sato, T.; Kato, M.; Kaji, Y.; Tokumarui, T.; Kaieda, H.; Kubota, K., A concept of CO_2 Georeactor sequestration at the Ogachi HDR site, NE Japan. *Energy Procedia* **2009,** 1, (1), 3683-3689.

128. Aste, N.; Del Pero, C., Impact of domestic and tertiary buildings heating by natural gas in the Italian context. *Energy Policy* **2012,** 47, 164-171.

129. Ukwattage, N. L.; Ranjith, P. G.; Yellishetty, M.; Bui, H. H.; Xu, T., A laboratory-scale study of the aqueous mineral carbonation of coal fly ash for CO_2 sequestration. *Journal of Cleaner Production*, **2015,** 103, 665-674

130. Chiara Giolito, G. R., and Giovanni Gianelli, Fluid Evolution in the Deep Reservoir of the Mt. Amiata Geothermal Field, Italy. *Geothermal Resources Council Transactions* **2007,** 31, 153–158.

131. Na, J.; Xu, T.; Yuan, Y.; Feng, B.; Tian, H.; Bao, X., An integrated study of fluid–rock interaction in a CO_2-based enhanced geothermal system: A case study of Songliao Basin, China. *Applied Geochemistry* **2015,** 59, 166-177.

132. Qi, R.; LaForce, T. C.; Blunt, M. J., Design of carbon dioxide storage in aquifers. *International Journal of Greenhouse Gas Control* **2009,** 3, (2), 195-205.

133. Munz, I. A.; Brandvoll, Ø.; Haug, T. A.; Iden, K.; Smeets, R.; Kihle, J.; Johansen, H., Mechanisms and rates of plagioclase carbonation reactions. *Geochimica et Cosmochimica Acta* **2012,** 77, 27-51.

134. Lo Ré, C.; Kaszuba, J. P.; Moore, J. N.; McPherson, B. J., Fluid–rock interactions in CO_2-saturated, granite-hosted geothermal systems: Implications for natural and engineered systems from geochemical experiments and models. *Geochimica et Cosmochimica Acta* **2014,** 141, 160-178.

135. Salvage, K. M.; Yeh, G.-T., Development and application of a numerical model of kinetic and equilibrium microbiological and geochemical reactions (BIOKEMOD). *Journal of Hydrology* **1998,** 209, (1–4), 27-52.

136. Wang, Y., Nanogeochemistry: Nanostructures, emergent properties and their control on geochemical reactions and mass transfers. *Chemical Geology* **2014,** 378–379, 1-23.

137. Atchley, A. L.; Navarre-Sitchler, A. K.; Maxwell, R. M., The effects of physical and geochemical heterogeneities on hydro-geochemical transport and effective reaction rates. *Journal of Contaminant Hydrology* **2014,** 165, 53-64.

138. Carpenter, M.; Kvien, K.; Aarnes, J., The CO_2 QUALSTORE guideline for selection, characterisation and qualification of sites and projects for geological storage of CO_2. *International Journal of Greenhouse Gas Control* **2011,** 5, (4), 942-951.

139. Carling, G. T.; Fernandez, D. P.; Johnson, W. P., Dust-mediated loading of trace and major elements to Wasatch Mountain snowpack. *Science of The Total Environment* **2012,** 432, 65-77.

140. Lin, C. L. G., C. , Microscale Characterization and Analysis of Particulate Systems via Cone-Beam X-ray Microtomography (XIMT). *Innovations in Natural Resource Processing* **2005**, 421-432.

141. Miller, J. D.; Lin, C. L.; Garcia, C.; Arias, H., Ultimate recovery in heap leaching operations as established from mineral exposure analysis by X-ray microtomography. *International Journal of Mineral Processing* **2003,** 72, (1–4), 331-340.

142. D. Garcia, C. L. L., and J.D. Miller, Experimental Evaluation of a Mineral Exposure Model for Crushed Copper Ores. *Society for mining, metallurgy, and Exploration, Inc. (SME)* **2006**, 261-268.

143. Tiwari, P.; Deo, M.; Lin, C. L.; Miller, J. D., Characterization of oil shale pore structure before and after pyrolysis by using X-ray micro CT. *Fuel* **2013,** 107, 547-554.

144. Witherspoon, P. A.; Wang, J. S. Y.; Iwai, K.; Gale, J. E., Validity of Cubic Law for fluid flow in a deformable rock fracture. *Water Resources Research* **1980,** 16, (6), 1016-1024.

145. Carroll, S.; McNab, W.; Torres, S., Experimental Study of Cement - Sandstone/Shale - Brine - CO_2 Interactions. *Geochemical Transactions* **2011,** 12, (1), 1-19.

146. Emberley, S.; Hutcheon, I.; Shevalier, M.; Durocher, K.; Mayer, B.; Gunter, W. D.; Perkins, E. H., Monitoring of fluid–rock interaction and CO_2 storage through produced fluid sampling at the Weyburn CO_2-injection enhanced oil recovery site, Saskatchewan, Canada. *Applied Geochemistry* **2005,** 20, (6), 1131-1157.

147. Garcia, D. J.; Shao, H.; Hu, Y.; Ray, J. R.; Jun, Y.-S., Supercritical CO_2-brine induced dissolution, swelling, and secondary mineral formation on phlogopite surfaces at 75-95 °C and 75 atm. *Energy & Environmental Science* **2012,** 5, (2), 5758-5767.

148. Kharaka, Y. K.; Thordsen, J. J.; Hovorka, S. D.; Seay Nance, H.; Cole, D. R.; Phelps, T. J.; Knauss, K. G., Potential environmental issues of CO_2 storage in deep saline aquifers: Geochemical results from the Frio-I Brine Pilot test, Texas, USA. *Applied Geochemistry* **2009,** 24, (6), 1106-1112.

149. Lu, P.; Fu, Q.; Seyfried, W., Jr.; Hereford, A.; Zhu, C., Navajo Sandstone–brine–CO_2 interaction: implications for geological carbon sequestration. *Environmental Earth Sciences* **2011,** 62, (1), 101-118.

150. Lu, J.; Kharaka, Y. K.; Thordsen, J. J.; Horita, J.; Karamalidis, A.; Griffith, C.; Hakala, J. A.; Ambats, G.; Cole, D. R.; Phelps, T. J.; Manning, M. A.; Cook, P. J.; Hovorka, S. D., CO_2–rock–brine interactions in Lower Tuscaloosa Formation at Cranfield CO_2 sequestration site, Mississippi, U.S.A. *Chemical Geology* **2012,** 291, 269-277.

151. Gaus, I.; Azaroual, M.; Czernichowski-Lauriol, I., Reactive transport modelling of the impact of CO_2 injection on the clayey cap rock at Sleipner (North Sea). *Chemical Geology* **2005,** 217, (3–4), 319-337.

152. Li, D.; Duan, Z., The speciation equilibrium coupling with phase equilibrium in the H_2O–CO_2–NaCl system from 0 to 250 °C, from 0 to 1000 bar, and from 0 to 5 molality of NaCl. *Chemical Geology* **2007,** 244, (3–4), 730-751.

153. Peng, C.; Crawshaw, J. P.; Maitland, G. C.; Martin Trusler, J. P.; Vega-Maza, D., The pH of CO_2-saturated water at temperatures between 308K and 423K at pressures up to 15MPa. *The Journal of Supercritical Fluids* **2013,** 82, 129-137.

154. Xu, T., TOUGHREACT User's Guide: A Simulation Program for Non-isothermal Multiphase Reactive Geochemical Transport in Variably Saturated Geologic Media, V1.2.1. In **2008**.

155. Lasaga, A. C., Chemical kinetics of water-rock interactions. *Journal of Geophysical Research: Solid Earth* **1984,** 89, (B6), 4009-4025.

156. Xu, T.; Apps, J. A.; Pruess, K., Reactive geochemical transport simulation to study mineral trapping for CO_2 disposal in deep arenaceous formations. *Journal of Geophysical Research: Solid Earth* **2003,** 108, (B2), ECV 3-1.

157. Schott, J.; Pokrovsky, O. S.; Oelkers, E. H., The Link Between Mineral Dissolution/Precipitation Kinetics and Solution Chemistry. *Reviews in Mineralogy and Geochemistry* **2009,** 70, (1), 207-258.

158. Zhou, X.; Lin, X.; Huo, M.; Zhang, Y., The hydration of saline oil-well cement. *Cement and Concrete Research* **1996,** 26, (12), 1753-1759.

159. Nasvi, M. C. M.; Ranjith, P. G.; Sanjayan, J.; Haque, A.; Li, X., Mechanical behaviour of wellbore materials saturated in brine water with different salinity levels. *Energy* **2014,** 66, 239-249.

160. Fischer, S.; Liebscher, A., Mineral Solubilities in CO_2-Saturated NaCl Brine Systems. *Procedia Earth and Planetary Science* **2013,** 7, 260-263.

161. Yan, W.; Huang, S.; Stenby, E. H., Measurement and modeling of CO_2 solubility in NaCl brine and CO_2–saturated NaCl brine density. *International Journal of Greenhouse Gas Control* **2011,** 5, (6), 1460-1477.

162. Zhao, J.; Lu, W.; Zhang, F.; Lu, C.; Du, J.; Zhu, R.; Sun, L., Evaluation of CO_2 solubility-trapping and mineral-trapping in microbial-mediated CO_2–brine–sandstone interaction. *Marine Pollution Bulletin* **2014,** 85, (1), 78-85.

163. Noiriel, C.; Luquot, L.; Madé, B.; Raimbault, L.; Gouze, P.; van der Lee, J., Changes in reactive surface area during limestone dissolution: An experimental and modelling study. *Chemical Geology* **2009,** 265, (1–2), 160-170.